THE OPTICAL PROPERTIES OF $RTiO_3$ PEROVSKITES
(R = LA, CE, PR, ND, SM, GD)

By

DAVID A. CRANDLES, B.Sc., M.Sc.

A Thesis

Submitted to the Faculty of Graduate Studies

in Partial Fulfilment of the Requirements

for the Degree

Doctor of Philosophy

McMaster University

THE OPTICAL PROPERTIES OF $RTiO_3$ PEROVSKITES
R = LA, CE, PR, ND, SM, GD

DOCTOR OF PHILOSOPHY(1992) McMASTER UNIVERSITY

(Physics) Hamilton, Ontario

TITLE: The Optical Properties of $RTiO_3$ Perovskites
R = La, Ce, Pr, Nd, Sm, Gd

AUTHOR: David A. Crandles, B.Sc. (U. Western Ontario)
M.Sc. (University of Ottawa)

SUPERVISOR: Dr. T. Timusk

NUMBER OF PAGES: vii, 132

ABSTRACT

Reflectance spectroscopy (50-40000 cm^{-1}) has been used to study the rare earth titanium (III) oxides ($RTiO_3$, R = La, Ce, Pr, Nd, Sm, Gd). A mid-infrared absorption has been observed in all members of the series. With decreasing rare earth radius (and decreasing Ti-O-Ti bond angle) the band shifts to higher frequencies. A tight-binding calculation of the effect of the Ti-O-Ti bond angle on the conduction band width supports the picture in which the mid-infrared band is due to transitions from the lower Hubbard to the upper Hubbard band. Because this intrinsic absorption is at lower energy than transitions corresponding to O(2p)-Ti(3d) charge transfer ($\approx$ 4 eV) the rare earth titanites are classified as Mott-Hubbard insulators. Systematic variations in the infrared active phonon spectra were observed and related to a tetragonal distortion of the TiO_6 octahedron in $NdTiO_3$, $SmTiO_3$ and $GdTiO_3$. In a second study, the reflectance of four well characterized (x-ray, neutron activation, thermogravimetric, dc resistivity, magnetization) doped $LaTiO_3$ samples was measured. Although the starting materials contained equimolar amounts of La and Ti, the neutron activation results and structural considerations indicate the presence of La vacancies. There is a transfer of oscillator strength from the mid-infrared band to lower frequencies in highly doped samples but transitions placing two electrons on one site (from the lower to the upper Hubbard band) retain considerable oscillator strength even in a sample where approximately one-fifth of the sites are empty.

ACKNOWLEDGEMENTS

I would like to thank my supervisor, Professor Tom Timusk, for his support and guidance these past four years. I have extreme respect for his creativity and for his obsession with making the best measurement.

I have enjoyed being part of the non-copper oxide subculture with Dr. John Greedan. I appreciate his sincere interest in my project as well as many useful discussions.

Thanks are due to Dr. Jules Carbotte both for helpful discussions in commitee meetings and for giving two excellent courses in solid state theory.

I feel privileged to have worked with all the people in the lab over the past few years especially Ning Cao, Andy Duncan, Chris Homes, Rob Hughes, Maureen Reedyk, and Xiucheng Wu. Big things like building the reflectometers and taking courses and little things like "filling up the trap" for me when I went home to my family will never be forgotten.

I owe special thanks to Jim Garrett for friendship and for growing the crystals which made my research possible. Frank Gibbs and Alice Pidruczny collected all the thermogravimetric and neutron activation analysis data respectively. Milan Maric and Wen He Gong performed the x-ray analysis. Thanks are due to Dr. C. Stager for the use of his SQUID.

More than anyone I would like to thank Maureen Keogh who has taken care of our children and enabled me to go out and play at McMaster.

Contents

Chapter 1

Introduction

In the past five years there has been a tremendous amount of research on the superconducting copper oxides. Virtually every experimental and theoretical technique available to solid state physicists has been applied to these systems. Still, neither the mechanism of superconductivity nor the peculiar normal state properties of these compounds are completely understood[1].

Accompanying this widespread activity is a resurgence of interest in transition metal oxides in general. There has been increased attention to old problems such as the electronic structure of NiO [2, 3] and V_2O_3 [4] as well work on new V,Ti,Nb and Ni oxides [5, 6, 7, 8]. The electronic structure of transition metal oxides is a problem which seems to resurface at least once a decade. For many of these oxides the Bloch-Wilson explanation of whether a material is insulating or metallic fails. Bloch was the first to show that an electron moving in a periodic potential cannot have arbitrary energy: there are forbidden and allowed energy bands. It was Wilson who predicted that a material is an insulator if, at absolute zero, all the energy bands are filled and a metal if the highest energy band is partially filled. Bloch-Wilson insulators are diamagnetic as Table 1.1 illustrates.

Table 1.1: Magnetic Susceptibilities of filled band insulators (FB), metals (M) and magnetic insulators (MI). The high temperature susceptibility of the magnetic insulators is positive and follows the Curie-Weiss law. Data taken from references [20,25,52,87,94].

material	electronic structure	χ_m (CGS 10^{-6} cm^{-3} mol^{-1})
Ar	FB	-19.4
Si	FB	-0.26
Ge	FB	-0.58
CdS	FB	-1.77
NaCl	FB	-15.5
Na	M	+ 15.8
K	M	+20.7
Hf	M	+71.4
$SrVO_{2.9}$	M	+ 250
$La_{1.875}Sr_{.25}CuO_4$	M	> 0
La_2CuO_4	MI	> 0
CoO	MI	> 0
NiO	MI	> 0

The Bloch-Wilson classification scheme works nicely for many materials but runs into trouble with magnetic insulators which have positive magnetic susceptibilities. Positive contributions to the magnetic susceptibility can come from either unpaired, localized spins or unfilled metallic bands. The anomalous electronic structure of the transition metal oxides was first observed over fifty years ago. In 1937 de Boer and Verwey pointed out that certain late transition metal oxides should be metals according to the one-electron theory of solids but are actually antiferromagnetic insulators[9]. Band theory, or the one electron theory of solids breaks down whenever the dispersional band width, W, is roughly the same as the coulomb correlation energy, U, the energy required to put two electrons on one site [10]. It is not a coincidence that the bonding states in the magnetic insulators derive to a certain extent from transition metal d states. Being more localized than either s or p states, the overlap integral between neighbouring d states is smaller. As the overlap integral is proportional to the band width, the band width in transition metal oxides is smaller than in the alkali or noble metals. The rare earth titanium (III) oxides are materials where $U \geq W$ and are the subject of this thesis.

1.1 Previous Work on Rare Earth Titanites

$RTiO_3$ (R = La, Ce, Pr, Nd, Sm and Gd etc.) perovskites are an interesting family of magnetic insulators. The electronic structure of these materials is not known, however transport and magnetic measurements by various workers have established that the Ti $3d$ electrons are weakly localized or itinerant in $LaTiO_3$ and the degree of localization of the $3d$ electrons increases with increasing rare earth mass [11, 12, 13]. Figure 1.1 shows the temperature variation of the resistivity of $RTiO_3$ compounds as measured by Bazuev *et al.* . Note that in this figure $LaTiO_3$ exhibits a metallic increase of resistivity with increasing temperature, the resistivity of $CeTiO_3$ and $PrTiO_3$ exhibits little temperature dependence while the resistivity of the heavier rare earths manifests

a semiconductor or insulator-like decrease of resistivity with temperature. Although the systematic increase in resistivity across the rare earth series is observed by all groups, there is some inconsistency in the observed transport properties . As will be discussed in detail, the physical properties of the rare earth titanites are extremely sensitive to oxygen content and rare earth vacancies.

Magnetic measurements provide further evidence for the systematic increase in $3d$ electron localization. Figure 1.2 shows the temperature dependence of the susceptibility for several light rare perovskites. In $LaTiO_3$ the magnetism comes from the Ti(III) sublattice. Above 125 K $LaTiO_3$ manifests temperature independent paramagnetism suggesting an itinerant character for the Ti $3d$ electrons[14]. On the other hand, Maclean *et al.* determined that the contribution of the Ti(III) sublattice to the magnetic susceptibility of $PrTiO_3$ and $NdTiO_3$ was of the Curie-Weiss (localized moment) type. They did this by subtracting the temperature dependent susceptibilities of isostructural $PrScO_3$ and $NdScO_3$ which approximate the rare-earth-only contributions to the susceptibility of $PrTiO_3$ and $NdTiO_3$ [15]. All the rare earth titanites, except $NdTiO_3$, exhibit some form of ordered magnetism.

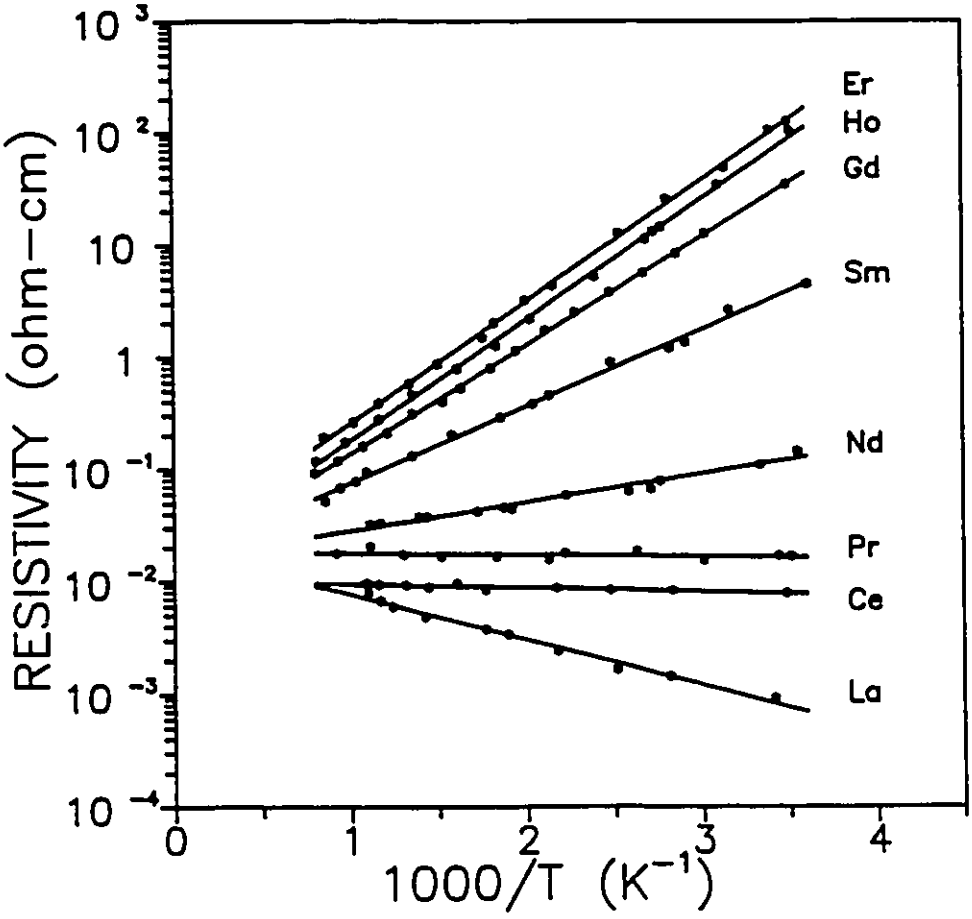

Figure 1.1: Resistivity versus Inverse Temperature of $RTiO_3$ compounds as measured by Bazuev *et al.* . From reference [11].

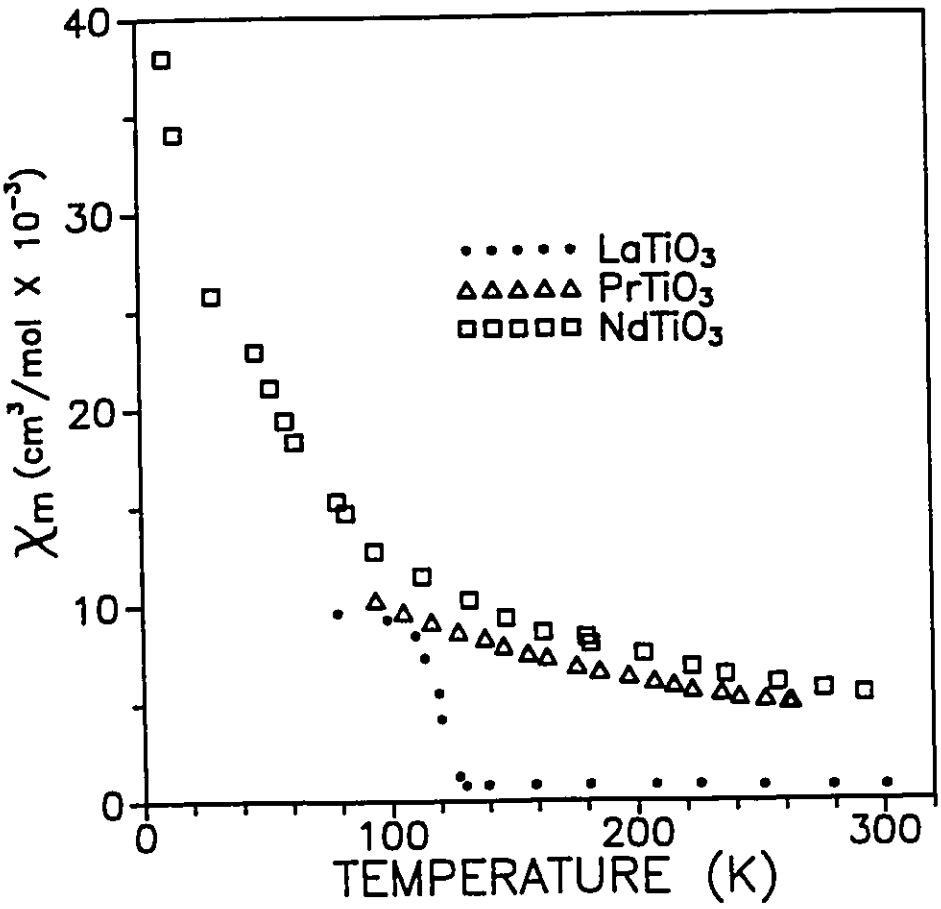

Figure 1.2: Temperature Dependence of the Magnetic Susceptibility for various rare earth perovskites. In $LaTiO_3$, the magnetism is due to the Ti(III) sublattice only while in $PrTiO_3$ and $NdTiO_3$ there is a further contribution from the rare earth sublattice. Comparison with $PrScO_3$ and $NdScO_3$, where the magnetism is due to the rare earth ions only, suggests that the Ti(III) sublattice in $PrTiO_3$ and $NdTiO_3$ obeys the Curie-Weiss law. Data from references [14,15].

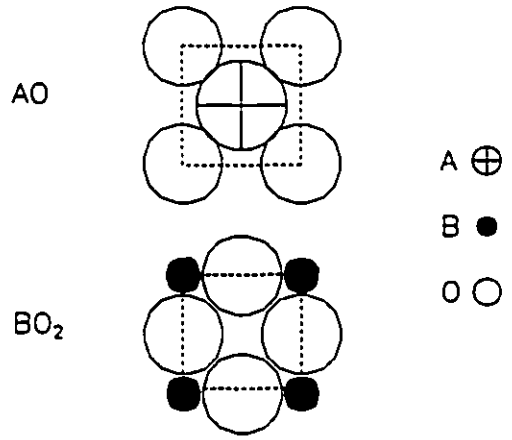

Figure 1.3: Alternating layers of the ABO_3 perovskite structure.

The crystal structure of $RTiO_3$ compounds changes systematically as R decreases in size. In future chapters, correlations will be made between the Ti-O network and the vibrational and electronic properties of the series so it is useful to discuss the crystal structure in some detail. The perovskite structure is composed of alternating AO and BO_2 layers as illustrated in figure 1.3. Note that A is the larger of A and B. Thus the rare earth titanites are composed of alternating RO and TiO_2 layers. It is the match (or mismatch) between the two layers which determines whether a particular ABO_3 compound will exhibit the cubic perovskite structure or not. As can be seen in figure 1.3, the AO and BO_2 layers desire lattice constants $d_{AO} = \sqrt{2}(r_A + r_O)$ and $d_{BO2} = 2(r_B + r_O)$ respectively where r_A, r_B r_O are the ionic radii. Table 1.2 lists d_{AO} and d_{BO2} for various perovskites calculated using the ionic radii compiled by Shannon [16]. As seen in table 1.2, there appears to be a critical ratio d_{AO}/d_{BO2} $\equiv r \approx 0.9$. If $r \leq 0.9$, the $GdFeO_3$ lattice is favoured and the BO_6 co-operatively buckle as shown in figure 1.4 to reduce the strain between the two layers.

Table 1.2: Lattice constants desired by the AO and BO_2 layers of various perovskite compounds. $\theta(B-O-B)$ less than 180° implies the $GdFeO_3$ structure.

compound	d_{AO}	d_{BO2}	r	$\theta(B-O-B)$
$SrVO_3$	3.52	3.92	0.9	180°
$SrTiO_3$	3.52	3.93	0.9	180°
$LaTiO_3$	3.56	4.06	0.88	157°
$GdTiO_3$	3.41	4.06	0.84	145°

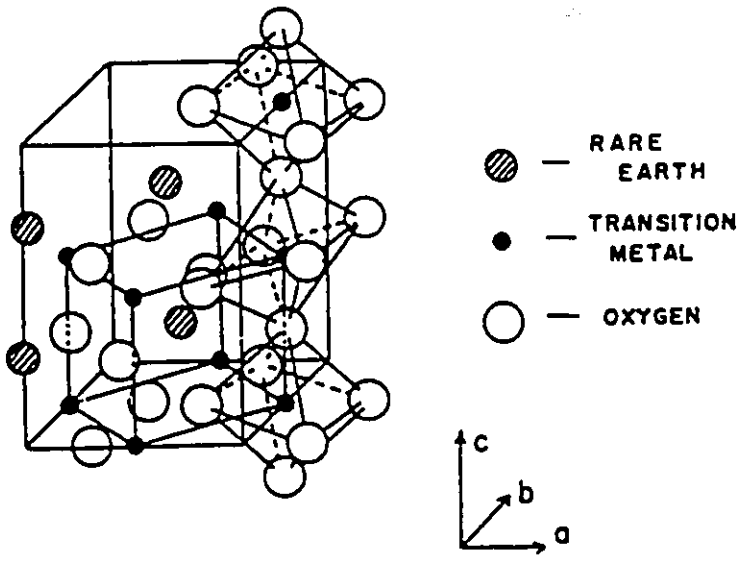

Figure 1.4: The $GdFeO_3$ distorted perovskite structure exhibited by $RTiO_3$ perovskites. From reference [13].

Table 1.3: Physical properties of the light rare earth titanites. Symbols: MI, metal-insulator transition; SC, semiconductor (activation energy in eV); TIP, temperature independent paramagnetism; CW, Curie Weiss, Fi, ferrimagnetic i.e. hyperbolic χ^{-1} vs. T.; F, ferromagnetic; AF, antiferromagnetic with both AF and F components. After reference [13].

			paramagnetism		ordered magnetism	
R	θ(Ti – O – Ti)°	electrical	Ti	R	Ti	R
La	157	MI	TIP	-	AF	-
Ce	?	MI	TIP	non-CW	AF	F,CF
Pr	?	SC (0.03)	CW	CW	AF	CF
Nd	150.5	SC (0.03)	CW	CW	-	-
Sm	147	SC (0.15)	?	?	?	?
Gd	145	SC (0.19)		Fi	F	F

The electrical, magnetic and structural properties of the rare earth titanites are summarized in table 1.3.

1.2 Plan of the Thesis

Reflectance spectroscopy, the technique used by the author to study the rare earth titanites, is a powerful probe of electronic structure and has been used to study many transition metal oxides.

This thesis describes two projects: a determination of the electronic and vibrational properties of the insulating rare earth titanites and a study of the evolution of the electronic structure of $LaTiO_3$ through a doping induced insulator-metal transition. Chapter 2 will discuss the technique of reflectance spectroscopy while

in chapter 3, various theoretical approaches to the electronic structure of magnetic insulators will be be considered. The reflectance of the insulating light rare earth titanites will be presented in chapter 4. In chapter 5 we turn to a study of doped $LaTiO_3$. Stoichiometric $LaTiO_3$ is the least localized of all the rare earth titanites and doping can induce a transition to truly metallic behaviour. A picture of the electronic structure of $RTiO_3$ compounds which is consistent with electrical, magnetic and structural trends in the series will emerge in the discussion of these two sets of experiments.

Chapter 2

Reflectance Spectroscopy

2.1 Optical Response Functions

A plane wave of electromagnetic radiation propagating in a sample is both absorbed and shifted in phase. Thus the response of the crystal to an optical probe is a complex function. One representation of the optical response is the dielectric function ($\hat{\varepsilon}(\omega) = \varepsilon_1(\omega) + i\varepsilon_2(\omega)$) which lends itself to the particularly simple classical sum model. In the sum model each absorption process (excitation of optical phonons, intra- and interband absorption) is considered to be a Lorentz oscillator for which the real and imaginary parts of the dielectric function can be easily calculated [18]. The total dielectric function is then a sum of the functions for each process.

A Lorentz oscillator is described by three parameters: the resonance frequency ω_j, a damping frequency Γ_j which is a measure of how easily it transfers energy to its environment and a plasma frequency ω_{pj} which is a measure of the strength of the coupling of the oscillator to the external electromagnetic field. The sum model for the dielectric function is:

$$\hat{\varepsilon}(\omega) = 1 + \sum_j \frac{\omega_{pj}^2}{(\omega_j^2 - \omega^2) - i\Gamma_j\omega} \tag{2.1}$$

Other representations of the optical response include the complex index of refraction ($\hat{N} = n + ik$) and the complex conductivity ($\hat{\sigma}(\omega) = \sigma_1 + i\sigma_2$). The complex index of refraction and conductivity are related to the dielectric function by the following equations.

$$n = \{\frac{1}{2}[(\epsilon_1^2 + \epsilon_2^2)^{1/2} + \epsilon_1]\}^{1/2} \tag{2.2}$$

$$k = \{\frac{1}{2}[(\epsilon_1^2 + \epsilon_2^2)^{1/2} - \epsilon_1]\}^{1/2} \tag{2.3}$$

$$\sigma_1 = \frac{\omega\epsilon_2}{4\pi} \tag{2.4}$$

$$\sigma_2 = \frac{\omega(\epsilon_1 - 1)}{4\pi} \tag{2.5}$$

2.2 Reflectance and Kramers-Kronig Analysis

The technique used to measure the optical response functions in this thesis is reflectance spectroscopy. Unlike experimental techniques such as ellipsometry and coherent terahertz spectroscopy which allow one to measure the real and imaginary parts of the optical response function simultaneously, reflectance spectroscopy relies on a dispersion relation in order to determine the complete optical response. The reflected electric field (E_r) is related to the incident electric field (E_i) as follows:

$$E_r(\omega) = r(\omega)e^{i\theta(\omega)}E_i(\omega) \tag{2.6}$$

What one measures is the reflected power ($R = |\frac{E_r}{E_i}|^2$) and all the phase information is lost. Happily the real and imaginary parts of the optical constants are not independent as can be seen qualitatively in figure 2.1 which is taken from J. S. Toll [17].

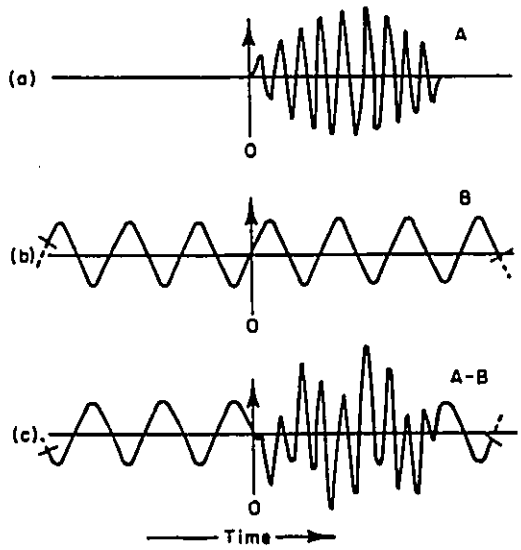

Figure 2.1: Consider an electromagnetic pulse such as that shown in part (a) which reaches a system at $t = 0$. The signal is composed of a superposition of many frequency components with phases appropriately chosen so that the signal is identically zero for $t \leq 0$. It is impossible for the system to absorb the single frequency component shown in (b) without affecting the phase of the other components. If it were possible then a signal would be created for $t \leq 0$ as shown in (c) which implies an effect before the cause. Thus an aborption process is always accompanied by dispersion (a compensating shift of the phases of the other components). From reference [17].

It can be shown [18] that the phase is related to the measured reflectance by the following equation which can be integrated numerically.

$$\theta(\omega_o) = \frac{\omega_o}{\pi} \int_0^\infty \frac{\ln[R(\omega)/R(\omega_o)]}{\omega_o^2 - \omega^2} d\omega \tag{2.7}$$

Once the phase has been calculated one can determine the other optical constants using the folowing equations:

$$n = \frac{1 - r^2}{1 + r^2 - 2r\cos\theta} \tag{2.8}$$

$$k = \frac{2r\sin\theta}{1 + r^2 - 2r\cos\theta} \tag{2.9}$$

$$\epsilon_1 = n^2 - k^2 \tag{2.10}$$

$$\epsilon_2 = 2nk \tag{2.11}$$

2.3 Numerical Integration of Phase Equation

As equation 2.7 indicates, it is necessary to know the reflectance at all frequencies in order to calculate the phase. Thus, it is necessary to extrapolate outside the measured frequency range. In insulators where there is a gap in the excitation spectrum at low frequencies and the reflectance should be constant, one generally observes the reflectance approaching a constant value below the lowest frequency transverse optical phonon and extrapolates this value to zero frequency. For metallic compounds where the reflectance approaches unity as ω approaches zero one usually assumes the Drude model for the dielectric function (a Lorentzian centred at $\omega = 0$ cm^{-1}). One assumes reasonable ω_p and Γ parameters which must satisfy $\frac{\omega_p^2}{60\Gamma} \approx \sigma_{dc}$ where ω_p and Γ are in

cm^{-1} while σ_{dc} is in $\Omega^{-1}cm^{-1}$. One then calculates the Drude n and k using equations 2.2 and 2.3 which are related to the low frequency reflectance extrapolation via

$$R = \frac{(n-1)^2 + k^2}{(n+1)^2 + k^2} \tag{2.12}$$

The high energy regions for which there is no reflectance data are the largest source of error in the phase calculation [18]. At extremely high frequencies, say $\omega \geq 10^6$ cm^{-1} where the electron response is essentially free one uses the extrapolation $R \propto \omega^{-4}$. This can be derived easily. For the Drude model equation 2.1 gives

$$\varepsilon_1 = 1 - \frac{\omega_p^2}{\Gamma^2 + \omega^2} \tag{2.13}$$

$$\varepsilon_2 = \frac{\omega_p^2 \Gamma}{\omega^3} \tag{2.14}$$

At high frequencies ($\omega \gg \Gamma, \omega_p$) these approach

$$\varepsilon_1 \approx 1 - \frac{\omega_p^2}{\omega^2} \tag{2.15}$$

$$\varepsilon_2 \approx 0 \tag{2.16}$$

In the high frequency limit equation 2.3 shows the optical constant $k \approx 0$ while equation 2.2 yields

$$n \approx \varepsilon_1^{1/2} \approx 1 - 1/2\frac{\omega_p^2}{\omega^2} \tag{2.17}$$

Finally, substituting for n and k in equation 2.12 gives:

$$R \approx \frac{(n-1)^2}{(n+1)^2} \approx \frac{\omega_p^4}{16\omega^4} \tag{2.18}$$

Between the highest available reflectance data and the region of validity of the free electron asymptotic form, one assumes $R \propto \omega^{-s}$.

In summary one has the following procedure for analyzing reflectance data: one calculates the phase using the measured reflectance data and extrapolations discussed above. From the reflectance and phase the dielectric function can be determined. One can finally attempt to model the dielectric function using the sum model (equation 2.1) or other models which have not yet been discussed .

2.4 Conductivity Sum Rule

One of the fundamental integral relations obeyed by the optical constants is the conductivity sum rule [18]:

$$\int_0^\infty \sigma(\omega)\mathrm{d}\omega = \frac{\omega_p^2}{8} \tag{2.19}$$

ω_p^2 is related to the total density of electrons in the crystal (N), and the free electron charge (e) and mass (m) via:

$$\omega_p^2 = 4\pi\frac{Ne^2}{m} \tag{2.20}$$

It is sometimes useful to consider the partial sum rule where the integral in equation 2.19 is over a restricted frequency range, m^*, is the effective mass of the electrons in this frequency range and V is the volume per formula unit:

$$N_{eff}(\omega_c) = \frac{2m^*V}{\pi e^2}\int_0^{\omega_c} \sigma(\omega)\mathrm{d}\omega \tag{2.21}$$

The conductivity sum rule can be used to determine whether a particular high frequency extrapolation is physically reasonable. Before the onset of core excitations, N_{eff} should saturate at the number of valence electrons. This can be seen clearly for metallic aluminum in figure 2.2.

Care must be exercised in interpreting the area under a particular band in the optical conductivity spectrum $N_{eff}(\omega_c)$ especially in a multielement compound.

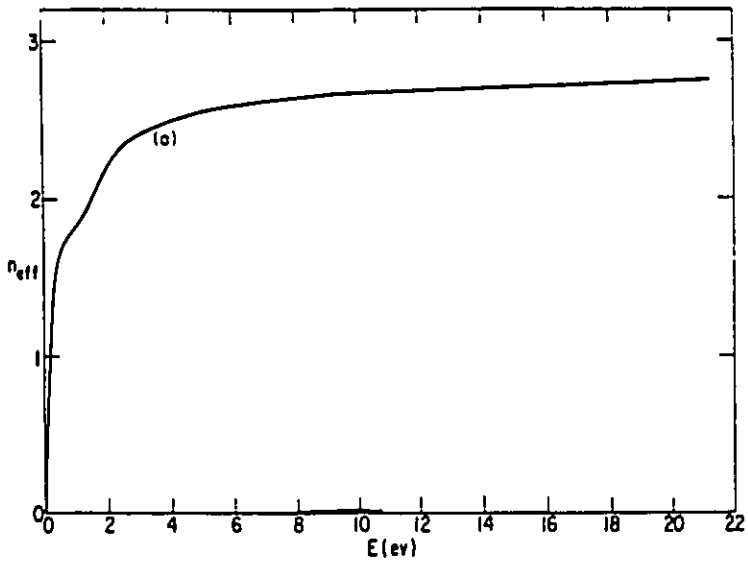

Figure 2.2: Partial sumrule evaluated for metallic aluminum. From reference [19].

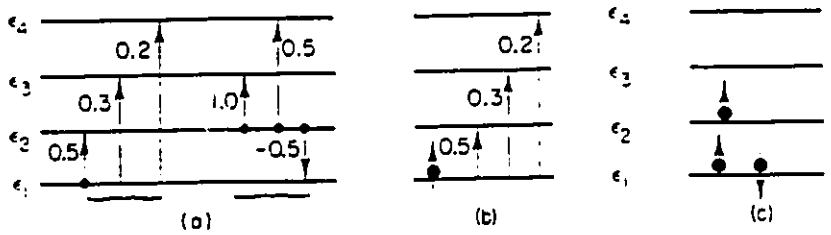

Figure 2.3: (a) An energy level scheme for a system having only four one- electron energy levels. Possible transitions and oscillator strengths are shown. The oscillator strengths are chosen arbitrarily except for the sum-rule requirement. (b) The oscillator strengths for various transitions of the system containing one electron. (c) The oscillator strengths for the system containing three electrons. The sum rule is satisfied for the system, but not for individual electrons. The oscillator strength for the electron in state ϵ_2 is enhanced while the oscillator strength for the spin-up electron in state ϵ_1 is depressed. From reference [18].

The sum rule applies to the whole system of electrons, and oscillator strength can be transferred from one subset of electrons to another. This is explained by Wooten [18] using the atomic system shown in figure 2.19. For an atomic system with Z electrons where f_{mn} is the oscillator strength for a transition from state m to state n the atomic equivalent of equation 2.19 is written:

$$\sum_m f_{mn} = Z \tag{2.22}$$

Consider a four level system with transitions having oscillator strengths cho-

sen arbitrarily except to satisy to the sum rule as illustrated in figure 2.3. If there is one electron in the system, the electron can make transitions to higher levels with the strengths shown in (b) which satisfy the f-sum rule. If there are three electrons in the system, the total oscillator strength for the system is 3. The electron in state ϵ_2 can make transitions with enhanced oscillator strength 1.0 + 0.5 = 1.5. Due to the exclusion principle, the spin-up electron in state ϵ_1 can only make transitions to states ϵ_3 and ϵ_4 and has a depressed total oscillator strength of 0.5. The spin-down electron electron is not affected by the electron in state ϵ_2 and has an oscillator strength of 1.0. The sum rule, which applies to the *system* is satisfied, but the partial sum rule, which applies to particular electrons must be interpreted carefully.

2.5 Reflectance Spectroscopy - some concerns

Reflectance spectroscopy must be done with extreme care in regions where the absorption coefficient is small. Regions of little absorption ($A \ll 1$) occur at low frequencies in metals (where the reflectance $R = (1 - A) \approx 1$) and in regions where R is roughly constant such as below the fundamental band gap in insulators where there can be considerable transmission. With metallic compounds the problem is experimental: it takes some care to measure $R \approx 1$ accurately. It can be argued that absorption measurements are more appropriate than reflectance measurements for determining changes in the low frequency optical constants such as produced by a superconducting transition. In insulating compounds, the problem has to do with the Kramers-Kronig transform. In equation 2.7 one can see that in regions where the reflectance changes very little - where $\ln[R(\omega)/R(\omega_o)] \approx 0$ - the phase is determined mainly by the *extrapolation*.

As an illustrative example consider Si. A reflectance file was generated using equation 2.12 and the n and k values tabulated in Pallik's *Handbook of the Optical Constants of Solids* [19]. A variety of extrapolations, shown in figure 2.4, were

used for $\omega \geq 160000$ cm^{-1} to calculate the optical conductivity. The free electron asymptotic form, equation 2.18, was used above 10^7 cm^{-1} . Figure 2.5 shows that the extrapolation above 160000 cm^{-1} has a significant effect on the optical conductivity down to almost 10000 cm^{-1} . Si has 14 electrons in total while the conductivity sum rule yields $N_{eff}(400000 \text{ cm}^{-1}) = 23.3$, 14.1, and 10.6 electrons when assuming R proportional to ω^{-4}, ω^{-5}, and ω^{-6} respectively between 160000 and 10^7 cm^{-1} . Thus ω^{-4} is a poor extrapolation and there are a range of physically reasonable power laws between ω^{-5} and ω^{-6} yielding some uncertainty to the KK analysis. In summary, the example illustrates two points. One must carefully choose the high frequency extrapolation. Secondly, reflectance is not the best measurement in regions where there is little absorption. It is known that the lowest band gap in silicon is the indirect transition near 10000 cm^{-1} which is relatively weak compared to the direct transition near 30000 cm^{-1} . Transmission measurements are more appropriate to measure the fundamental band gap.

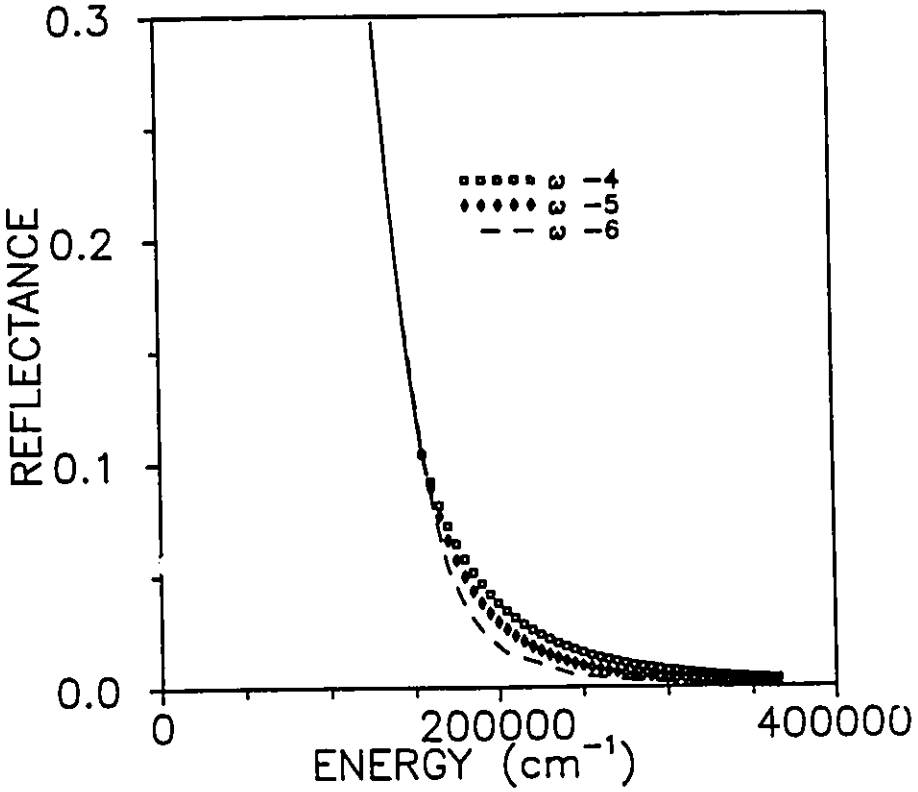

Figure 2.4: Power law extrapolations ($R \propto \omega^{-s}$; s=4,5,6) used between 160000 and 10^7 cm^{-1} to calculate the optical conductivity of Si.

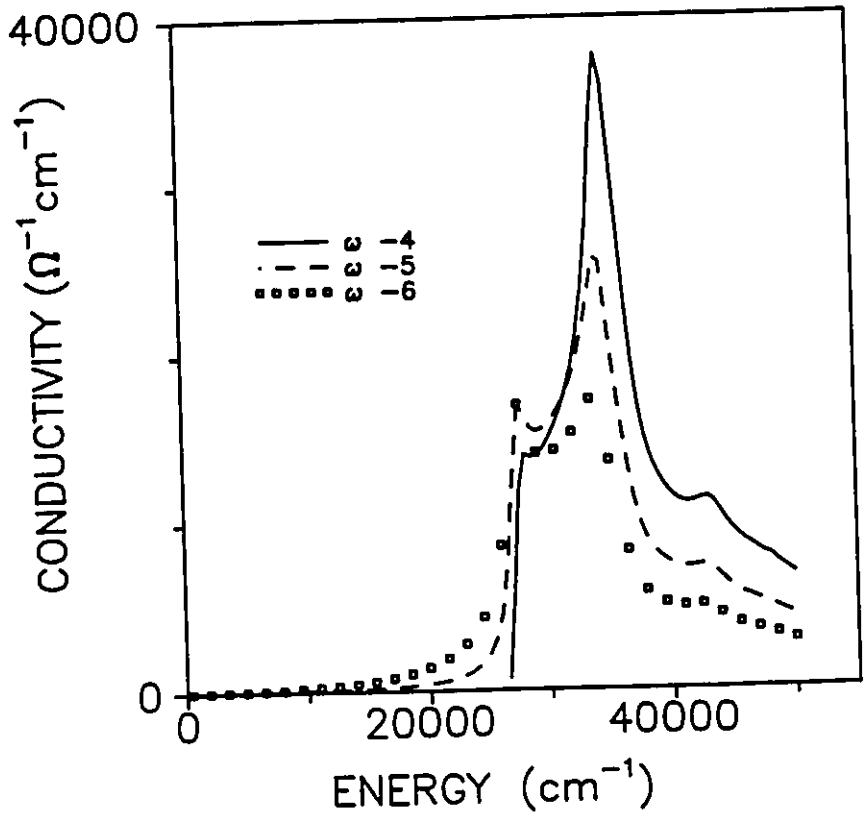

Figure 2.5: Real optical conductivity of Si determined by Kramers-Kronig transformation of the reflectance calculated using the power law extrapolations shown in figure 2.4

2.6 Apparatus

2.6.1 Spectrometers

Two different spectrometers were used for the reflectance measurements, a continuous scan Michelson interferometer for low frequencies (50-5500 cm^{-1}) and a grating spectrometer for higher frequencies (3800-40000 cm^{-1}). It was necessary to use a variety of lamps, detectors, beamsplitters and gratings to determine a single reflectance spectrum. These are listed in tables 2.1 and 2.2.

Table 2.1: Beamsplitter and Detector Combinations for the Michelson Interferometer

Range (cm^{-1})	lamp	Beamsplitter	Detector
50-220	mercury arc	12 μ Mylar	1.3K Si bolometer
110-720	ceramic glower	2 μ Mylar	4.2K Si bolometer
550-5500	tungsten-halogen	Ge coated KBr	77K HgCdTe

Table 2.2: Lamp, detector and filter Combinations for the Grating Spectrometer

Range (cm^{-1})	Lamp	Detector	Filter
3800-6300	tungsten-halogen	PbS (300K)	Ge
5500-10000	tungsten-halogen	PbS (300K)	Si
9200-16700	tungsten-halogen	Si photodiode	Red Glass
11000-23000	tungsten-halogen	photomultiplier	yellow glass
15000-30000	tungsten-halogen	photomultiplier	blue glass
20000-35000	deuterium	photomultiplier	purple glass
25000-40000	deuterium	photomultiplier	9863 glass

2.6.2 Reflectance Module

A reflectance module, which holds the sample and controls its temperature, is necessary to direct the incident light to the sample and reflected light to the detector. The reflectance module is composed of two parts: an optics table and the sample holder. An aperture is placed at the beginning of the optics table and mirror optics are used to form an image of the aperture on the sample (or reference mirror) as shown in figure 2.6. In the near infrared/ultraviolet system the reflected light is imaged by the reflectance module onto the entrance slit of the grating spectrometer; the detector sits at the exit slit.

The heart of the reflectance module is the sample holder attached to the optics table. The sample holder is built around a R.J. Hansen Hi-Tran continuous flow cryostat. The sample sits in the cubic evacuated chamber of the cryostat, allowing the sample temperature to be varied between approximately 10 and 300 K. The six ports leading from the sample chamber lead to (i) the cold-finger cryostat on which the sample sits (ii) the vacuum line (iii) vacuum gauge (iv) an *in situ* evaporator (v) a viewing port and (vi) the window separating the evacuated chamber from the the rest of the optical system appropriate for the spectrum being measured. For example, in the near-infrared to the ultraviolet, a quartz window is employed while in the far infrared a polypropylene window is used.

The sample and a reference mirror are mounted on adjacent sides of a copper block attached to the cold finger of cryostat. The cryostat sits on a thrust bearing allowing precision rotation of the sample or the reference mirror into the incident light beam. The positions are set by mechanical stops.

Different sample mounting devices are employed depending on the size of the samples. Small samples (under 2 mm a side) are mounted on the tip of a brass cone. The brass cones are attached to the cold finger by three screws, and for low temperature work, a copper braid. The cone geometry allows the complete surface

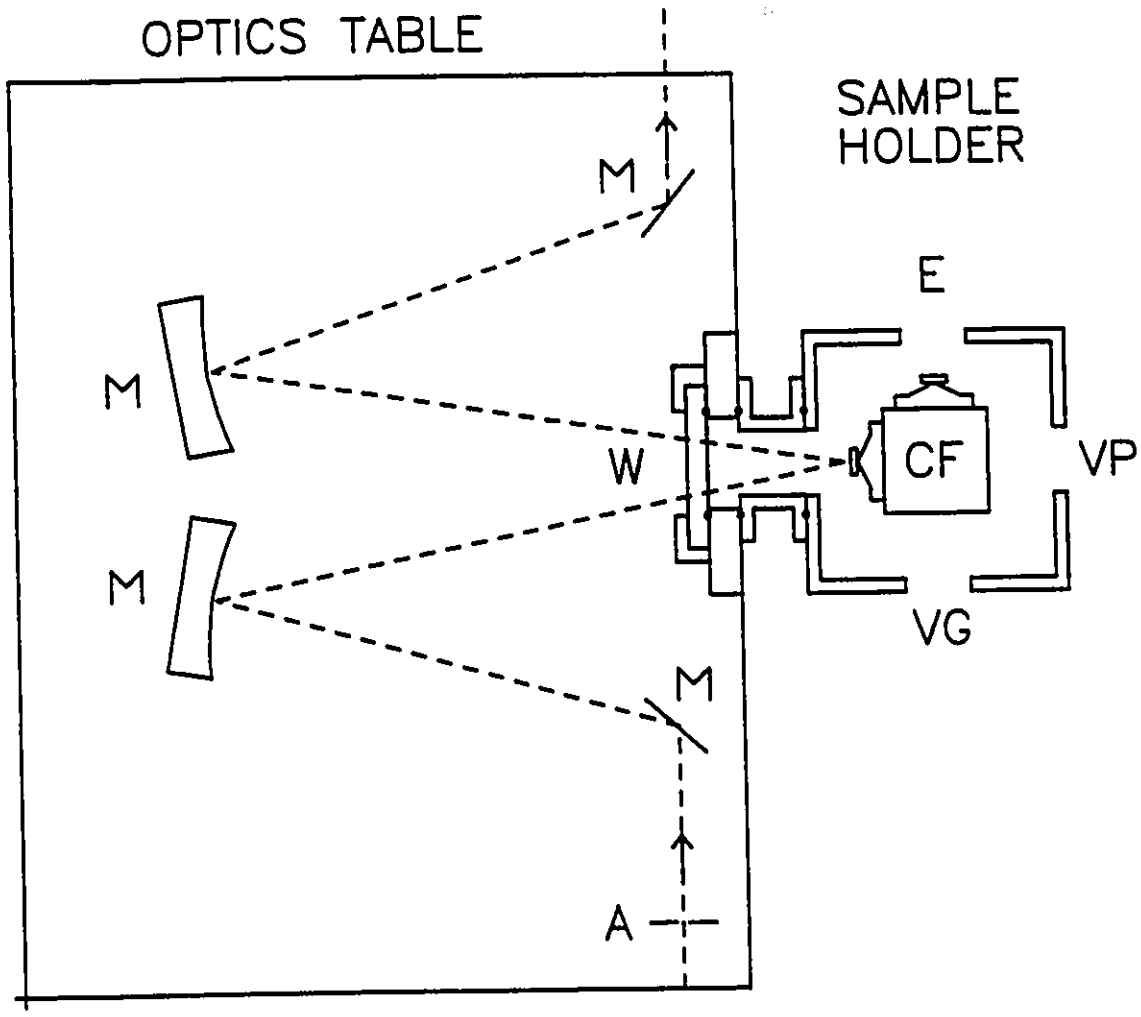

Figure 2.6: Reflectance Module for the grating spectrometer. The dashed line represents the light path. Light from the source shines on the aperture (A). It is directed and focussed by two mirrors (M) and passes through a quartz window (W) where it hits the sample. In the diagram, the sample is sitting on a brass cone attached to the copper cold finger (CF). After being reflected off the sample, light is directed towards the entrance of the grating spectrometer. The three other labelled ports to the evacuated sample chamber lead to the evaporator (E), the vacuum gauge (VG) and the viewing port (VP) which are not illustrated in the figure.

area of a small sample to be utilized: the image of the aperture is larger than the sample, but only light striking the sample is seen by the detector. Larger samples are mounted in the conventional manner on flat pieces where the image of the aperture is smaller than the sample.

2.6.3 Data Collection

Measurements of absolute reflectance are made in two stages. First, the power spectra of the sample P_{samp} and reference mirror P_{ref1} are obtained at various temperatures. Then the sample is returned to room temperature and rotated so that it faces a tungsten evaporator coil from which hang either gold or aluminum wires (for $\omega \leq$ 17000 or $\geq$ 15000 cm^{-1} respectively). Hanging the appropriate amount of material and running approximately 3 A through the coil produces a film thick enough to prevent transmission but thin enough to retain the surface morphology of the sample. The power spectrum of the coated sample (P_{coat}) and reference P_{ref2} are determined at the same temperatures as during the first thermal cycle. The absolute reflectance of the sample R_{abs} is given by the following formula, where $R_{al,au}$ is the accepted reflectance of the overcoating material [19].

$$R_{abs} = \frac{P_{samp}}{P_{ref1}} \times \frac{P_{ref2}}{P_{coat}} \times R_{al,au} \tag{2.23}$$

The overcoating procedure corrects for any extra scattering due to surface roughness and also for any residual optical misalignment. The vacuum in the sample chamber is $\approx 10^{-5}$ torr, good enough for high quality films. The films were checked from time to time by a multiple reflectance technique for absolute reflectance and by measuring the reflectance of well-known materials such as silicon (see figure 2.7). The overcoating procedure allows the absolute reflectance to be determined to within one percent between 50 and 700 cm^{-1} and to within two percent at higher frequencies.

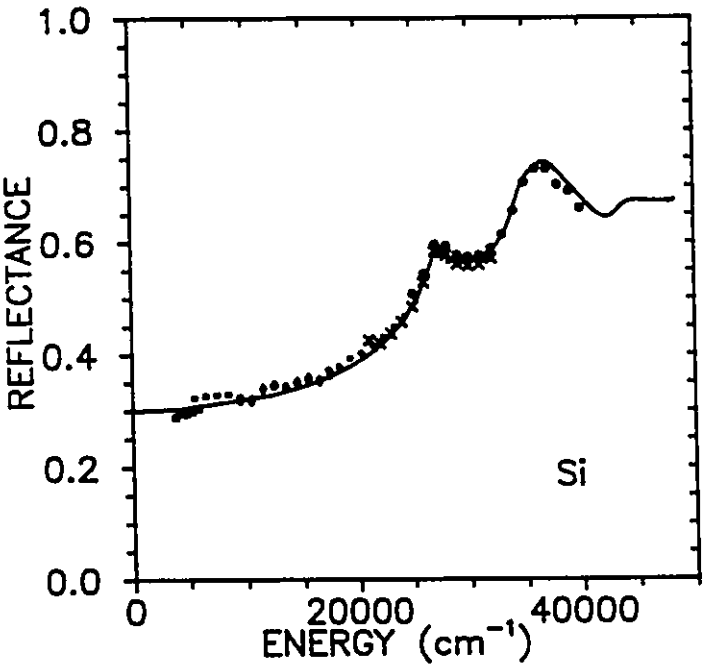

Figure 2.7: Reflectance of Si measured using the grating spectrometer (dots, circles and crosses) compared with literature values (solid line) compiled in reference [19]. The literature measurements are on large optical flats where it is easy to get a good absolute value. Our data is for millimeter size chips in a cryostat.

Chapter 3

Electronic Structure

3.1 Cubic Perovskite Band Structure

The electronic structure of many solids can be determined using the one electron approximation where the true many body Schrodinger equation:

$$H\Psi = \sum_{i=1}^{N}\{-\frac{\hbar^2}{2m}\nabla_i^2\Psi - Ze^2\sum_{\mathbf{R}}\frac{1}{|\underline{r_i} - \underline{R}|}\Psi\} + \frac{1}{2}\sum_{i\neq j}\frac{e^2}{|r_i - r_j|}\Psi \tag{3.1}$$

is replaced by N one-electron Schrodinger equations[20],

$$-\frac{\hbar^2}{2m}\nabla_i^2\psi_i + U(r)\psi(r) = \epsilon_i\psi_i(r) \tag{3.2}$$

The art of band structure calculations is to choose astutely $U(r)$ and appropriate basis functions so that the one-electron band structure best agrees with the available experimental data such as transmission, which can determine the fundamental band gap of an insulator, or cyclotron resonance which measures the effective mass of free carriers, a quantity related to the curvature of the conduction band [21].

To begin to understand the electronic structure of the rare earth titanites it is appropriate to examine the band structures of various cubic perovskites. Figure

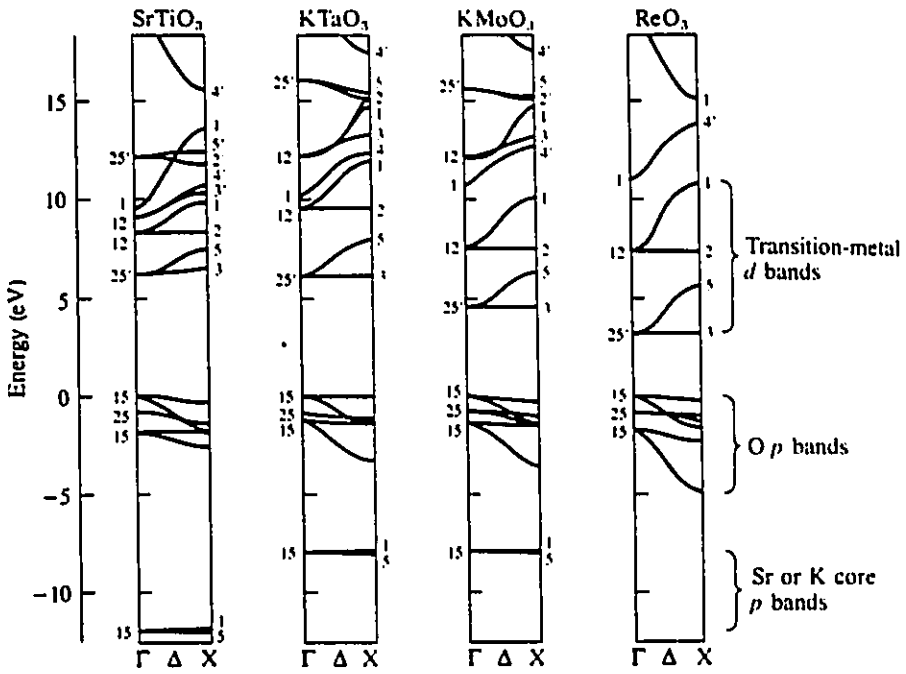

Figure 3.1: Band Structures of Various Perovskites in the 001 direction of the Brillouin Zone. From reference [22].

3.1 shows that the band structures [22] of many early transition metal perovskites are similar. In these compounds one can generally predict whether the material will be metallic or insulating by simply filling states in a rigid band picture. For example in ReO_3 the cation (Re) has seven electrons outside a Xe core (one more than required to fill the O(2p) orbitals) and one would predict metallic behaviour. This is indeed the case as the conductivity of ReO_3 rivals that of copper [23]. Other examples are listed in table 3.1. Note that $LaTiO_3$, the most metallic $RTiO_3$ compound has a much higher resistivity than either $SrVO_3$ or ReO_3 suggesting the electrons are not as itinerant as in the latter two compounds.

Table 3.1: Comparison of 'electron counting' predictions of transport properties with measured dc resistivity

Compound	number of e^- outside cores	prediction	ρ_{300K} mΩcm
$SrTiO_3$	6	ins.	$\approx 10^4$ [24]
ReO_3	7	met.	0.017 [23]
$SrVO_3$	7	met.	0.4 [25]
$LaTiO_3$	7	met.	90 [26]

The band structure of $LaTiO_3$ (assuming the cubic perovskite structure) has been calculated by David Singh of the Naval Research Laboratory in Washington using the general potential extended linear augmented plane wave (LAPW) method [27]. In this method the one electron wave function is represented by a finite number of plane waves between ions while it is forced to have more oscillatory behaviour in the core region. The result of the calculation appears in figure 3.2 where one can see that the band structure in the $\Gamma - X$ direction is similar to those shown in figure 3.1. Secondly note that Fermi level cuts a band near the zone center: a metallic state is predicted in agreement with the electron counting rule discussed above. The orthorhombic distortion - the rigid rotation of the cornershared TiO_6 octahedra - was ignored in the calculation and will be considered below.

(a)

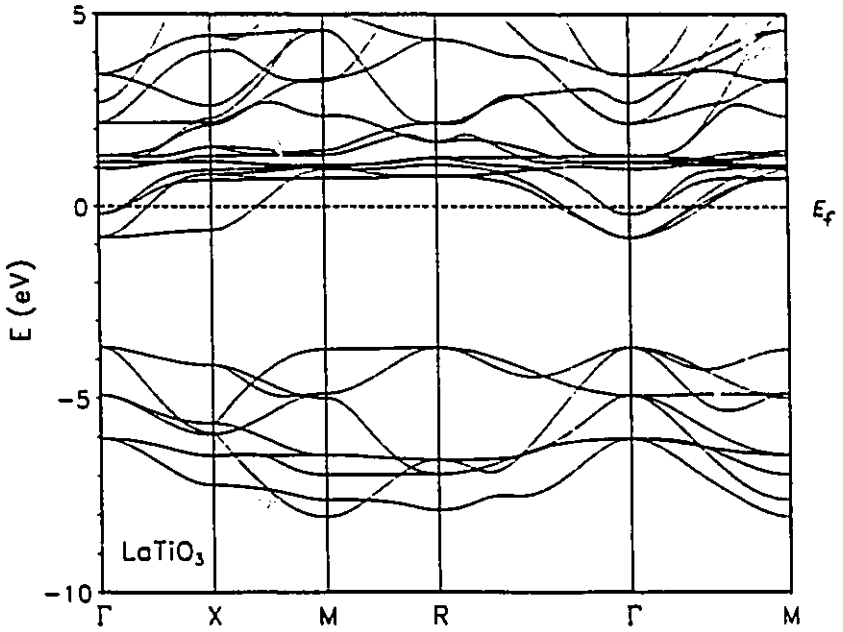

(b)

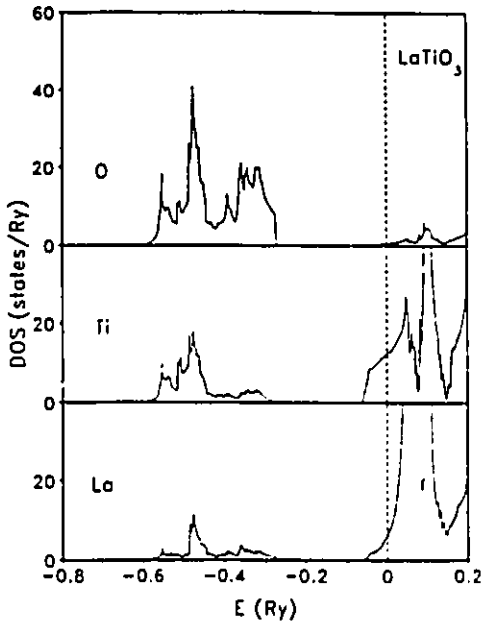

Figure 3.2: (a) Band Structure of $LaTiO_3$ assuming cubic perovskite structure. (b) Contribution of each atom to the density of states. Reference [27].

3.2 The Hubbard Model

Mott was the first to suggest that when the energy required to put two electrons on one site (U) is greater than the bandwidth, the Bloch-Wilson band theory is not appropriate. Hubbard, using a highly simplified model, demonstrated how a large U could induce a compound with a half-filled band into an insulating state. Hubbard proposed that the following Hamiltonian contains the essential physics of a set of electrons which have intersite transfer integrals T_{jk} and where it takes an extra energy U to put two electrons on one site [28].

$$H = \sum_{j,k\sigma} T_{jk} c^{+}_{j\sigma} c_{k\sigma} + \frac{1}{2} U \sum_{j,\sigma} n_{j\sigma} n_{j,-\sigma} \tag{3.3}$$

$c_{j\sigma}$ is the annihilation operator for an electron with spin σ located on site j while $c^{+}_{k\sigma}$ is the creation operator for an electron of spin σ located on site k. T_{jk} is the hopping matrix element between sites j and k. The bandwidth (W) for Bloch electrons will increase as T_{jk} increases.

One of the questions that Hubbard considered was,"what happens to the density of quasi-particle states $\rho(E)$ in the presence of large U ?" He answered this in the following manner. One knows that n_σ, the mean number of electrons per atom of spin σ is given by:

$$n_\sigma = \int_{-\infty}^{\infty} \rho_\sigma(E) \frac{dE}{e^{\beta(E-\mu)} + 1} \tag{3.4}$$

To find an expression for $\rho_\sigma(E)$ one first finds an expression for n_σ. In second quantized notation n_σ is given by

$$n_\sigma = \frac{1}{N} \sum_{j} \langle c^{+}_{j\sigma} c_{j\sigma} \rangle \tag{3.5}$$

where the Green's function technique is used to determine the expectation value

$(c^+_{j\sigma}c_{j\sigma})$ in equation 3.5. The Hamiltonian 3.3 determines the structure of the one-particle Green's function G(j,k) = $i\langle N|Tc_{j\sigma}c^+_{k\sigma}|N\rangle$ and equation 3.5 becomes,

$$n_\sigma = \frac{i}{N}\lim_{\epsilon\to 0^+}\sum_j \int [G^\sigma_{jj}(E+i\epsilon) - G^\sigma_{jj}(E-i\epsilon)]\frac{dE}{e^{\beta(E-\mu)}+1} \tag{3.6}$$

where $G^\sigma_{jk}(E)$ is the fourier transform of the one particle Green's function. By comparing equations 3.5 and 3.6 one sees that

$$\rho_\sigma(E) = \frac{i}{N}\lim_{\epsilon\to 0^+}\sum_j [G^\sigma_{jj}(E+i\epsilon) - G^\sigma_{jj}(E-i\epsilon)] \tag{3.7}$$

In the case of zero bandwidth, where the band energy of each electron is T_0, after determining $G^\sigma_{jj}(E)$, the density of states is given by:

$$\rho_\sigma(E) = (1-\frac{1}{2}n)\delta(E-T_0) + \frac{1}{2}n\delta(E-T_0-U) \tag{3.8}$$

The calculation shows that the system behaves as though it has two energy levels T_0 and T_0+U containing $1-\frac{n}{2}$ and $\frac{n}{2}$ states per atom respectively. The chemical potential is T_0 until half filling when it suddenly jumps to T_0+U. A half-filled band ($n=1$) is split into filled lower and empty upper Hubbard subbands, and the system behaves as an insulator.

Note that the density of states in the upper Hubbard subband depends on the site occupation. This implies that doping a Mott- Hubbard insulator has a profound influence on the density of states. Consider an N-site system where one can change the site occupation by some doping process. There are 2N states associated with the N sites. This is a fixed quantity but the way in which they are distributed between the upper and lower Hubbard subbands depends on the occupation of the sites (n). The number of states in the upper subband is equal to the number of possible ways of putting two electrons on one site. Thus, if all the sites are occupied, there are N states in both subbands. If we remove an electron from the system (hole doping), we destroy a state in the upper subband because there are only N-1 ways of placing two

electrons on one site. The same thing happens if we add an electron to the system. There are now N-1 states in the upper band and N+1 states in the lower band. This transfer of spectral weight from high to low frequencies is one of the most significant experimental signs of a highly correlated insulator [75] and is very different from doping a semiconductor where the density of states is a rigid quantity.

3.3 The ZSA Framework

Zaanen, Sawatsky and Allen (ZSA) showed that there is another energy besides W and U which determines the electronic structure of a solid near the Fermi energy in ionic compounds: the charge transfer energy Δ, which is the energy associated with cation-anion charge transfer [29]. In transition metal oxides Δ would be the energy required to transfer an electron from an oxygen $2p$ type orbital into a metallic d state. The ZSA framework provides an answer to the puzzling observation that NiO is an insulator while NiS undergoes a metal-insulator transition [32]. There is no reason for a large reduction in the Ni(3d)-Ni(3d) U when substituting sulphur for oxygen. When Δ is considered, one realizes that U can be bigger than W and the sample can still be metallic if $\Delta \leq U$. Thus, in the ZSA framework there are two types of magnetic insulators: charge transfer insulators where Δ is smaller than U and Mott insulators where the smallest gap is U. These two types of electronic structure are illustrated schematically in figure 3.3.

Torrance *et al.* studied the ZSA framework by using a simple ionic model to estimate U and Δ for 76 simple and perovskite oxides [30]. The ionic model is a lattice of ions having integer oxidation states. Many phenomena are ignored: lattice relaxation, ionic polarizability, covalency, crystal field splittings, screening and electronic polarizability.

U is the energy required to transfer an electron from one transition metal cation to its neighbour a distance d_{M-M} away and is given by the following formula

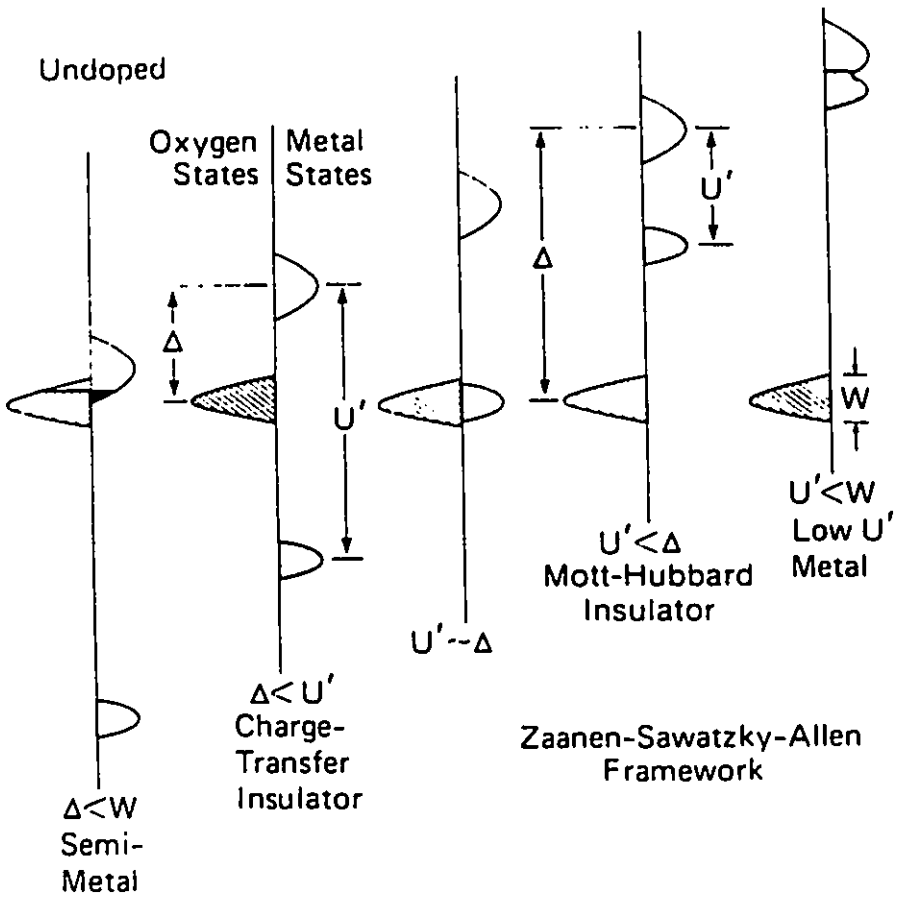

Figure 3.3: Classification of electronic structure in the in the ZSA framework. From reference [30].

which incorporates the ionization potential $I_{v+1}(M)$ and electron affinity $A = -I_v(M)$ of M^{v+}:

$$U_o = I_{v+1}(M) - I_v(M) - e^2/d_{M-M} \tag{3.9}$$

Δ, the energy required to excite an electron from O^{2-} to a cation a distance d_{M-O} away depends on the ionization potential of O^{2-} (the negative of the electron affinity $A(O^-)$) and the cation electron affinity $A(M) = -I_v(M)$ as well as the term ΔV_M which is the difference in Madelung site potentials between the cation and anion sites:

$$\Delta_o = \Delta V_M - I_v(M) - A(O^-) - e^2/d_{M-O} \tag{3.10}$$

The subscript zero indicates that these are ionic model calculations. The major assumption is that the *differences* in Δ and U are due primarily to differences in ionization and Madelung potentials. The neglected effects will reduce Δ and U from the ionic values Δ_o and U_o.

Their results are shown in figure 3.4 which is taken from Torrance *et al.* [30]. A particular compound is placed on the diagram according the U and Δ values calculated using equations 3.9 and 3.10 with a symbol indicating whether it is a metal, an insulator or exhibits a metal- insulator transition. For the purposes of figure 3.4 Torrance *et al.* considered a material to be a metal if its dc conductivity is greater than 1 S/m at 300K. The remarkable feature of this plot is the appearance of boundaries, $U_B \approx 11$ eV and $\Delta_B \approx 10$ eV, separating metallic from insulating oxides [30]. The rare earth titanites for which $U_o = 12.2$ and $\Delta_o = 15.8$ lie closer to the U rather than the Δ boundary suggesting insulating $RTiO_3$ compounds are Mott rather than charge transfer insulators.

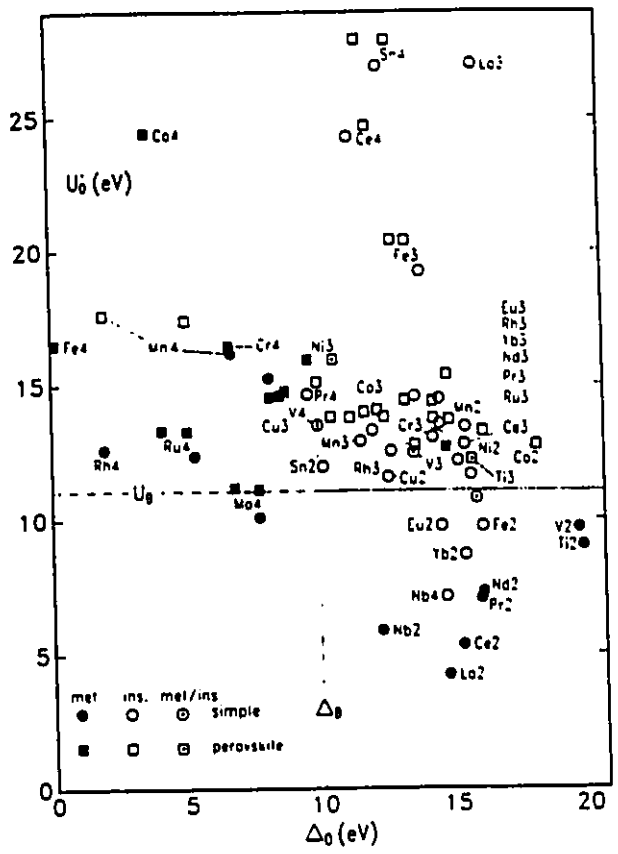

Figure 3.4: Calculated values of Correlation Energy U and Charge Transfer Energy Δ for various transition metal oxides. The lines U_B and Δ_B attempt to separate the "insulators" from the "metals". From reference [30].

3.4 Optical Determination of Δ and U

Systematic studies of transition metal oxides have shown that, in general, the early transition metal oxides (Ti,V) are Mott-Hubbard insulators while the late transition metal oxides and sulphides (Fe,Ni,Cu) are charge transfer insulators [31]. NiO which for a long time was considered the prototypical Mott insulator is actually a charge transfer insulator [2]. In this section optical methods for measuring Δ and U will be discussed.

In X-ray Photoemission Spectroscopy (XPS), holes are created in core levels. If the interaction between the core hole and the valence electrons is strong enough, satellites will be observed in the XPS spectrum. Consider the Cu(2p) core level spectra for CuO and Cu_2O shown in figure 3.5 (a) [33]. In CuO, copper is in a d^9 configuration with one empty d level. In Cu_2O, the copper d states are completely filled (d^{10} configuration). Note that there are satellite lines in the CuO spectrum which are explained by saying that before the electron is photoexcited, an electron is transferred from O(2p) to a Cu($3d^9$) atom. The absence of satellites in the Cu_2O spectrum is because the anion-cation charge transfer is impossible. The satellite splitting U_{split} is due to the different Coulomb energies between the core hole and 9 Cu(3d) electrons and the core hole and 10 Cu(3d) electrons and is related to the $d-d$ U.

The layered cuprates are good materials to illustrate measurements of Δ and U. There is general consensus that the antiferromagnetic insulating parent compounds to the the high T_c superconductors are charge transfer insulators. A peak in the reflectance spectrum of the insulating parent compounds at approximately 1.5 eV [34, 35, 36] has been associated with the the charge transfer gap. The XPS spectrum for various high T_c oxides [37] is shown in figure 3.5 from which $U \approx 8.5$ eV can be extracted.

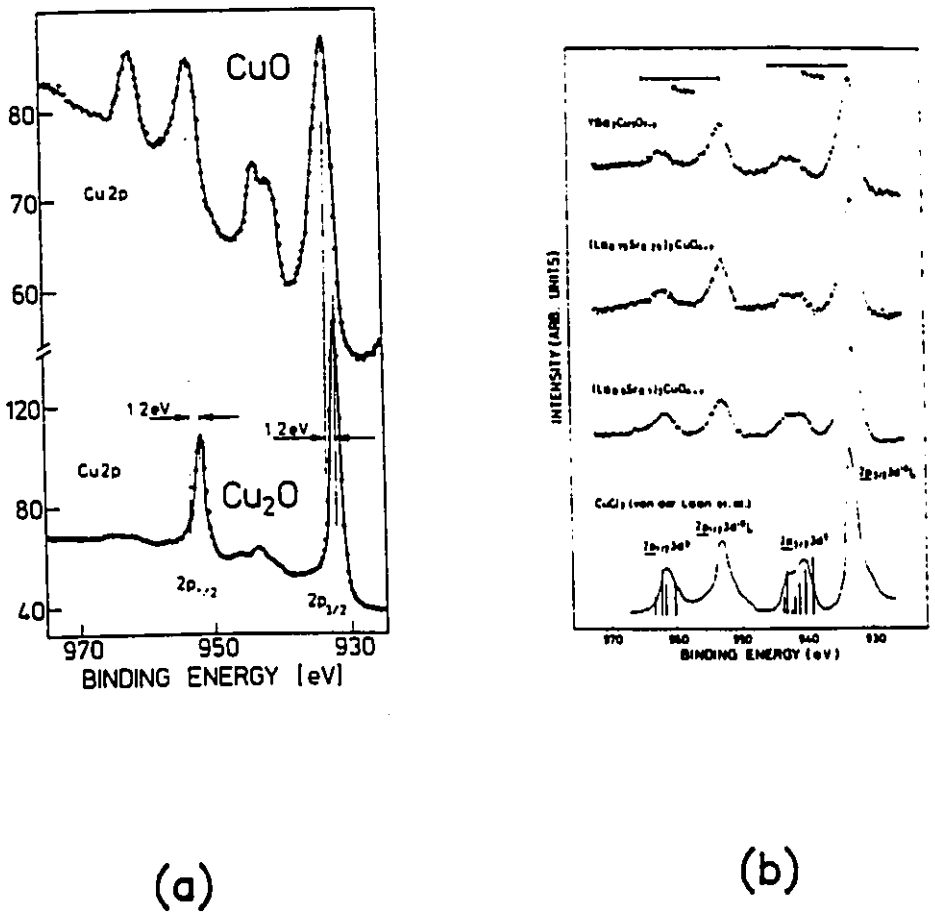

Figure 3.5: (a) XPS spectrum of the Cu $2p_{1/2}$-$2p_{3/2}$ core levels in CuO and Cu_2O. The CuO spectrum shows strong satellites. (b) XPS spectrum of various high T_c cuprates. $U \approx 8.5$ eV can be extracted from the spectrum. From reference [33].

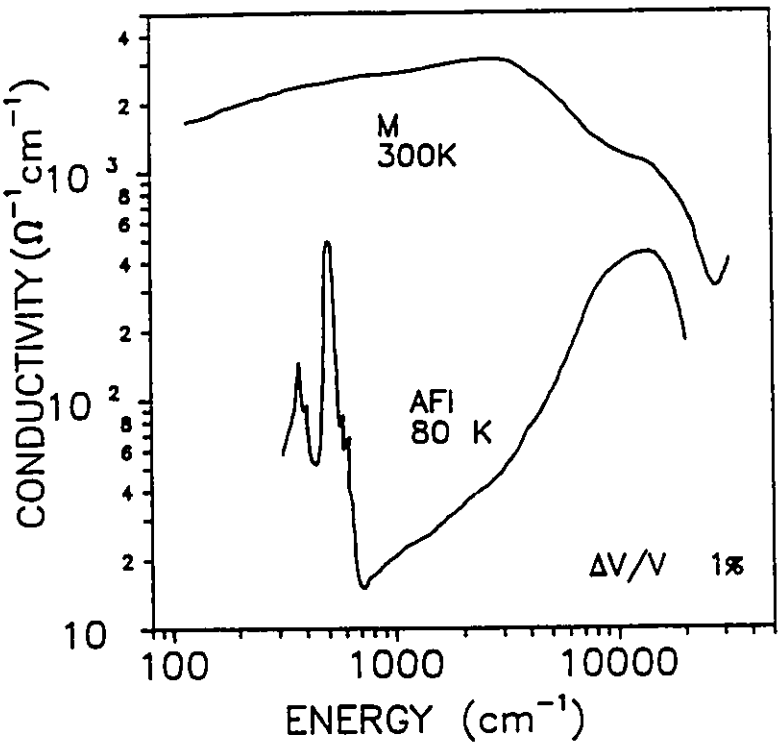

Figure 3.6: Optical conductivity of V_2O_3 in the AFI and metallic regimes. From reference [38]

As well as providing a means to measure Δ in charge transfer insulators, reflectance spectroscopy can be used to observe U. Consider the Mott-Hubbard insulator V_2O_3 which undergoes a transition from a high temperature metallic state (M) to an antiferromagnetic insulating state (AFI) at 150 K. The frequency dependent real optical conductivity, obtained by Kramers-Kronig transformation of reflectance data [38] appears in figure 3.6. One can see that the low frequency conductivity of the metallic phase is suppressed in the AFI phase where there is a gap like feature. The electrical conductivity of antiferromagnetic V_2O_3 has a fairly well defined activation energy of 0.1 eV whereas there is no sharp onset of absorption in figure 3.6. Barker *et al.* suggest this indicates a well defined mobility edge in a slowly varying density of states [38].

3.5 Brinkmann-Rice Metal Insulator Transition

Gutzwiller, and Brinkmann and Rice studied the Hubbard Hamiltonian 3.3 from a slightly different point of view and found that it predicts a metal-insulator transition as the average electron density approaches one per site [39]. They start from the metallic side and perform a variational calculation assuming a trial wavefunction which incorporates the effect of the on-site Coulomb repulsion which dislikes doubly occupied sites. Letting $\tilde{\eta}$ be a variational parameter to be determined by minimizing the energy and $|\Phi_o\rangle$ be the conventional ground state for non-interacting electrons, Gutzwiller's wavefunction is [40]:

$$|\Psi_G\rangle = \prod_i (1 - \tilde{\eta} n_{i\sigma} n_{i-\sigma}) |\Phi_o\rangle \tag{3.11}$$

In the limit $U \rightarrow \infty$, it can be shown [40] that the Hamiltonian 3.3 reduces to :

$$H = \sum_{ij\sigma} \gamma_\sigma t_{ij} c^+_{i\sigma} c_{j\sigma} \tag{3.12}$$

where γ_σ reduces the hopping matrix elements (narrows the band or enhances the mass) by a factor related to the band filling factor (z). $z = \frac{1}{2}$ means a half-filled band, or one electron per site on average.

$$\gamma_\sigma = \frac{1 - 2z}{1 - z} \tag{3.13}$$

In this limit, the electrons cannot move anywhere when there is one electron per site ($z = \frac{1}{2}$) and the system behaves as an insulator.

Another interesting limit is to assume finite U and $z = \frac{1}{2}$. In this case it can be shown [39] that the effective mass of the carriers diverges as U approaches a critical value U_c related to the bandwidth:

$$m^*/m = [1 - (U/U_c)^2]^{-1} \tag{3.14}$$

3.6 Summary

Historically, two different approaches have been used to examine the effects of short-range Coulomb repulsion on a system containing one electron per site [41] and two different effects are predicted in a system where $U \approx W$. On the insulating side of the transition, a system with a half-filled band containing 2N states behaves like a system containing one filled and one empty band each containing N states. On the metallic side of the transition, the effective mass of the carriers is enhanced. The calculations of Torrance *et al.* have suggested that $RTiO_3$ perovskites are Mott-Hubbard insulators. Let us now examine the optical properties of the the light rare earth titanites and the insulator-metal transition in doped $LaTiO_3$ in light of the Hubbard and Brinkman-Rice models.

Chapter 4

Insulating Rare Earth Titanites

4.1 Sample Preparation

$NdTiO_3$ and $CeTiO_3$ were prepared by a three step process. First the rare earth and titanium oxides were mixed according to the following reactions:

$$CeO_2 + TiO \rightarrow CeTiO_3 \tag{4.1}$$

$$Nd_2O_3 + Ti_2O_3 \rightarrow NdTiO_3 \tag{4.2}$$

Before weighing, the rare earth oxides - Rhône-Poulenc CeO_2 (99.9 %) and Nd_2O_3 (99.99 %) - were heated in alumina crucibles at $\approx$ 1000°C in air overnight before weighing. TiO was prepared by arc melting equimolar amounts of Ti metal with TiO_2 under an argon atmosphere. The stoichiometry of the TiO was determined by measuring the weight gain upon heating TiO in an oxygen atmosphere. Titanium sesquioxide (99.9 %) was manufactured by CERAC.

Secondly, polycrystalline $RTiO_3$ was obtained by arc melting the starting materials under an argon atmosphere. Finally, single crystals were prepared by Jim Garrett using the Czochkralski technique: The polycrystalline material was melted in the water-cooled hearth of a modified Reed type Tri-arc furnace [42] and, using a

Tungsten rod as a seed, the crystal was pulled from the melt. In the triarc furnace, both the hearth and the crystal can rotate, and one has the option of rotating them in opposite directions.

The remaining samples ($LaTiO_3$, $PrTiO_3$, $SmTiO_3$ and $GdTiO_3$) were prepared by Dr. J.E. Greedan's previous graduate students using techniques discussed in D.A. MacLean's Ph. D. thesis [43].

The phase purity and lattice spacings of the samples were checked using a Guinier camera. No impurity phases were observed and the lattice constants listed in table 4.1 agree with previous measurements [44].

Table 4.1: Lattice constants of the $RTiO_3$ samples studied in this thesis. All entries are in Å, except for volume ($Å^3$)

Sample	a	b	c	Volume
La	5.6058(7)	5.6025(7)	7.914(1)	249.43(3)
Ce	5.6023(7)	5.5867(9)	7.869(1)	246.29(4)
Pr	5.6151(5)	5.5548(7)	7.8308(6)	244.25(3)
Nd	5.5800(8)	5.5000(11)	7.8000(13)	239.38(6)
Sm	5.6585(6)	5.4588(6)	7.7295(7)	238.75 (3)
Gd	5.7000(8)	5.4100(12)	7.6800(13)	236.83(4)

For $CeTiO_3$ and $NdTiO_3$ two types of chemical analysis were employed. Neutron activation analysis, which gives an estimate of the cation ratio, gave somewhat anomalous results listed in Table 4.2. Heating the samples in oxygen to 1000°C causes $CeTiO_3$ ($NdTiO_3$) to pick up one (one half) oxygen atom per formula unit.

Table 4.2: Chemical Analysis of $CeTiO_3$ and $NdTiO_3$ samples. Cation ratios were determined by neutron activation analysis. Weight gains were measured while heating the samples to 1000°C in air.

sample	R:Ti (NAA)	expected gain	measured gain
$CeTiO_3$	1.15 ± 0.06	6.8 %	7.4 ± 0.5 %
$NdTiO_3$	1.07 ± 0.03	3.4 %	3.4 ± 0.5 %

4.2 Mid- to Near-Infrared Results: Electronic Properties

4.2.1 Reflectance

Figure 4.1(a) presents the room temperature mid- to near-infrared reflectance of six rare earth titanites. The most important feature in these spectra is the systematic blue shift of a midinfrared peak with decreasing rare earth ionic radius indicated by the arrows. Figure 4.1(b) shows the reflectance of $LaTiO_3$ and $SmTiO_3$, up to 4 eV. The increase in reflectance one can see above 3 eV was exhibited by all the light $RTiO_3$. In fact a reflectance peak near 4 eV is common to many compounds containing TiO_6 octahedra, as can be seen in figure 4.2 and has been attributed to a charge transfer excitation from O(2p) type orbitals to Ti(3d) type orbitals [45]. This assignment is supported by band structure calculations [22]. The far-infrared reflectance spectra and the vibrational properties will be presented and discussed in section 4.3.

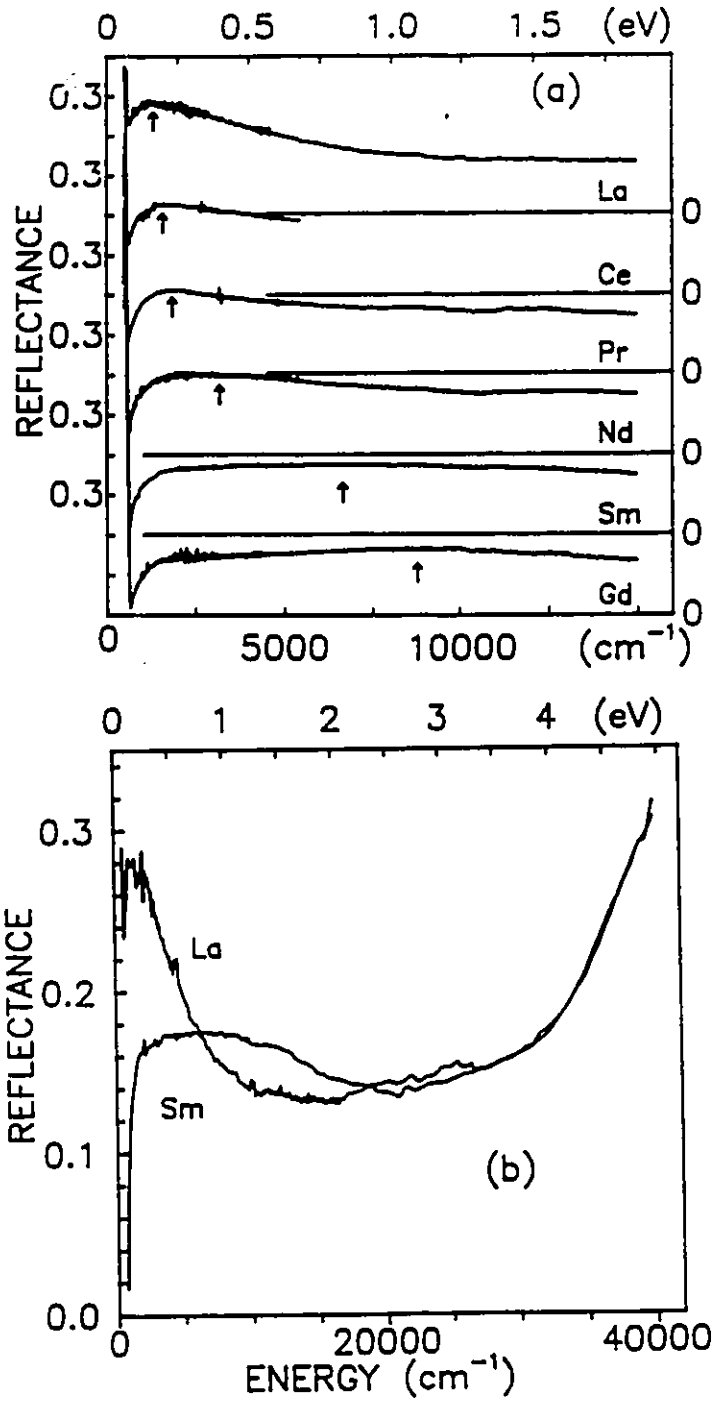

Figure 4.1: (a)Infrared Reflectance of the Insulating Rare Earth Titanites (b)Visible Reflectance of $LaTiO_3$ and $SmTiO_3$

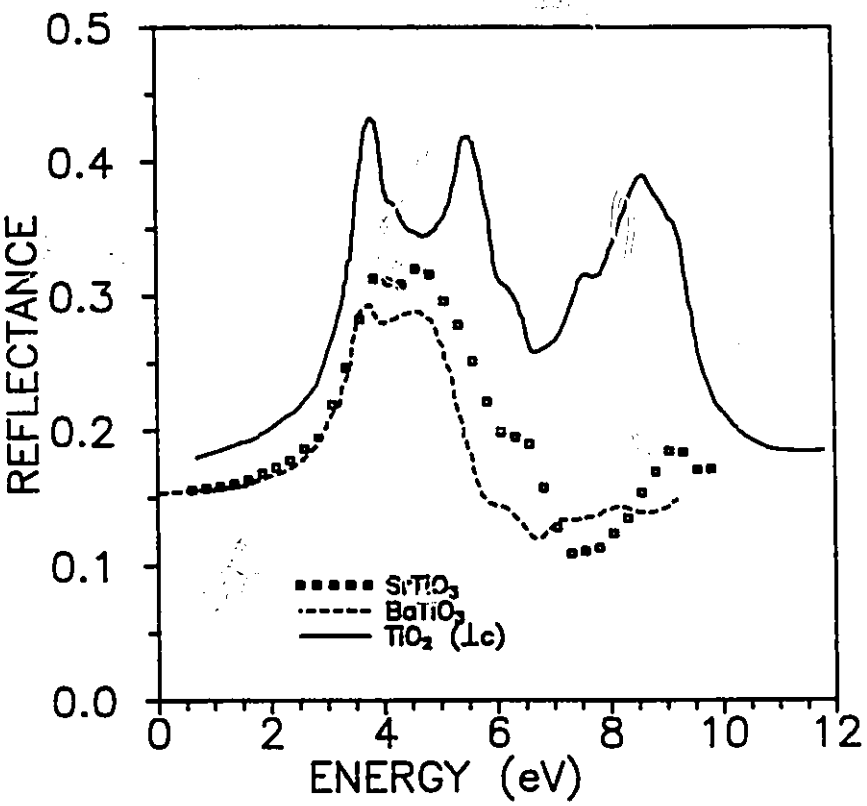

Figure 4.2: Reflectance of various compounds containing TiO_6 octahedra as measured by Cardona, reference [45].

Table 4.3: Low frequency constant reflectance (R) extrapolations for the Kramers-Kronig analysis.

Sample	$R(\omega \rightarrow 0)$
La	0.60
Ce	0.52
Pr	0.54
Nd	0.53
Sm	0.46
Gd	0.46

4.2.2 Optical Conductivity

High and low frequency extrapolations were constructed in order to calculate the optical constants using Kramers-Kronig (KK) analysis. The reflectance spectra were extended below the far infrared by the constants listed in the table 4.3.

In order to estimate the uncertainty in the KK analysis, the phase was calculated using different high frequency extrapolations. Between 40000 and approximately 200000 cm^{-1} two different extrapolations, shown in figure 4.3, were utilized. Neither the reflectance of $SrTiO_3$ measured by Cardona [45] nor the reflectance of an oxidized sample of $LaTiO_3$ measured by Fujishima *et al.* [46] agree very well with the present measurements of nominally stoichiometric $LaTiO_3$. One does not expect $SrTiO_3$ to agree but one should expect better agreement with doped $LaTiO_3$. Fujishima *et al.* did not use an overcoating procedure and as a consequence their measurements are less accurate than the present ones. Scattering losses due to surface roughness assume increasing importance with higher incident photon energy. For the KK analysis, the $SrTiO_3$ data were shifted to make the edges near 35000 cm^{-1} match while the doped

$LaTiO_3$ data was multiplied by 1.3. It is apparent that the free electron region begins above 160000 cm^{-1} since the reflectance is increasing at the end of both Cardona's and Fujishima's spectra. The extrapolations between 160000 and 200000 cm^{-1} shown in figure 4.3 were generated using one Lorentzian oscillator. Between 200000 cm^{-1} and the free electron region ($\omega \geq 10^6$ cm^{-1}), the reflectance was assumed to vary as ω^{-s} where s is some constant.

The high frequency extrapolation (even the choice of s) cm^{-1} had a significant effect on the optical constants down to nearly 10000 cm^{-1} and is due to the fact that the phase in a relatively flat part of the reflectance spectrum is determined by the reflectance at distant frequencies. Figure 4.4 shows the frequency dependent real optical conductivity in the region where there is little uncertainty in the KK analysis. The blue shift of the onset of the midinfrared absorption can be seen clearly.

The optical conductivity calculated using the two extrapolations of figure 4.3 and ω^{-5} between 200000 and 10^6 cm^{-1} is shown for $LaTiO_3$ and $SmTiO_3$ in figure 4.5. $LaTiO_3$ has 25 valence electrons. For $LaTiO_3$, both extrapolations give similar and physically reasonable values of N_{eff} (800000 cm^{-1}) $\approx$ 18. As can be seen in figure 4.5 one cannot be sure if the mid-infrared band excitations are separated cleanly from the charge transfer excitation above 30000 cm^{-1}.

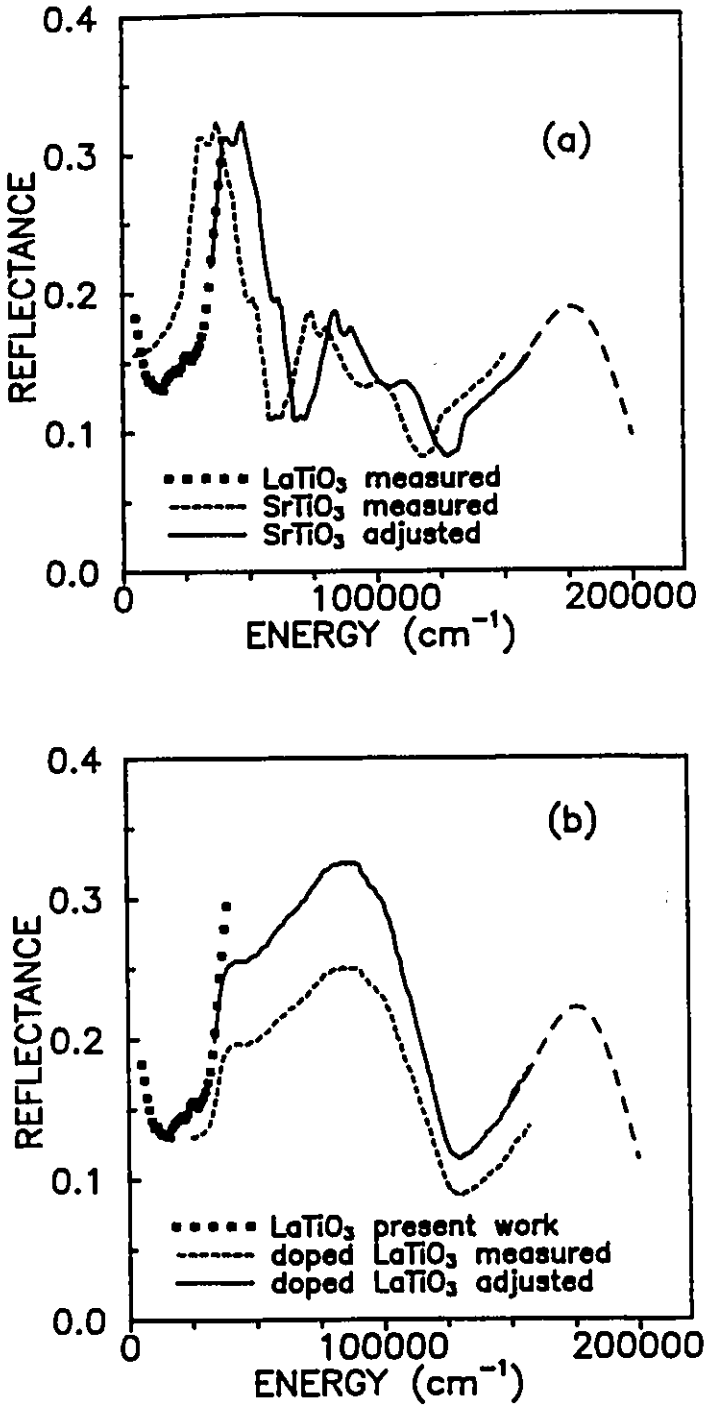

Figure 4.3: High Frequency extrapolations employed for the Kramers-Kronig Analysis

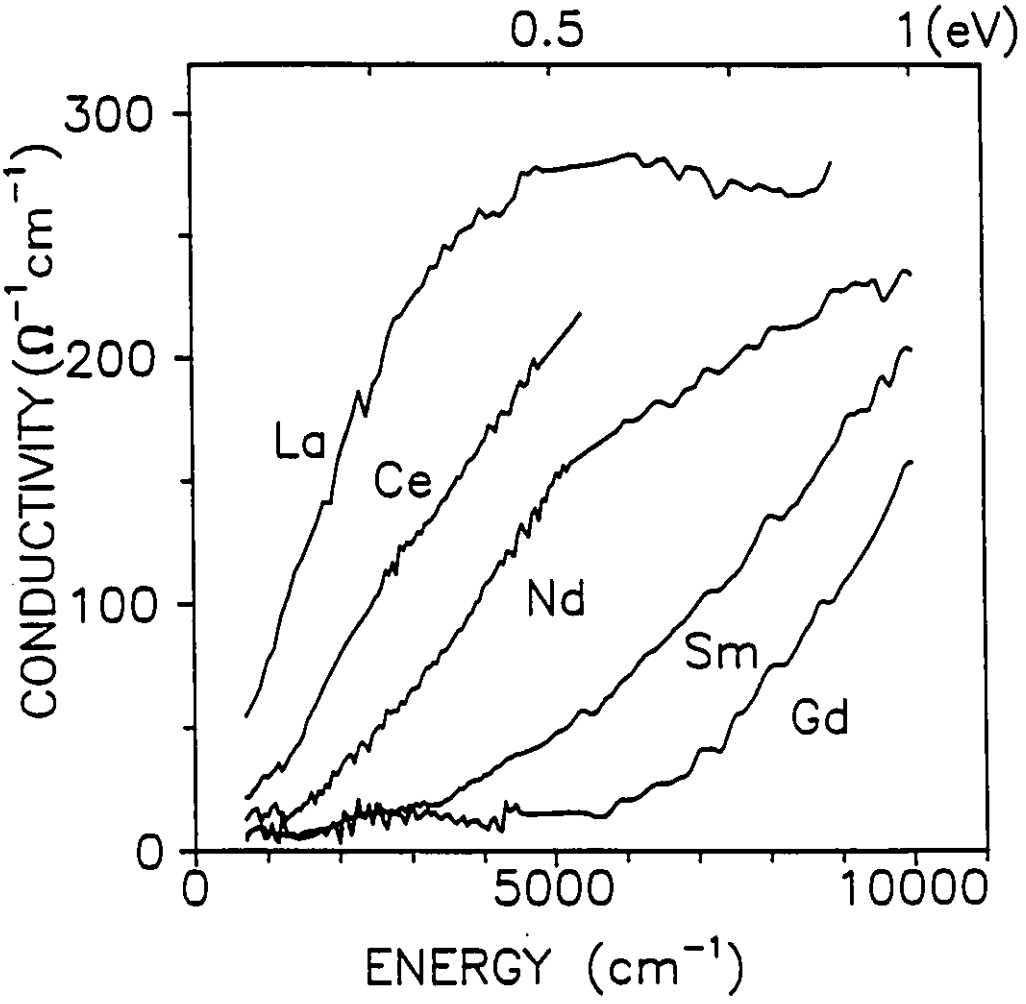

Figure 4.4: Frequency dependent real optical conductivity of the rare earth titanites.

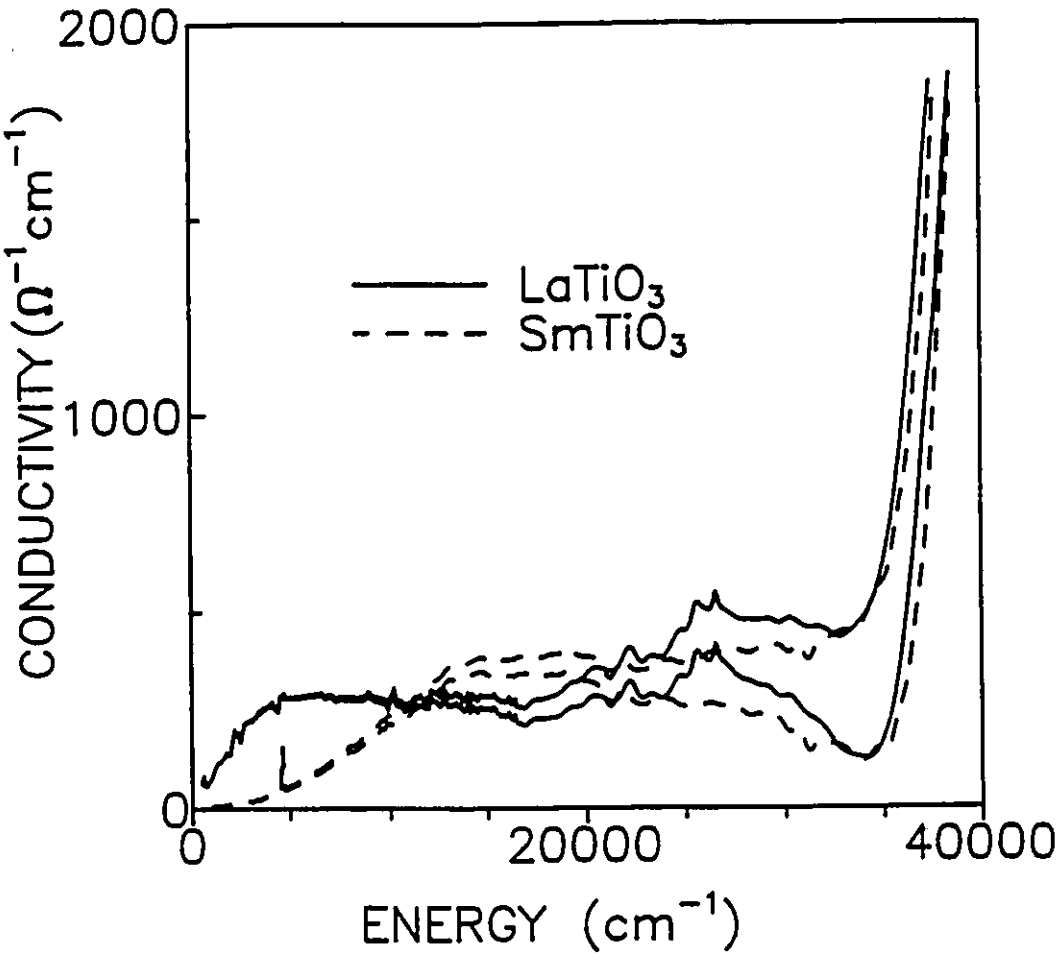

Figure 4.5: Optical conductivity for $LaTiO_3$ and $SmTiO_3$ at 300 K for different high frequency extrapolations. Extrapolation (a) of figure 4.3 produces the higher $\sigma(\omega)$ values for both compounds. For all curves in this figure it is assumed that $R \propto \omega^{-5}$ between 200000 and 10^6 cm^{-1}

It is interesting to calculate $N_{eff}(\omega)$ using the partial sumrule, equation 2.21. $N_{eff}(\omega)$ for $LaTiO_3$ and $SmTiO_3$ appears in figure 4.6. The figure indicates the spectral weight associated with the mid-infrared band is approximately 0.2 electrons per formula unit. The near equality of the spectral weight of the band in the two materials is an indication that the midinfrared band is an intrinsic feature of $RTiO_3$ perovskites. If it were impurity related one would expect $N_{eff}(35000cm^{-1})$ to vary widely from sample to sample and to be much less than 0.2 for nominally stoichiometric material. To obtain an impurity band of this much spectral weight would require grossly non-stoichiometric samples. However, neutron activation and thermogravimetric analyses of the $LaTiO_3$ sample - to be discussed in detail in chapter 5 - indicate stoichiometric composition. As intimated in section 3.3, calculations suggest the rare earth titanites are Mott-Hubbard insulators where $U \leq \Delta$. We associate the mid-infrared absorption, which is an intrinsic feature of the series with U. The mid-infrared absorption is due to excitations of electrons from the lower to the upper Hubbard subband, excitations which place two electrons on one site. We will see in the next section that the mechanism responsible for the blue shift of the onset of of the midinfrared absorption may be the increased buckling of the Ti-O network with decreasing rare earth ionic radius.

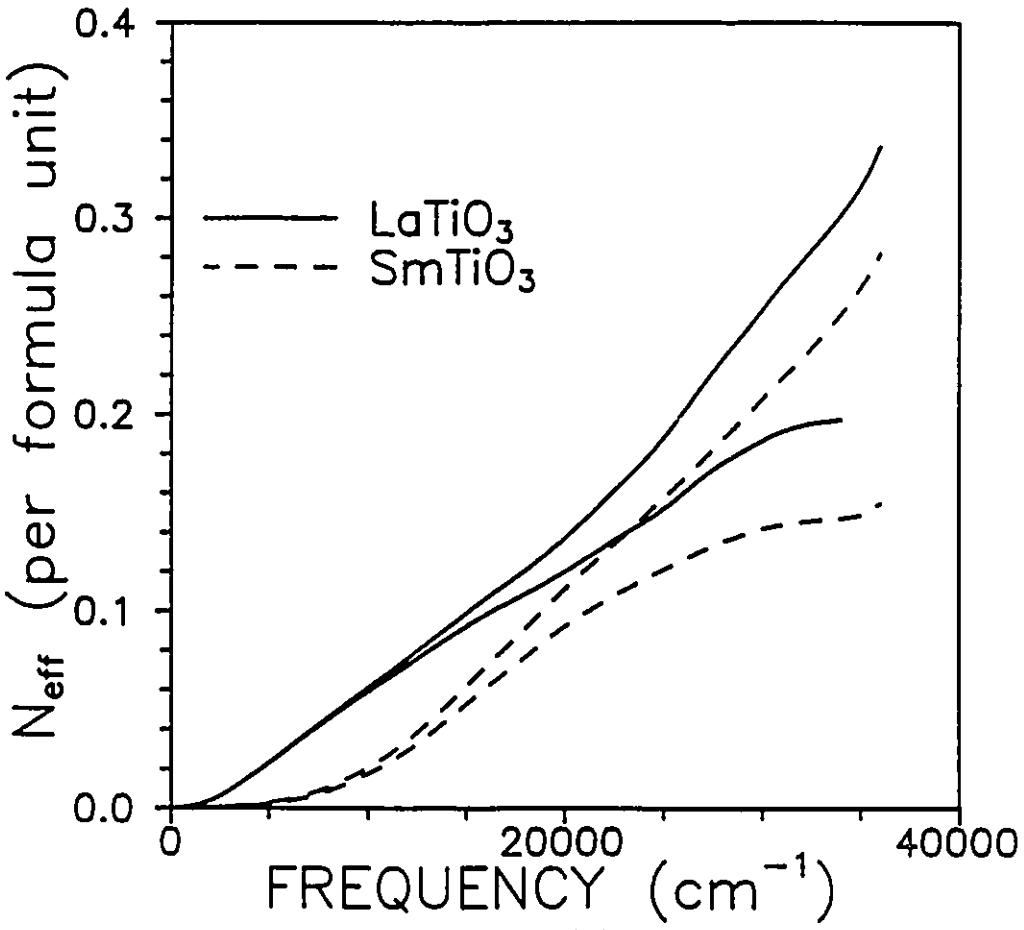

Figure 4.6: The effective number of carriers involved in optical transitions up to ω versus frequency for insulating $LaTiO_3$ and $SmTiO_3$ calculated assuming $m^* = 1$. The two curves presented for each sample result from substituting the $\sigma(\omega)$ curves of figure 4.5.

4.2.3 The Ti-O-Ti Bond Angle and Electronic Stru

The importance of the distortion of the Ti-O network is suggested by a comparison of doped $SrTiO_3$, $SrVO_3$ and $LaTiO_3$. Stoichiometric $SrTiO_3$, with a large band gap ($\approx$ 4 eV), must be reduced to achieve appreciable conductvity. Figure 4.7 is a plot of the room temperature resistivity of doped $SrTiO_3$ versus carrier concentration as measured by the Hall effect. Assuming $\rho = 1/ne\mu$, the data suggests constant mobility. Points for $SrVO_3$ [25] and $LaTiO_3$ [26] have been placed on the graph assuming that the electron concentration equals the density of V and Ti atoms respectively (one band model). The data for $SrVO_3$, which is a cubic perovskite like $SrTiO_3$ lie closer to the extrapolated line of doped $SrTiO_3$ than do the data for $LaTiO_3$ in which the TiO_6 octahedra undergo a set of co- operative twists to accomodate the difference in lattice constants desired by the LaO and TiO_2 layers. If the assumed carrier concentrations are correct the data indicate a significant decrease in mobility for the rare earth titanites.

To examine the effect of buckling the Ti-O network on the band structure near the Fermi surface we use linear combination of atomic orbitals (LCAO) with some guidance from Harrison [52]. The details of the technique are given in Appendix A. The important atomic orbitals close to the Fermi energy in early transition metal ABO_3 compounds are the B(3d), O(2p) and O(2s) states. The A ions serve only as electron donors. Generally, the conduction bands derived from A orbitals lie quite high above the Fermi energy and can be ignored. This may not be true for the rare earth titanites as Singh found non-zero La character near the Fermi level for 'cubic' $LaTiO_3$ [27]. The LCAO band structure of 'cubic' $LaTiO_3$ using the parameters listed in table 4.4 can be compared with Singh's calculation in figure 4.8. The agreement between the approximate and full calculation is not as good as for $SrTiO_3$.

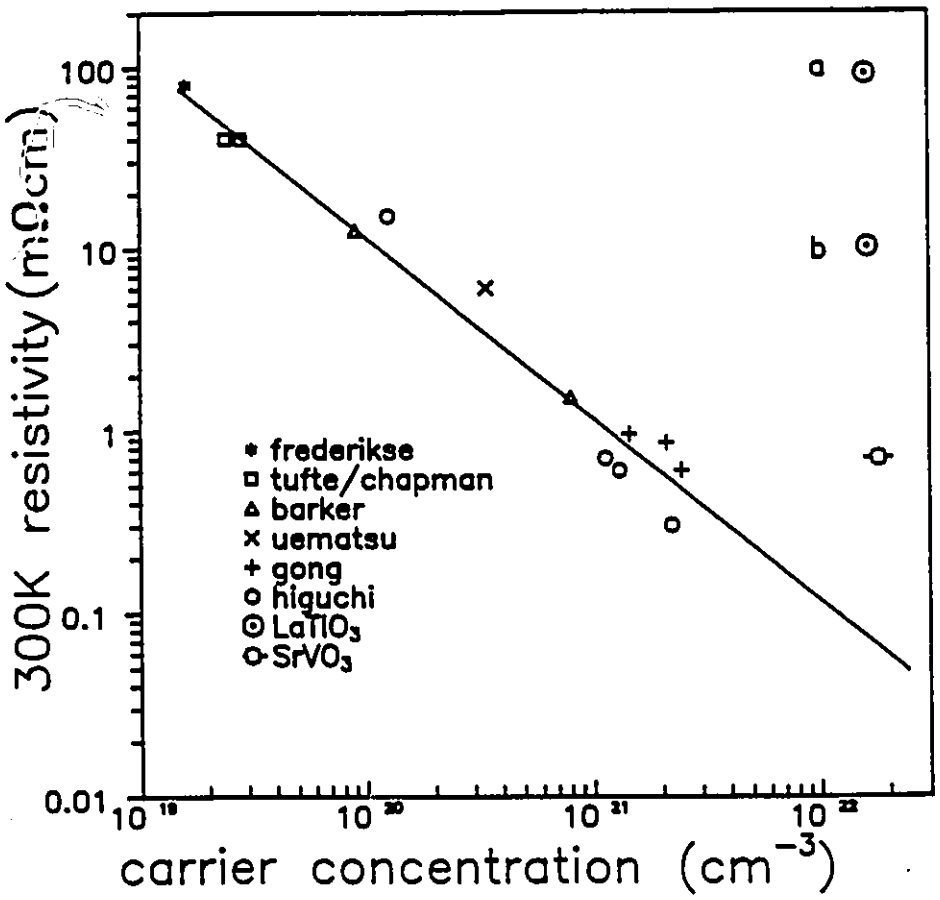

Figure 4.7: Room temperature resistivity versus carrier concentration ($1/R_he$) for doped $SrTiO_3$ measured by a variety of groups [47-51]. $LaTiO_3$ points *a* and *b* from references [14] and [26] respectively. Resistivity for $SrVO_3$ from reference [25].

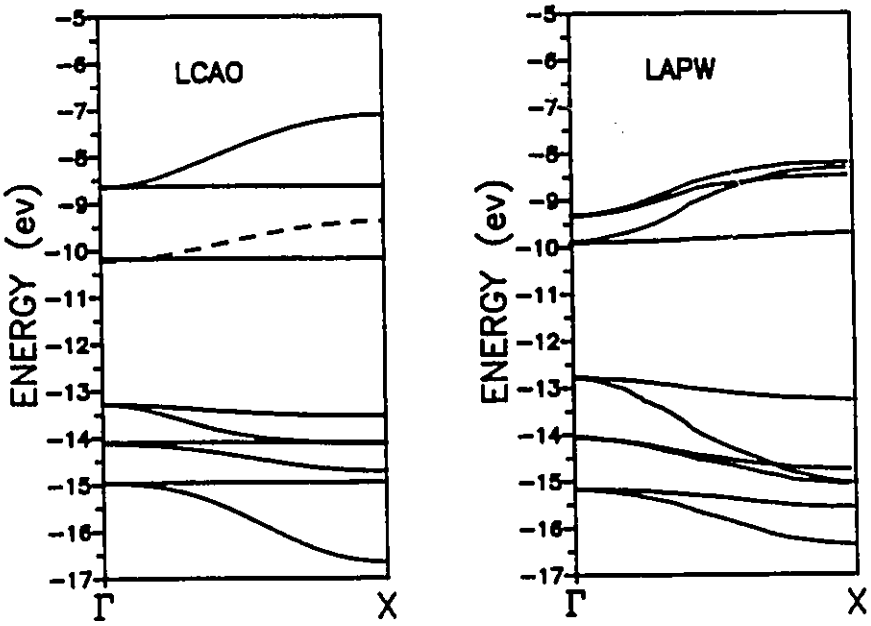

Figure 4.8: Comparison of LCAO bands with Singh's APW bands. The dashed line in the figure is the conduction band.

Table 4.4: Parameters required for LCAO band structure calculation of 'cubic' $LaTiO_3$. d(Ti-O) = 2.02 Å. The matrix elements were obtained using Harrison's method discussed in the appendix and are given in eV.

ϵ_s	ϵ_p	ϵ_d	$V_{sd\sigma}$	$V_{pd\sigma}$	$V_{pd\pi}$	E_{xx}
-29.14	-14.13	-10.22	-2.31	-2.15	0.993	0.148

As the calculation in the appendix shows, the conduction band in the $\Gamma - X$ direction ($\underline{k} = k_z = (001)$) belongs to the irreducible representation Δ_5 and is a $Ti(d\pi) - O(p\pi) - Ti(d\pi)$ pathway. We have to consider mixing d_{xz} with p_x or d_{yz} with p_y orbitals. To make the calculation for the distorted lattice simpler, second nearest neighbour O(2p)-O(2p) interactions are ignored. The calculated conduction band is not affected by this approximation (however the valence bands - of largely O(2p) character - are not correctly obtained). The only required matrix elements are those relevant for the nearest neighbour $p_x - d_{xz}$ interaction ($V_{pd\pi}$ and $V_{pd\sigma}$). We set $V_{pd\pi} = 1.52$ eV rather than the Harrison value listed in table 4.4 in order to obtain better agreement Singh's conduction band width (≈ 1.7 eV). Figure 4.9 illustrates the orbitals involved in the calculation in both the cubic and distorted geometries as well as the Bloch sum phases for the cubic case.

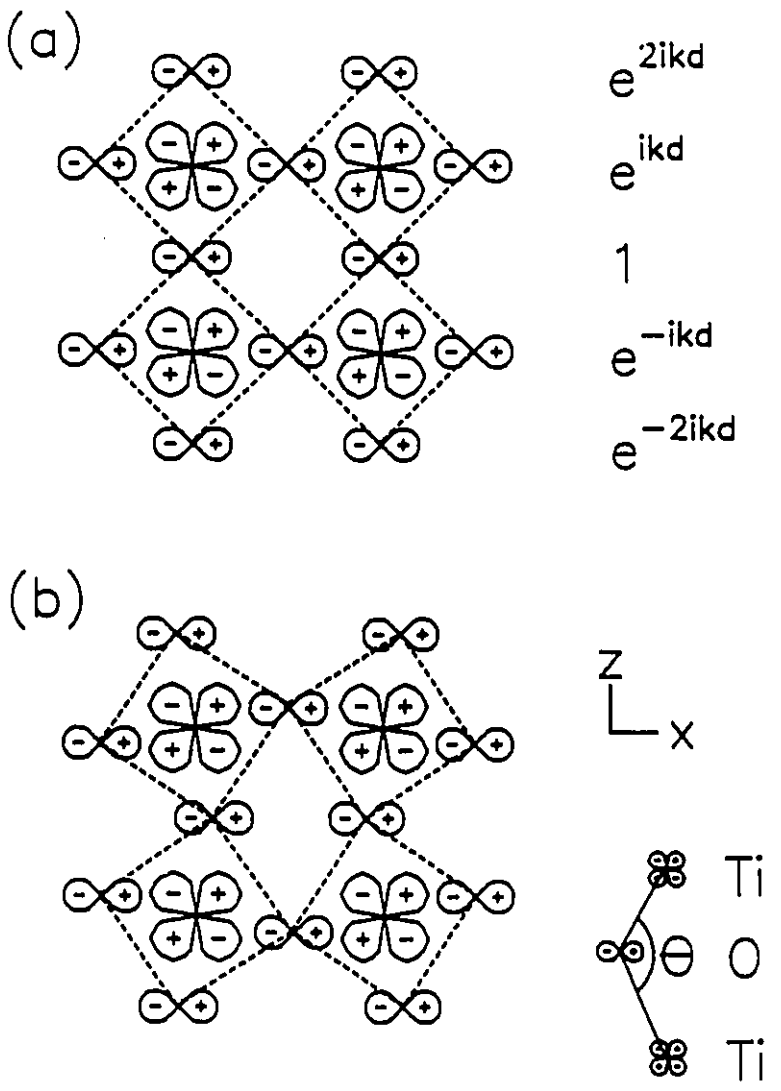

Figure 4.9: Orientation of the orbitals making up the conduction band in $LaTiO_3$ in the (a) cubic and (b) orthorhombically distorted structures.

The matrix which must be diagonalized is:

$$\begin{pmatrix} \epsilon_p & 0 & 0 & E^1_{x,xz}\exp -ik_z d_1 \\ 0 & \epsilon_p & 0 & 0 \\ 0 & 0 & \epsilon_p & -2iE^3_{x,xz}\sin k_z d_3 \\ E^1_{x,xz}\exp ik_z d_1 & 0 & 2iE^3_{x,xz}\sin k_z d_3 & \epsilon_d \end{pmatrix} \tag{4.3}$$

where

$$d_1 = d\cos\theta/2 \tag{4.4}$$

$$d_3 = d\sin\theta/2 \tag{4.5}$$

$$E^i_{x,xz} = \sqrt{3}l_i^2 n_i V_{pd\sigma} + n_i(1-2l_i^2)V_{pd\pi} \tag{4.6}$$

$$l_1 = n_2 = \cos\theta/2 \tag{4.7}$$

$$n_1 = l_3 = \sin\theta/2 \tag{4.8}$$

The result of the calculation can be seen in figure 4.10. A structural trend (the monotonic decrease in θ(Ti−O−Ti) across the rare earth titanite series) produces a systematic narrowing of the conduction band in the one electron approximation. In the titanites, where the Ti(3d) electrons are localized, the conduction bandwidth $W \leq U$, and the band splits into lower and upper Hubbard subbands. The midinfrared absorption is due to excitations from the lower to the upper Hubbard subband. The blue shift of the onset of the midinfrared absorption can be explained if U is constant for the series but the Hubbard subband width systematically decreases. These are reasonable assumptions since U is determined mainly by the ionization potentials of

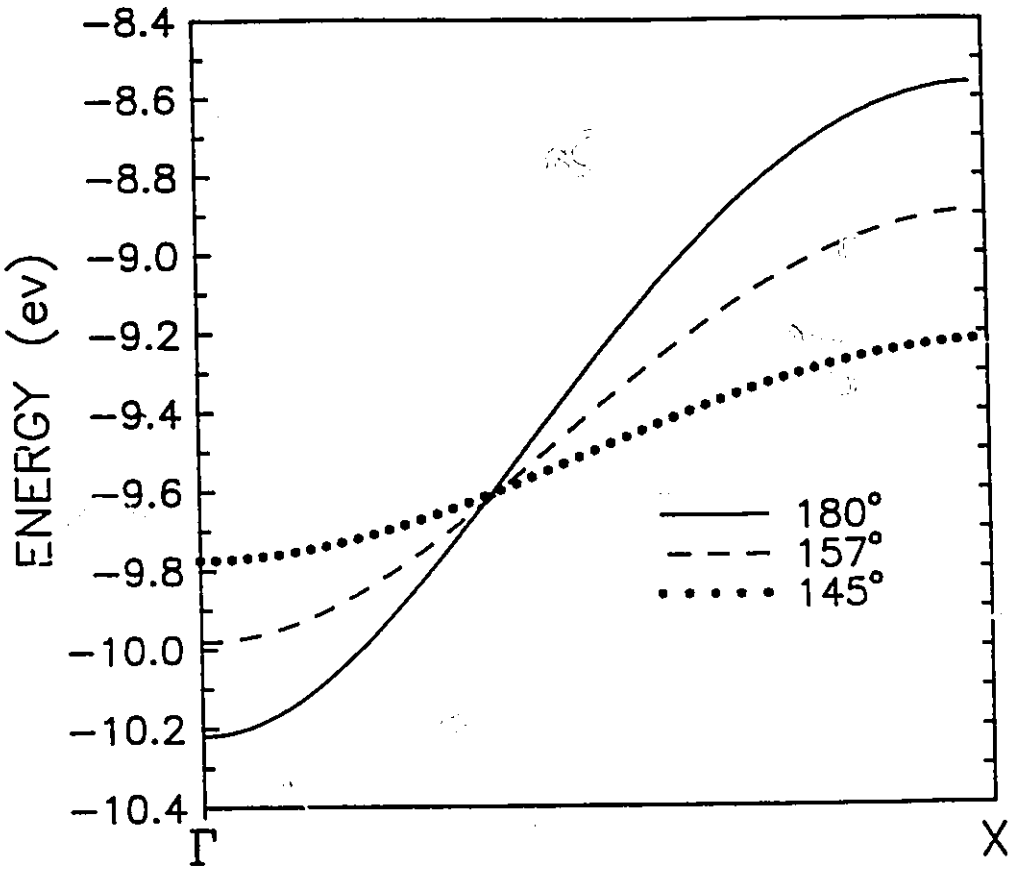

Figure 4.10: Dispersion of the conduction band in $RTiO_3$ perovskites in the $\Gamma - X$ direction as a function of buckling angle, $\theta(Ti - O - Ti)$

Ti and the Hubbard subband width should scale with the width of the conduction band in the one electron approximation. The band narrows by ≈ 0.6 eV as θ (Ti-O-Ti) decreases from 157° ($LaTiO_3$) to 145° ($GdTiO_3$) which is quite close to the observed shift of the onset of the midinfrared absorption - see figure 4.4.

From the beginning of this work, our wish has been to determine the electronic structure of $RTiO_3$ perovskites. Recall figure 3.3 which illustrates the possible types of electronic structure of transition metal oxides. We propose that the rare earth titanites are Mott-Hubbard insulators where $U < \Delta$. From the reflectance data, one can estimate values for the intrasite coulomb repulsion, U, the O(2p)-Ti(3d) charge transfer energy, Δ, and the valence band width, W. U and Δ can be estimated using figure 4.3. One can use equation 2.1 to model the dielectric function of the rare earth

titanites. The upturn in reflectance above 30000 cm^{-1} which is due to O(2p)-Ti(3d) charge transfer can be produced by adding a Lorentzian centred at approximately 5 eV to the dielectric function. Thus $\Delta \approx 5$ eV. Figure 4.3 shows that Δ is smaller in $SrTiO_3$ than in the $RTiO_3$ perovskites. This is expected since the Ti(3d) band is empty in $SrTiO_3$. The extra energy required for O(2p)-Ti(3d) charge transfer in $RTiO_3$ is U. A sum model fit of the reflectance of $SrTiO_3$ yields $\Delta \approx 4$ eV. Thus $U \approx$ 1 eV in $RTiO_3$ perovskites. Figure 4.10 indicates that W varies from approximately 1 eV in $LaTiO_3$ to 0.5 eV in $GdTiO_3$.

The optical properties are explained well using the Hubbard picture. However, a successful model of the electronic structure should be able to explain a wide variety of physical properties. For example, the free electron fermi gas model of simple metals can explain heat capacity, electrical conductivity, Pauli paramagnetism and optical reflectance [87].

Let us consider the electrical properties of $RTiO_3$ perovskites. As discussed in the introduction, previous measurements have shown a systematic increase in the dc conductivity activation energy, E_a, with increasing rare earth mass. E_a values extracted from resistivity versus temperature curves by various groups [11, 13] are listed in table 4.5 for comparison with the onset of the mid-infrared absorption. For convenience, the absorption onset was defined as the frequency at which an extrapolated linear fit to the band edge intersects the frequency axis. The E_a are systematically lower than the absorption onsets. This discrepancy deserves further study. It is hard to pin down the absorption onsets due to uncertainties in the Kramers-Kronig analysis and the presence of tails below the main edges in the frequency dependent conductivity curves of figure 4.4. Also, there is no theoretical prediction of the shape of the band edge. The E_a listed in table 4.5 were obtained at high temperatures. At high temperatures, where impurities are less important, the dc conductivity of Bloch-Wilson semiconductors is dominated by the free carrier density ($n,p \propto \exp E_g/2kT$)

[87] Thus, in semiconductors, the activation energies extracted from transport measurements are one half the band gaps obtained via optical measurements. Unlike a semiconductor, the density of states in a Mott-Hubbard insulator must be strongly-temperature dependent. States in the upper Hubbard band will be destroyed when the average thermal energy is big enough to create a substantial number of doubly occupied sites. There are a number of questions which should be considered. For example, are thermally created unoccupied sites similar to unoccupied sites created by doping which foster metallic dc conductivity? In summary, it is not obvious how to predict the temperature variation of the dc conductivity of a Mott-Hubbard insulator.

Let us turn to the magnetic properties of $RTiO_3$ perovskites. The Ti(3d) electrons are localized in $PrTiO_3$, $NdTiO_3$ and the heavier rare earth titanites and the Ti sublattice exhibits Curie-Weiss behaviour consistent with correlation induced localization. Insulating $LaTiO_3$ has the smallest gap between Hubbard subbands. Previous workers observed temperature independent Pauli paramagnetism in $LaTiO_3$ samples where the resistivity increases with temperature. However, Lichtenberg *et al.* maintain that metallic resistivity is found only in non-stoichiometric $LaTiO_3$. A close examination of the magnetic susceptibility, $\chi(T)$, data for a $LaTiO_3$ sample exhibiting insulating resistivity behaviour shows that $\chi(T)$ increases slightly with decreasing temperature above T_n [26]. This is a point which merits further attention.

In summary, the Hubbard model can qualitatively account for systematic changes in structural, electrical , magnetic and optical properties of the rare earth titanites. Before we turn to a study of the doped Mott- Hubbard insulator, $LaTiO_3$ let us examine the vibrational properties of the rare earth titanites.

Table 4.5: Activation energies (in eV) for the dc conductivity of insulating $RTiO_3$ compounds measured by Basuev *et al.* [11] on polycrystalline samples or Greedan *et al.* on single crystals [13]. The onset of the mid infrared absorption listed in this table is defined as where an extrapolated linear fit to the band edge intersects the frequency axis. The actual onset is probably lower due to band tailing effects.

R	Basuev	Greedan	MIR band onset
La	-	-	0.01
Ce	-	-	0.05
Pr	0	0.03	0.06
Nd	0.06	0.03	0.16
Sm	0.15	0.15	0.50
Gd	0.19	0.19	0.75

4.3 Far-Infrared Results: Vibrational Properties

4.3.1 Background

Consider the phonons in the cubic perovskite structure. Having five atoms per formula unit, a cubic perovskite has three acoustic phonon branches and twelve optical phonon branches. Group theory predicts five triply degenerate irreducible representations at the zone center (k = 0) [53]:

$$\Gamma^{\text{total}} = 4F_{1u} + F_{2u} \tag{4.9}$$

The acoustic phonons have F_{1u} symmetry and the F_{2u} mode is optically silent (i.e. neither infrared (IR) nor Raman active.) The three IR active modes - commonly called the stretching mode (B-O bond length modulation), the bending mode (B-O bond angle modulation) and the external mode (vibration of the BO_6 octahedron against the A atoms) - are illustrated in figure 4.11 [54].

Table 4.6 lists the frequencies of the three infrared active modes in several perovskites. Two factors influence phonon frequency, the interatomic potential and the mass of the atoms involved in the vibration. There are no simple rules for mode assignments. For example the lowest frequency mode in $KMgF_3$ is the external mode, while the lowest frequency mode in in ferroelectric $BaTiO_3$ and $SrTiO_3$ is the stretching mode. One should be aware that the perovskite structure is prone to ferrolectricity. The low frequency stretching mode - the soft mode - in ferrolectric $BaTiO_3$ and $KNbO_3$ and antiferrolectric $SrTiO_3$ is overdamped, producing high and relatively constant low frequency reflectance. The soft mode is also strongly temperature dependent [55, 56, 57, 58]. For example in $SrTiO_3$, the center frequency of the mode monotonically increases from approximately 10 to 100 cm^{-1} between 10 and 300 K.

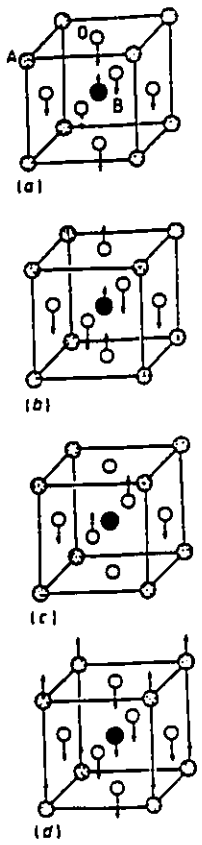

Figure 4.11: Zone center modes in the cubic perovskite lattice. (a) stretching (b) bending (c) inactive (d) external. From reference [54].

Table 4.6: phonon frequencies for various cubic perovskites

Compound	Temp (K)	Ext	Bend	Stretch
$SrTiO_3$	300	178	544	88 [58]
$KNbO_3$	710	198	521	65 [56]
$BaTiO_3$	400	180	485	60 [55]
$KMgF_3$	300	155	300	478 [59]

Non-cubic perovskites often exhibit only three main IR active bands, even though in principal the crystal distortion produces new modes. Couzi and Huong considered the $GdFeO_3$ structure exhibited by $RTiO_3$ perovskites and the effect of the orthorhombic distortion on the zone center modes of a cubic perovskite [53]. There are four formula units per unit cell in the orthorhombic structure implying 57 optical modes.

The group theoretical correspondence between the optical modes in the cubic structure and the orthorhombic structure is:

$$4F_{1u}^{ext} \rightarrow 2A_g + 2B_{1g} + B_{2g} + B_{3g} + A_u + B_{1u} + 2B_{2u} + 2B_{3u} \tag{4.10}$$

$$4F_{1u}^{stretch} \rightarrow 2A_g + 2B_{1g} + B_{2g} + B_{3g} + A_u + B_{1u} + 2B_{2u} + 2B_{3u} \tag{4.11}$$

$$4F_{1u}^{bend} + 4F_{2u}^{silent} \rightarrow 3A_g + 3B_{1g} + 3B_{2g} + 3B_{3g} + 3A_u + 3B_{1u} + 3B_{2u} + 3B_{3u} \tag{4.12}$$

New modes: $3A_u + 2B_{1u} + 2B_{2u} + 2B_{3u}$

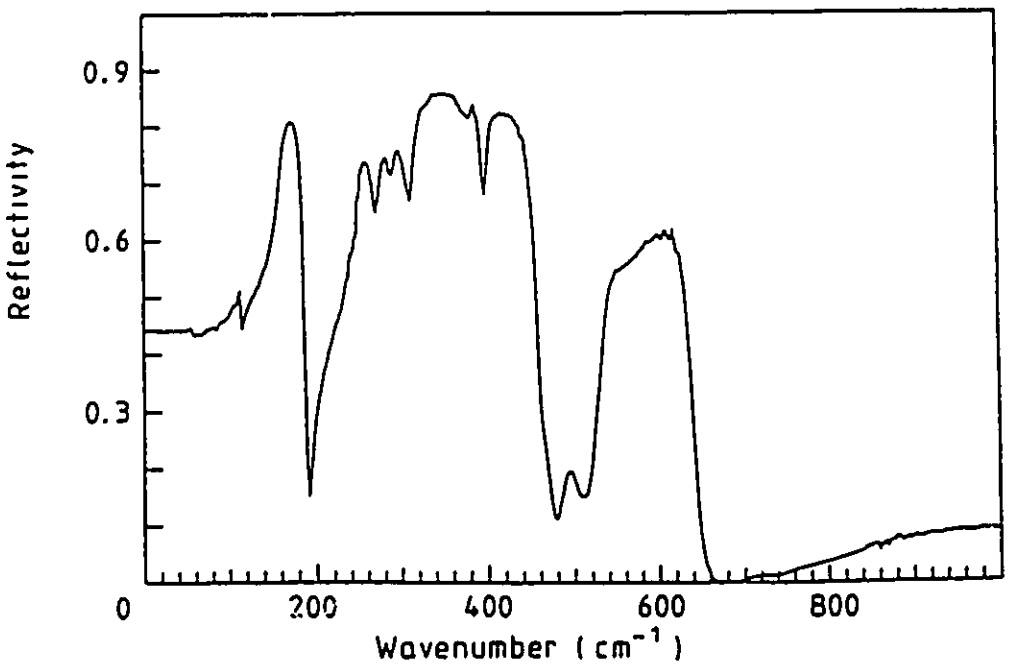

Figure 4.12: Room temperature reflectance of $LaFeO_3$. From reference [54].

Only the B_{1u}, B_{2u} and B_{3u} modes are optically active implying 25 modes in total. Therefore $RTiO_3$ perovskites should have should have 5 external modes, 5 stretching modes and 9 bending modes as well as 6 new modes. The reflectance of $LaFeO_3$ - which has the same orthorhombic crystal structure as the $RTiO_3$ series - is shown in figure 4.12. The spectrum retains the three band structure of a cubic perovskite spectrum. The orthorhombic distortion produces small splittings within the three main bands.

4.3.2 Far-Infrared Reflectance of the Rare Earth Titanites

The far-infrared reflectance of the insulating rare earth titanites appears in figure 4.13. The crystals were not oriented for the measurements which were performed with unpolarized light.

Three main groups of modes can be seen in all the spectra. Let us try to assign the bands to particular vibrational modes. Calculation of the optical conductivity shows that none of the modes in the spectra are overdamped and temperature dependent studies of $LaTiO_3$ and $GdTiO_3$ show that none of the modes are strongly temperature dependent. Thus, neither of the signals of a soft stretching mode appear in the far-infrared spectra. A comparison of the frequencies of the external mode of the perovskites listed in table 4.6 with the spectra of figure 4.13 suggests the lowest mode ($\approx$ 170 cm^{-1}) is probably the external mode. The two higher frequency bands are then the internal vibrations of the TiO_6 octahedron. Note that there are more modes clustered near 340 cm^{-1} than 550 cm^{-1}. Hence we tentatively assign the middle band to the bending mode. As discussed above, there should be nine bending type modes but only five stretching modes in the $GdFeO_3$ structure. The mode near 550 cm^{-1} splits into two modes for $SmTiO_3$ and $GdTiO_3$ while the modes near 340 cm^{-1} appear to fan out in $NdTiO_3$, $SmTiO_3$ and $GdTiO_3$. In $GdTiO_3$, the 340 cm^{-1} band splits into two groups of modes.

These changes can be correlated with a systematic tetragonal distortion of the TiO_6 as the rare earth becomes smaller. If one bond is signicantly longer than the other two, one would expect the force constants and vibrational frequencies of the bonds to be different. Table 4.7 lists the intraoctahedron Ti-O bond lengths of several rare earth titanites determined by David Maclean [43].

The far infrared reflectance spectra were modeled using equation 2.1. $SmTiO_3$ and $GdTiO_3$ were modeled using Lorentzians to represent the phonons and the high frequency dielectric constant ε_∞. As discussed in the previous section there is

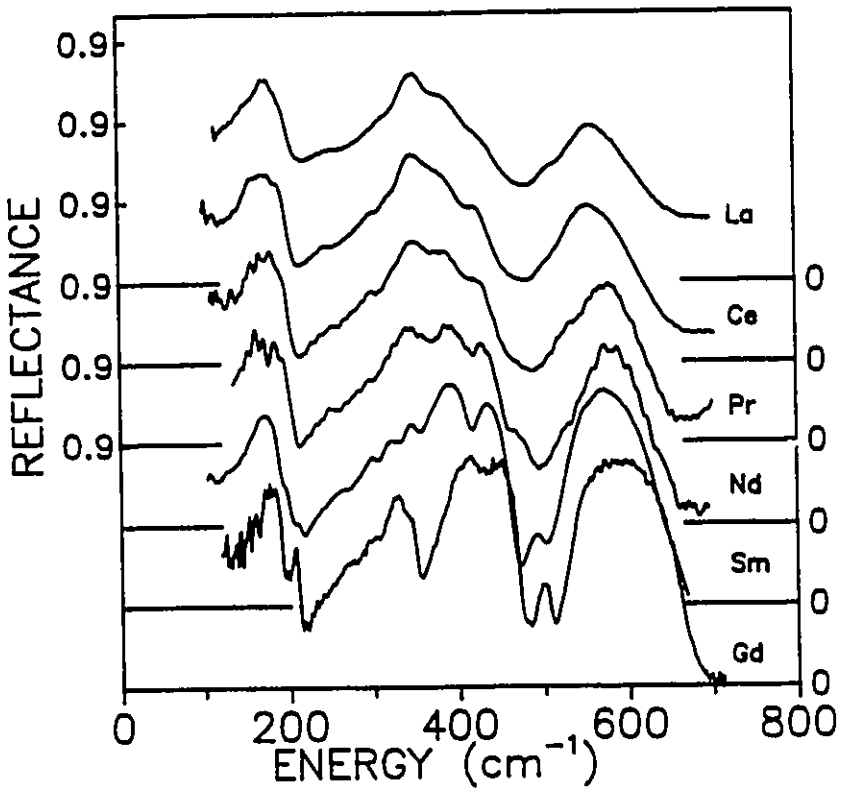

Figure 4.13: Room temperature far-infrared reflectance as a function of frequency for various $RTiO_3$ perovskites.

Table 4.7: Interatomic distances in Å within the TiO_6 octahedron for several rare earth titanites.

Bond	La	Nd	Sm	Gd
Ti-O1(1)	2.015(5)	2.010(1)	2.014(2)	2.014(1)
Ti-O2(6)	2.016(12)	2.020(3)	2.042(5)	2.027(3)
Ti-O2(7)	2.023(12)	2.035(3)	2.056(5)	2.076(3)

a mid-infrared process, modeled by an overdamped Lorentzian which must be added to the dielectric function when fitting $LaTiO_3$, $CeTiO_3$, $PrTiO_3$ and $NdTiO_3$. Finally, there is a small Drude component which is added for $LaTiO_3$. The phonon parameters are listed in table 4.8 while the electronic contributions to the model dielectric function are given in table 4.9. If the spectra are examined closely, there are some weak shoulders which are not included in the fits. For example, although only one phonon is used to model the reflectance peak near 340 cm^{-1} in $LaTiO_3$, one can perceive four shoulders. Unique fitting parameters for phonons with small oscillator strength could not be obtained; they depended strongly on the starting parameters for the fit. The large width of the higher frequency bands in $LaTiO_3$, $CeTiO_3$ and $PrTiO_3$ in table 4.8 is an indication that the band is composed of several modes which become split in $NdTiO_3$, $SmTiO_3$ and $GdTiO_3$.

Table 4.8: Phonon parameters determined in sum model fits to the far-infrared reflectance of the rare earth titanites. The parameters for each phonon are a column of three numbers (in cm^{-1}). The top, center and bottom numbers are the center frequency (ω_{oj}), width (Γ_j) and strength (ω_{pj}) of the phonon respectively.

	ext	bend				stretch	
La	170	340				545	
	20.3	55.9				51.6	
	595	1105				720	
Ce	172	339				533	
	25.4	62.8				58.1	
	596	1110				670	
Pr	173	338				543	
	23.0	62.5				50.8	
	560	1090				630	
Nd	171	333		373		550	
	28.2	37		82		43	
	570	850		650		600	
Sm	167	324	343	368	422	490	536
	24.3	42	17.1	23.6	13.6	14.3	24.2
	500	670	410	566	173	155	521
Gd	174 205	324		390	433	496	539
	12.8 8.6	24.3		19.4	10.4	16	20.4
	450 160	700		720	110	220	490

Table 4.9: Parameters of electronic contributions to the dielectric function of the insulating rare earth titanites. 'D' and 'M' refer to the Drude and midinfrared components respectively. ω_{oi}, Γ_i and ω_{pi} are the center frequency, width and strength of the Lorentzians representing the electronic modes.

	La	Ce	Pr	Nd	Sm	Gd
ϵ_∞	3.9	4.8	4.8	5.0	5.9	5.6
ω_{pD}	1120	-	-	-	-	-
Γ_D	540	-	-	-	-	-
ω_{oM}	6600	8900	9800	11300	-	-
Γ_M	22700	26000	29400	23000	-	-
ω_{pM}	19400	18600	18300	18300	-	-

Chapter 5

Doped $LaTiO_3$

High T_c superconductivity occurs when certain antiferromagnetic *charge transfer* insulators are doped. Understandably, there has been considerable interest in how the physical properties of highly correlated insulators evolve with doping. To date, all of the doping studies have been performed on charge transfer insulators like the cuprates. It is interesting to determine what sort of doping-induced changes will occur in the electronic structure of $LaTiO_3$ which is a Mott-Hubbard insulator.

5.1 Doping Mechanism

The electrical and magnetic properties of $LaTiO_3$ depend strongly on the oxidation state of Ti. One indication of this is the inconsistency in the early measurements of the temperature dependent resistivity of nominally stoichiometric $LaTiO_3$. Some workers measured a metallic resistivity at all temperatures [11, 12] while others [14] measured a change from insulating to metallic resistivity near 125 K. Lichtenberg *et al.* maintain that $LaTiO_3$, like the other rare earth titanites is actually a magnetic insulator and argue that the variation in electrical properties is due to excess oxygen.

Lichtenberg *et al.* studied a series of samples containing excess oxygen produced via reaction 5.1.

$$\frac{1}{2}La_2O_3 + (0.5 - x)TiO + (0.5 + x)TiO_2 \rightarrow LaTiO_{3+x} \qquad (5.1)$$

One of the puzzling features of the orthorhombic $LaTiO_{3+x}$ system ($0 \leq x \leq 0.2$) is the observation that the cell volume decreases from 249.70 to 242.85 $Å^3$ for $LaTiO_3$ and $LaTiO_{3.2}$ respectively. The excess oxygen would be interstitial since the perovskite structure contains no empty sites large enough to accomodate the large O^{2-} ion. It is hard to understand how the presence of large interstitial ions could produce a decrease in cell volume.

Some perovskites can tolerate a large number of vacancies on the A site. For example $Na_{1-x}WO_3$ is stable for $0.05 \leq x \leq 0.7$ [60] while ReO_3 is a perovskite where the A site is totally vacant. It is conceivable that $LaTiO_3$ is susceptible to La vacancies as there is a compound $La_{2/3}TiO_3$ [61] which may form a solid solution with $LaTiO_3$. Perhaps Lichtenberg *et al.* produced samples with La vacancies rather than excess oxygen. The effect of both doping mechanisms is the same, the Ti ion is oxidized. An excess oxygen atom produces 2 holes in the Ti(3d) band while a rare earth vacancy produces 3 holes. It is significant that Lichtenberg *et al.* did not measure the cation ratios of their samples and one might postulate that their TGA data could be explained by a cation vacancy mechanism. In the cation vacancy model ($La_{1-y}TiO_3$) one expects a weight gain of $\frac{(1-3y)15.999}{2FW}$ where the formula weight (FW) is 234.81-138.9y. In the oxygen excess model ($LaTiO_{3+x}$) one expects a weight gain of $\frac{(1-2x)15.999}{2FW}$ where the formula weight is 234.81. Table 5.1 gives the stoichiometry of the sample as a function of measured thermogravimetric weight gain as well as the oxidation state of titanium for the oxygen excess model and the cation vacancy model.

Table 5.1: Stoichiometry of the sample as a function of thermogravimetric weight gain (in %) as well as the oxidation state of titanium in the oxygen excess $LaTiO_x$ and cation vacancy La_yTiO_3 models.

	cation vacancy		oxygen excess	
weight gain	y	Ti oxidation state	x	Ti oxidation state
3.8	1.049	2.85	2.94	2.88
3.7	1.036	2.89	2.96	2.92
3.6	1.023	2.93	2.97	2.94
3.5	1.011	2.97	2.99	2.98
3.4	0.999	3.00	3.00	3.00
3.3	0.987	3.04	3.015	3.03
3.2	0.975	3.08	3.03	3.06
3.1	0.963	3.11	3.04	3.08
3.0	0.952	3.14	3.06	3.12
2.9	0.940	3.18	3.07	3.14
2.8	0.929	3.21	3.09	3.18
2.7	0.918	3.24	3.10	3.20
2.6	0.907	3.28	3.11	3.22
2.5	0.896	3.31	3.13	3.26
2.4	0.885	3.34	3.14	3.28
2.3	0.875	3.37	3.16	3.32
2.2	0.865	3.41	3.17	3.34
2.1	0.854	3.44	3.19	3.38
2.0	0.844	3.46	3.20	3.40
1.9	0.834	3.50	3.22	3.44
1.8	0.824	3.52	3.23	3.46
1.7	0.814	3.56	3.25	3.50

The phase diagram of the "$LaTiO_{3+x}$" system established by Lichtenberg *et al.* [26] appears in figure 5.1. Besides the decrease in cell volume discussed above, systematic trends in electrical and magnetic properties were observed with increasing Ti oxidation state for samples with orthorhombic structure: The Neél temperature decreases monotonically with x. Samples with $x \geq 0.1$ exhibit no long range magnetic order at low temperatures. Stoichiometric $LaTiO_3$ exhibits a semiconductor-like decrease of resistivity with temperature between 4 and 300K. Low oxygen doping ($0.03 \leq x \leq 0.09$) produces samples which exhibit minima in the temperature dependent resistivity near T_n, while samples with $x \geq 3.1$ exhibit metallic resistivity at all temperatures. The room temperature resistivity decreases monotonically from approximately 90 to 0.4 mΩcm for $LaTiO_{3.01}$ and $LaTiO_{3.15}$ respectively.

5.2 Sample Preparation and Characterization

The reflectance of four well characterized samples labelled A,B,C and D was measured. Samples A, B and C were not intentionally doped. They were prepared by Dr. J.E. Greedan's previous graduate students using the technique described in David Maclean's thesis [43]. Surprisingly, these samples exhibit strikingly different physical properties. Sample D was intentionally doped with excess oxygen using the reaction:

$$La_2O_3 + (1 - 2x)Ti_2O_3 + 4xTiO_2 \rightarrow 2LaTiO_{3+x} \qquad (5.2)$$

The target stoichiometry was $LaTiO_{3.10}$ while chemical analysis which will be discussed presently suggests the product stoichiometry is $La_{0.88}TiO_3$. After the reactants were mixed and pressed into a pellet, a crystal was prepared in the same manner as the $NdTiO_3$ and $CeTiO_3$ samples discussed in section 4.1. In the triarc furnace, the crystal was pulled at a rate of 25 mm/h. The water cooled seed rod and hearth were rotated at 60 rpm and 120 rpm respectively in opposite directions. There

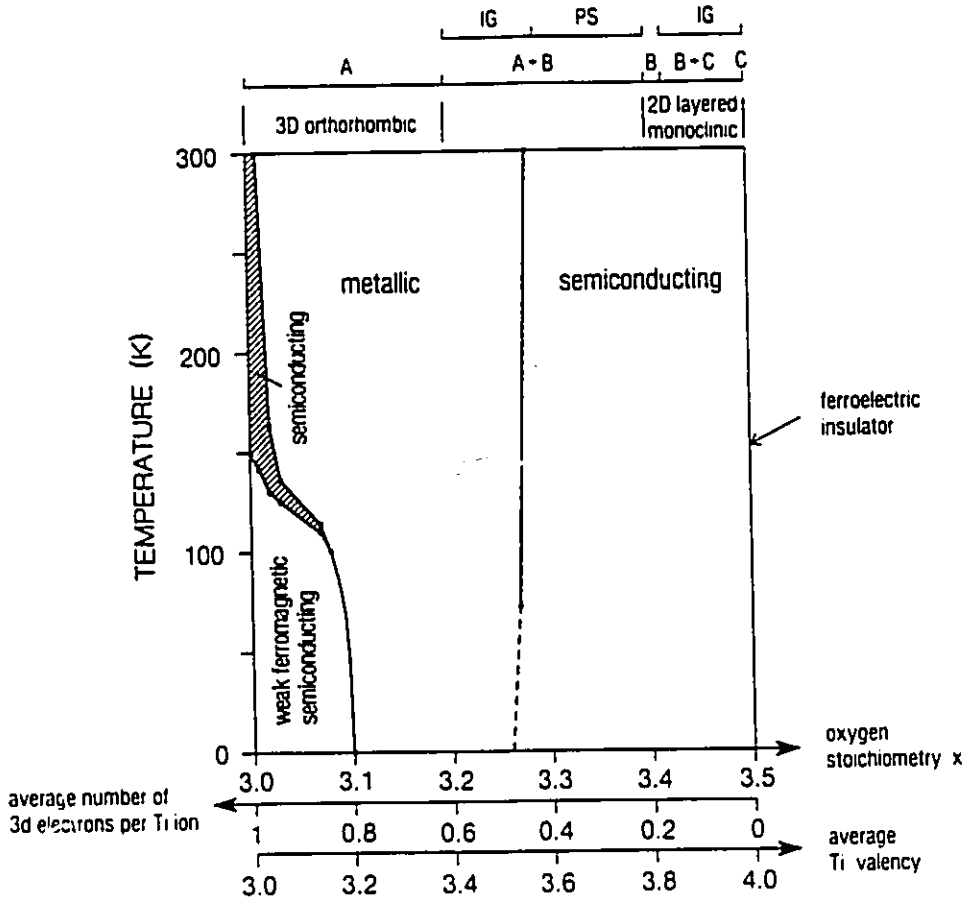

Figure 5.1: Phase Diagram of $LaTiO_{3+x}$ as determined by Lichtenberg *et al.* . Reference [26]

are some indications that sample D is not homogeneous as will be discussed below.

Sample purity and lattice constants were determined using a Guinier camera. The cation ratios were checked using neutron activation analysis and relative oxygen contents determined by measuring the weight gain upon heating to 1000°C in air. There was not very much A and C type material. Consequently the thermogravimetric analysis (TGA) was performed on roughly 100 mg of material. As the expected weight gain for stoichiometric $LaTiO_3$ is only 3.4 %, the uncertainty in these runs ($\approx$ 0.5 mg) leads to large relative uncertainties. TGA was done on larger pieces of samples B and D producing lower relative uncertainty. A summary of the chemical and structural analyses appears in table 5.2. Although the uncertainty is large, the neutron activation results support the $LaTiO_3$ vacancy doping mechanism. Sample D is grossly non-stoichiometric and the measured weight gain places it close the phase diagram boundary (figure 5.1) separating the orthorhombic phase from an intergrowth phase. No impurity phases were detected in the guinier photograph but chemical analysis as well as magnetic measurements to be discussed below shows the boule from which sample D was cut is inhomogeneous. The entries for sample D in table 5.2 are for a piece of the boule adjacent to sample D.

Fig. 5.2 shows the temperature dependence of the resistivity for the four samples. The measurements were made with silver paint contacts in the Van Der Pauw configuration. Sample A, which has the lowest oxygen content, exhibits an insulator-like negative temperature coefficient of resistivity for all temperatures between 4 and 300 K. Sample B exhibits a change from insulating to metallic behaviour near 175 K while samples C and D, are metallic over the whole temperature range studied.

Table 5.2: Chemical Analysis of samples A, B, C and D. The La:Ti ratio was determined by neutron activation analysis. The TGA weight gains were determined while heating to 1000°C in air. The Ti oxidation states come from the TGA data assuming the cation vacancy model - see table 5.1. Lattice parameters, given in Å, were measured using a guinier camera.

Sample	La:Ti (± 0.045)	% weight gain	Ti oxidation state	-
A	0.97	3.4 ± 0.5	3.0 ± 0.15	
B	0.96	3.18 ± 0.15	3.06 ± 0.03	
C	0.93	2.7 ± 0.5	3.24 ± 0.15	
D	0.88	2.3 ± 0.1	3.37 ± 0.03	
		Lattice parameters		
Sample	a	b	c	cell volume (Å^3)
A	5.6058(7)	5.6225 (7)	7.914(1)	249.93(3)
B	5.6035(7)	5.6204(6)	7.911(1)	249.14(3)
C	5.5949(10)	5.6035(8)	7.902(2)	247.76(7)
D	5.553(2)	5.593(2)	7.878(2)	244.69(6)

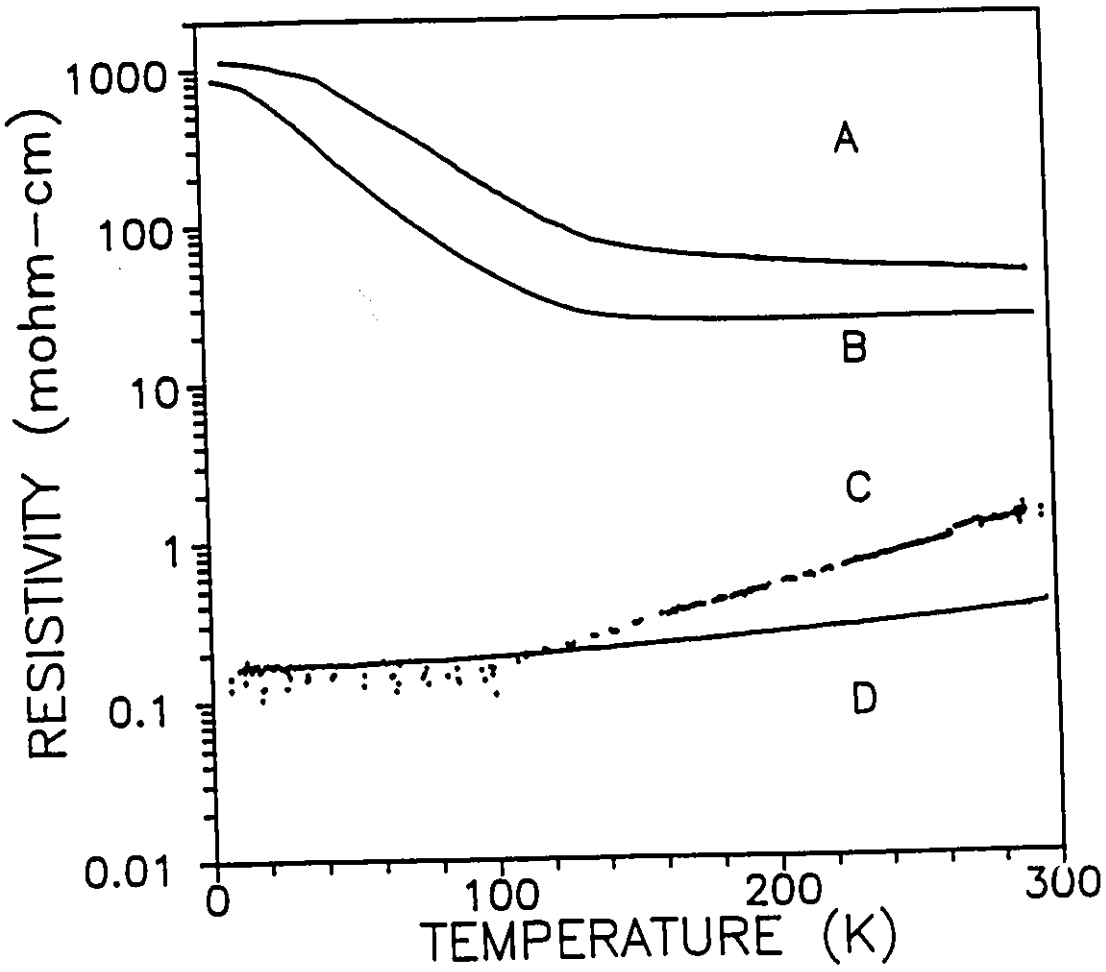

Figure 5.2: Resistivity of the four $LaTiO_3$ samples used in the reflectance measurements

Measurements of magnetization as a function of temperature are shown in Fig. 5.3. $LaTiO_3$ exhibits antiferromagnetic ordering [62] so the small moments are due to canting of adjacent spins. Sample C exhibits both metallic resistivity and magnetic ordering. Figure 5.3(b) shows the region of temperature independent paramagnetism. Data for two different pieces of sample D are presented. One of them exhibits a moment while the other does not. The guinier photograph did not show multiple phases but the magnetic data shows that grossly non-stoichiometric sample D is inhomogeous.

The decrease in cell volume, resistivity and Neél temperatures with increasing Ti oxidation state are consistent with the results of Lichtenberg *et al.* [26]. However the neutron activation results support the cation vacancy rather than the excess oxygen model. Careful diffraction studies should confirm the cation vacancy model.

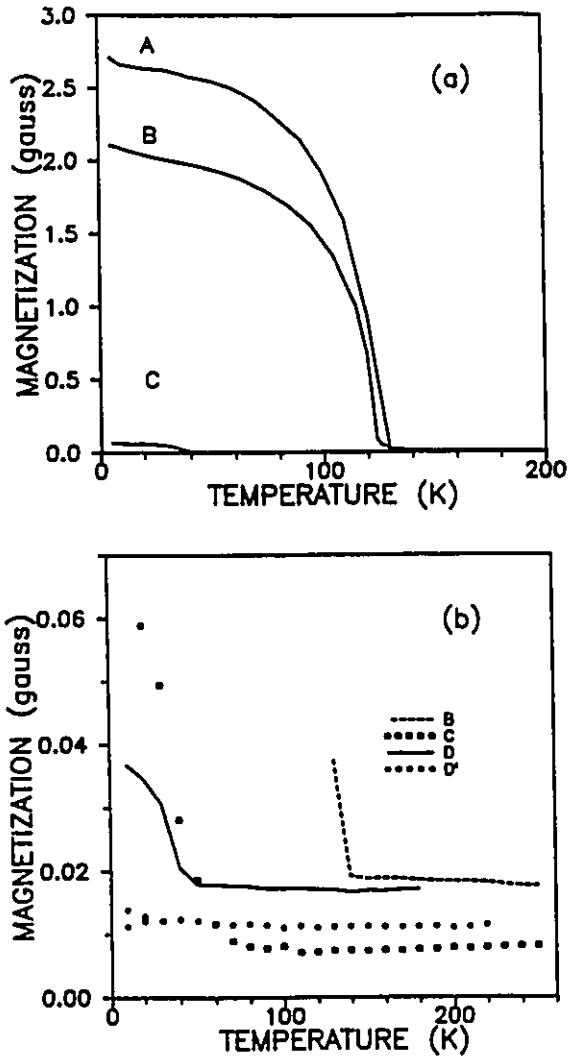

Figure 5.3: (a)Magnetization as a function of temperature for samples A, B and C. These samples were cooled in zero field. The moment was established by ramping the field to 15 kG. The field was then reduced to zero and the sample warmed in zero field. (b) Magnetization as a function of temperature for samples B, C and D and D'. Sample D' is cut from a different region of the boule than sample D. The different result indicates inhomogeneous stoichiometry. These samples were cooled below T_n, the moment established by ramping up to 10 kG. The field was reduced to 1 kG and the moment measured as the temperature was raised.

5.3 Previous optical studies of doped oxides

Before analyzing the reflectance of doped $LaTiO_3$, it is of interest to review the influence of doping on the optical properties of different types of parent compounds. Obviously, the nature of the parent compound must be considered in interpreting the effects of doping. Both Bloch-Wilson insulators (Si, $SrTiO_3$, TiO_2) and charge transfer insulators (e.g. the planar cuprates and La_2NiO_4) will be considered.

5.3.1 Impurities: Doped semiconductors

High levels of doping can render a filled-band-insulator metallic [63]. For example Si:P samples doped more heavily than the critical doping density ($n_c \approx 3.7 \times 10^{18} cm^{-3}$) exhibit metallic behaviour. The frequency dependent absorption coefficient, which is proportional to the real optical conductivity, appears in figure 5.4 for two different systems at various doping levels. The absorption spectrum for low doping levels is characterized by a series of atomic- like lines which are excitations to the various excited states of the donor. Higher doping levels cause the formation of impurity bands due to the overlap of nearby electron wavefunctions. Note that the absorption band widens and the edge moves towards zero frequency as the metallic regime is approached in the Si:P system [64]. Note also the development of a Drude type absorption centered at zero frequency for doping levels above n_c for the Ge:As system [65]. It has been argued that the broadening of the impurity absorption band in Si:P shown in figure 5.4 is due to the growth in intensity of absorption from random clusters of various sizes [64]. In a different doped system (Ge:Sb) Narita and Kobayashi [66] have interpreted the rise in far-infrared absorption above 2.2 meV ($\approx$ 18 cm^{-1}) as due to excitations from the lower to the upper Hubbard subband. In this model, as the impurity density increases, the subband width increases and the onset of absorption tends towards zero frequency.

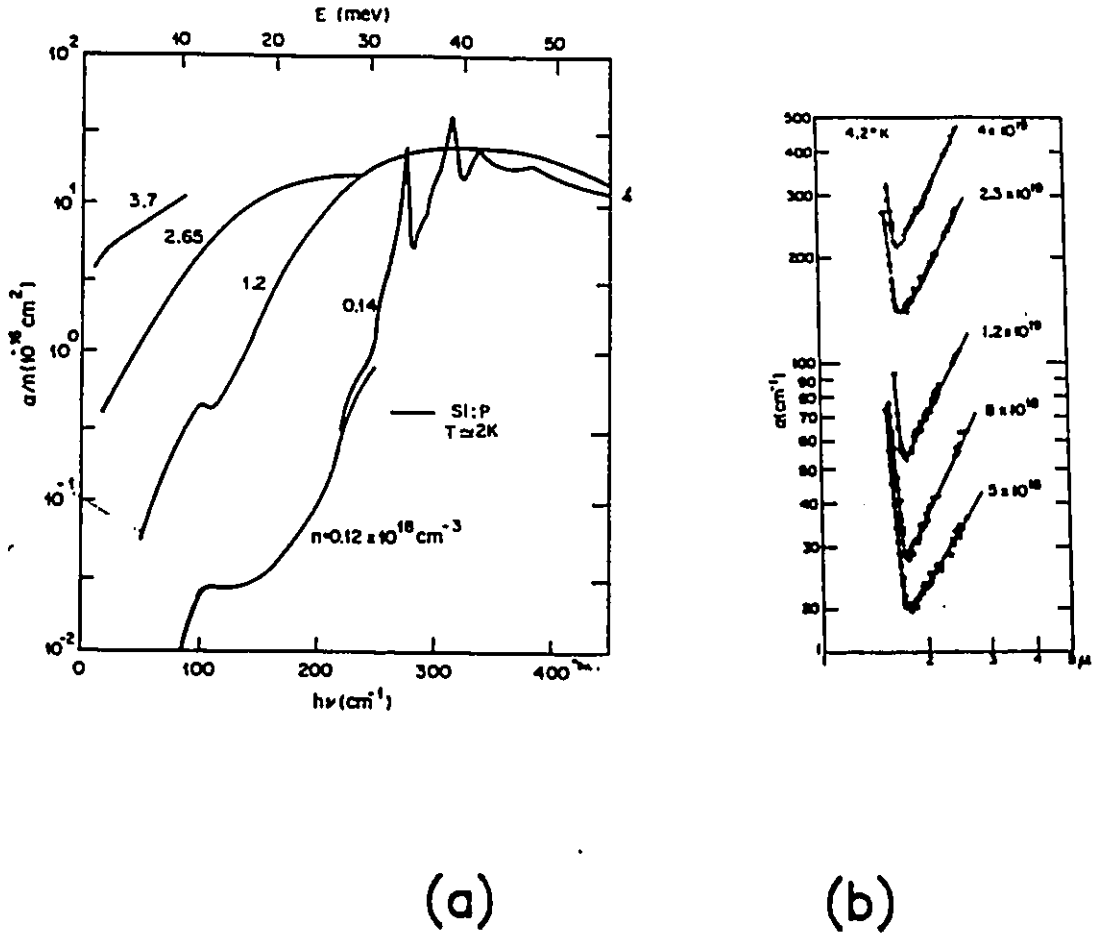

Figure 5.4: (a)Absorption coefficients for heavily doped Si:P samples at 2K. The most heavily doped sample is just on the insulating side. Reference [64].(b) Absorption coefficient of Ge:As in the metallic regime at 4K. Reference [65].

Consider now the relationship between the optical and transport properties of heavily doped semiconductors. The dc conductivity of a heavily doped semiconductor occurs via different processes depending on doping level and temperature [63]. In one process, which occurs at low doping levels and high temperature, electrons are thermally excited from the donors to the conduction band of the crystal (activation energy E_1). In another process, which occurs at higher doping levels, electrons travel in an impurity band where activation energy E_2 is required to excite electrons to the mobility edge of the impurity band. E_2 is governed by the combined effects of Anderson (disorder) and Hubbard (correlation) induced localization. The activation energy E_2 is about the same as the peak of the impurity absorption band [67].

5.3.2 Polarons: Non-magnetic titanates

TiO_2 and $SrTiO_3$ are both materials containing Ti^{4+} (empty d bands) which must be doped to attain appreciable dc conductivity. There is some evidence that a midinfrared absorption in doped TiO_2 is due to absorption by small polarons [68, 69].

Polarons are elementary excitations consisting of an electron accompanied by a lattice distortion. The coulomb field of a conduction band electron tends to pull positive ions closer and repel negative ions. If the electron is induced to move by an external field it will drag the lattice distortion along with it. There are two types of polarons: large polarons which are essentially itinerant electrons with an enhanced mass due to the strong electron-phonon interaction and small polarons where the lattice distortion produces a potential well at a particular atomic site which localizes the electron. Small polarons must hop from site to site. Experimental signs of small polaron behaviour are a thermally activated mobility and an optical absorption band centered at non-zero frequency . At first glance, the transport and optical properties of insulating $RTiO_3$ perovskites suggest the small polaron model.

The DC conductivity in the small polaron model is given by the equation 5.3 where Z is the number of nearest neighbours, n is the density of polarons, a is the nearest neighbour spacing, J is the band width and E_a is the thermal activation energy for the mobility [68]:

$$\sigma_{dc} = \sqrt{\frac{\pi}{36}} Z n a^2 J^2 \frac{e^2}{\hbar} \frac{(kT)^{-3/2}}{\sqrt{E_a}} \exp -\frac{E_a}{kT} \tag{5.3}$$

The real part of the optical conductivity in the small polaron model, where ω_o is the 'effective' optical phonon frequency and E_a is again the activation energy for the mobility, is given by [68, 71]:

$$\sigma(\omega) = \sigma_{dc} \frac{2kT}{\omega} [1 + (\frac{\hbar^2 \omega \omega_o}{8 E_a kT})^2]^{-1/4} \sinh \frac{\omega}{2kT} \exp -\frac{\omega^2}{16 E_a kT} \tag{5.4}$$

Besides requiring consistency between optical and transport properties, the small polaron model predicts that the strength of the mid-infrared absorption should scale with the number of carriers doped into the conduction band and that the absorption band is temperature dependent as shown in figure 5.5. Note that where $kT \gg E_a$, the center of the small polaron absorption moves to zero frequency which makes sense because the electrons are not bound to a particular site very effectively at these temperatures.

The small polaron model as originally constructed [69, 68] applies to materials where a relatively low density of carriers is doped into the conduction band and electron-electron (e-e) interactions can be ignored. Suzuki *et al.* [70] have studied the more complicated problem of polaron conductivity as a function of electron density in the narrow-band Hubbard model. The absorption spectrum in this model is given as a function of electron density in figure 5.6 which is taken from reference [70]. $\sigma(\omega)$ exhibits two peaks, one at an energy of $\hbar\omega_1 \approx S\hbar\omega_o$ where ω_o is an optical phonon frequency and S is related to the electron-phonon coupling strength. This low energy peak is described by equation 5.4.

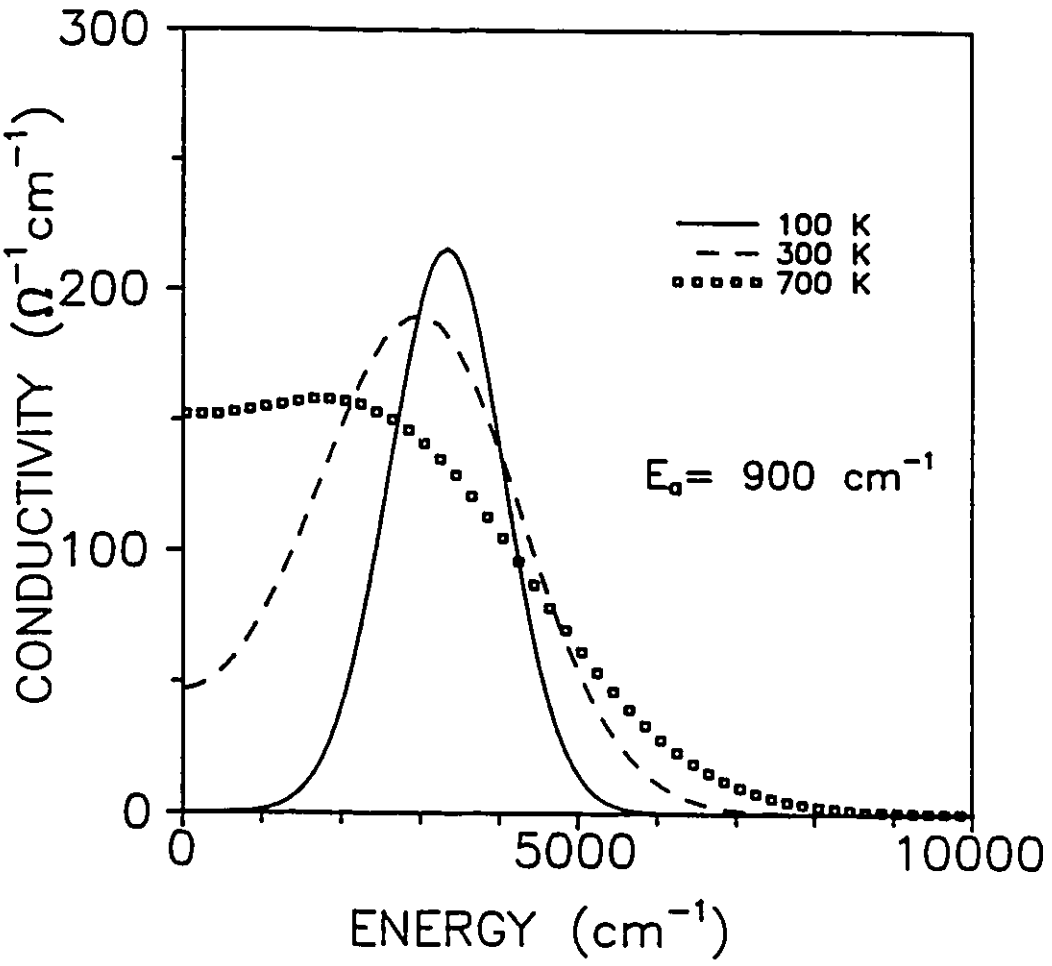

Figure 5.5: Temperature dependence of the absorption band in the small polaron model.

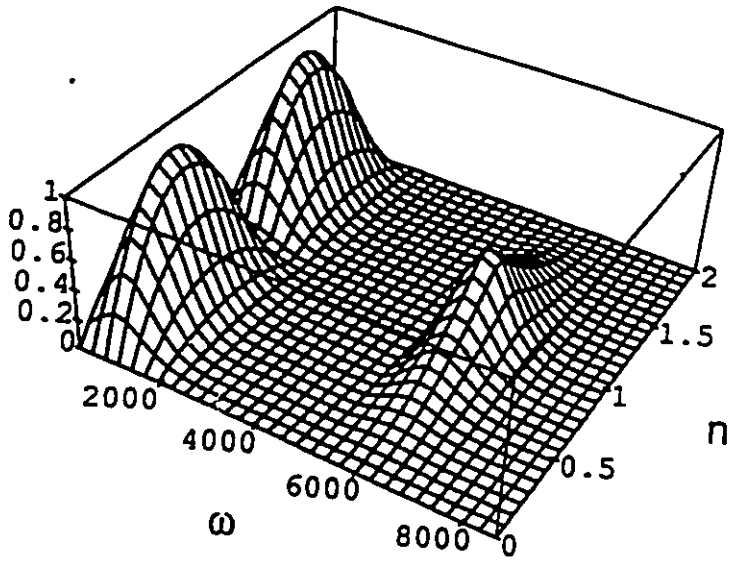

Figure 5.6: The polaron conductivity, in arbitrary units, is plotted versus frequency ω (cm^{-1}) and electron density. $n = 1$ corresponds to a half-filled band. From reference [70].

The higher energy peak occurs at $\hbar\omega_2 \approx S\hbar\omega_o + U$, where U is the effective Hubbard gap. As a function of electron density, the lower energy peak has maxima at $n = \frac{1}{2}$ and $n = \frac{3}{2}$. At $n = 1$ there is no conductivity until the photon energy exceeds the Hubbard gap, the lower peak disappears and only the upper peak survives.

One can show that the midinfrared band in $RTiO_3$ perovskites is not the lower energy peak in figure 5.6 by trying to apply equations 5.3 and 5.4 to $LaTiO_3$. In figure 5.7(a) we see that substituting $E_a = 182$ cm^{-1} into equation 5.3 fits the transport data of sample B reasonably well but the same E_a substituted into equation 5.4 gives a poor fit to the optical conductivity (figure 5.7(b)). If we use $E_a = 900$ cm^{-1} we obtain a better fit to the optical conductivity but a poor fit to the resistivity

data. In the previous chapter it was argued that the mid-infrared absorption band in $RTiO_3$ perovskites may be due to excitations across the Hubbard gap. In this model, the $RTiO_3$ midinfrared absorption band corresponds to the higher energy peak in figure 5.6 and is thus not the same as the absorption band in TiO_2 which is due to photon assisted hopping of small polarons.

Reik has argued [71] that the mid-infrared band in n-type $SrTiO_3$ shown in figure 5.8 is due to small polaron absorption. Since the mid-infrared band in $SrTiO_3$ scales with the dc conductivity it can argued that the band is related to the current carriers. However, Lee *et al.* note that an excitation from one conduction band to another (Γ_{15} - Γ_{12}) would also scale with doping[24]. The origin of the mid- infrared band in n-type $SrTiO_3$ and its relationship to the mid- infrared band of the $RTiO_3$ series deserves further study.

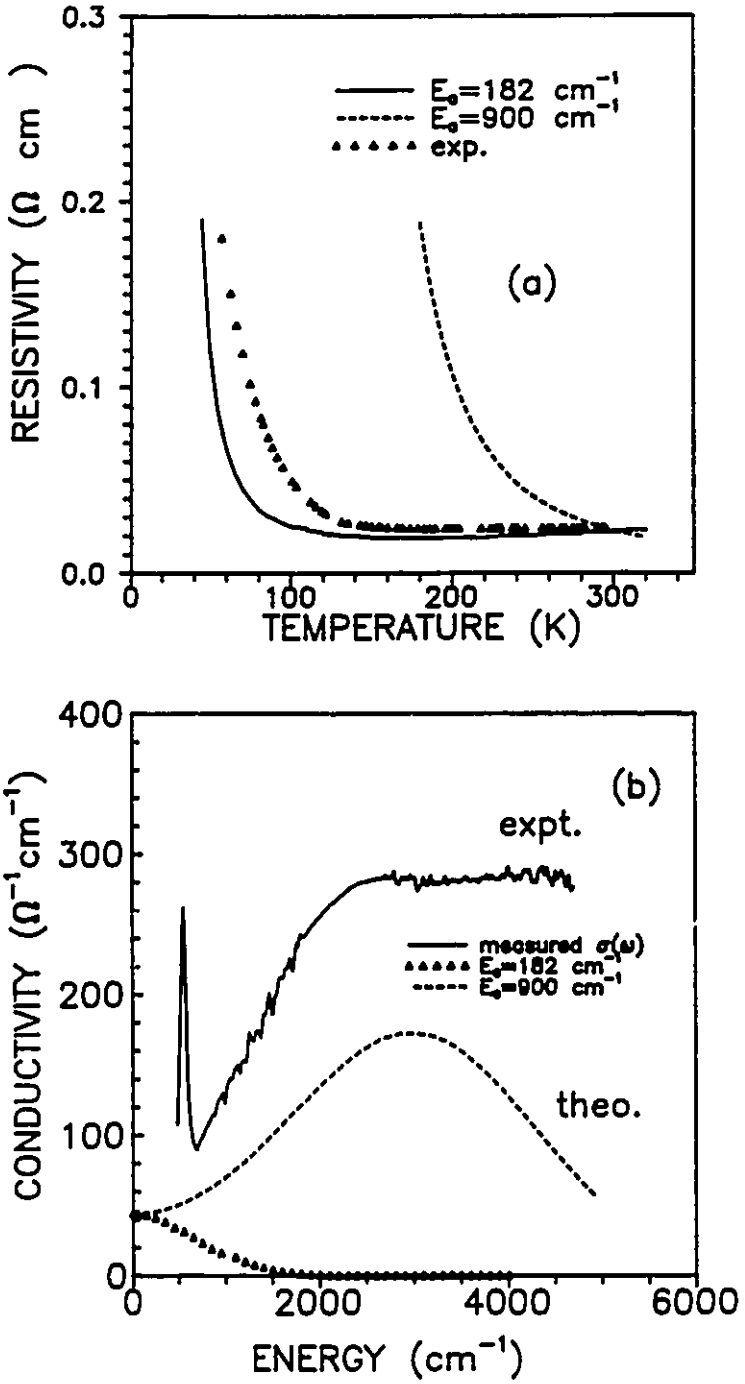

Figure 5.7: (a) dc resistivity of sample B versus temperature along with the small polaron theory prediction for activation energies of 182 and 900 cm^{-1} . (b) 300 K frequency dependent optical conductivity of sample B along with theoretical curves for E_a = 182 cm^{-1} and E_a = 900 cm^{-1}

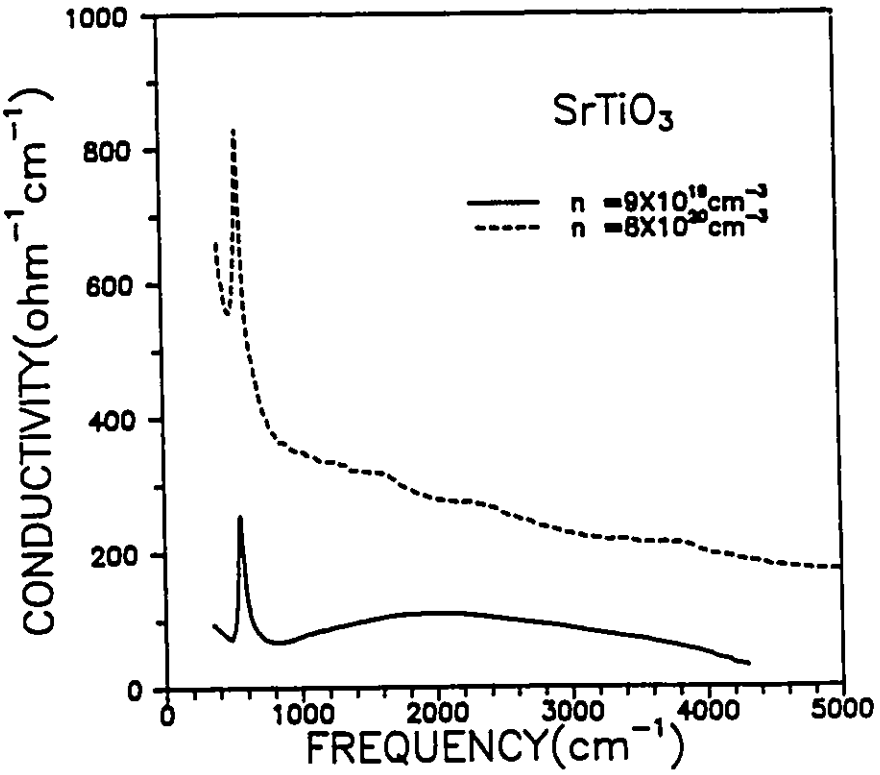

Figure 5.8: Optical conductivity of n-type $SrTiO_3$ determined by A. S. Barker, Jr. Figure created using data from reference [49]

5.3.3 Doped Charge Transfer Insulators

As discussed in section 3.4, the planar cuprates are antiferromagnetic charge transfer insulators meaning that the smallest gap in the excitation spectrum is the energy required to transfer an electron from O(2p) orbitals to Cu(3d) type orbitals rather than the Hubbard Cu(3d)-Cu(3d) splitting. In the stoichiometric parent compounds there is no absorption below the charge transfer gap The best published example of this is the work of Thomas *et al.* on high quality crystals of Nd_2CuO_4 [67] shown in figure 5.9 where one can see no absorption below the fundamental charge transfer gap in undoped material while in the oxygen deficient material there is a midinfrared absorption. Furthermore, M. Reedyk has observed roughly 50 percent transmission below the charge transfer gap in approximately 0.1 mm thick samples of the most insulating members (R= La,Ce) of the $Pb_2Ca_2RCu_3O_8$ series (R=rare earth) [72]. Although not intentionally doped, this series exhibits an insulator-metal transition as smaller rare earths are placed into the *R* site. It is believed that a small rare earth ionic radius promotes the formation of rare earth vacancies which introduce holes into the CuO_2 planes [73].

The effect of doping on the optical conductivity spectrum of the planar cuprates has been studied by a number of authors [34, 35, 36, 74]. Doping causes a mid-infrared absorption band to develop which is composed of at least two components, as can be seen in figure 5.9. Thomas *et al.* note that the center frequency (E_J of the lower frequency component of the mid-infrared band in a number of planar cuprates is close to the antiferromagnetic exchange energy ($J \approx 0.1$ eV) measured in the two magnon Raman scattering spectrum (there is a peak in the Raman spectrum at approximately 4J which is due to the creation of two zone boundary magnons of equal and opposite momentum). At low levels of doping, movement of a hole to a different copper site in the CuO_2 plane would require energy of order *J* since it would place parallel spins side-by-side. They also observe that the center frequency of the

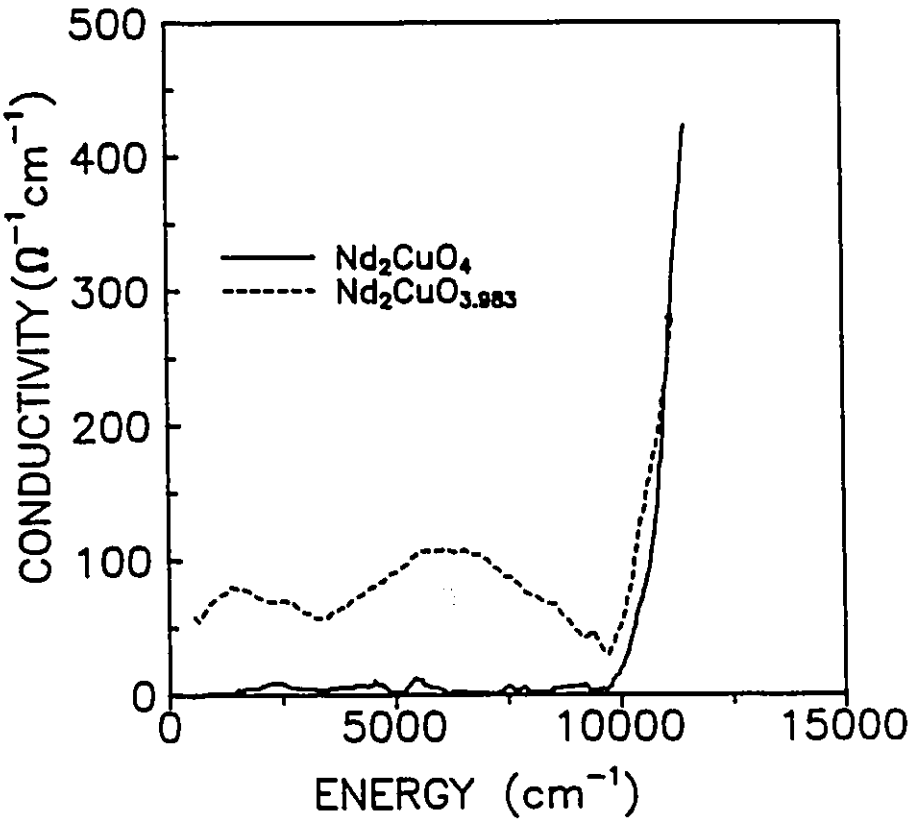

Figure 5.9: Optical conductivity of stoichiometric and slightly oxygen deficient Nd_2CuO_{4-y}. From reference [67].

second component is roughly equal to a crude estimate of the binding energy of a hole associated with an oxygen impurity ($E_I \approx 0.5 - 0.7$ eV). As the level of doping increases, the center of the mid-infrared band moves towards zero frequency. This may be explained if the band centered at E_I grows until the metal-insulator transition where it saturates while the band centered at E_J continues to grow. For doping levels above the metal- insulator transition, a Drude-like absorption centered at zero frequency develops associated with itinerant carriers. In the planar cuprates there is a noticeable transfer of spectral weight from the charge transfer excitation to the mid-infrared and Drude components which can be seen in figure 5.10(a). The transfer of spectral weight from high frequency to low frequencies with increased doping is one of the strongest experimental indications of a highly correlated system [75]. The optical conductivity of the $La_{2-x}Sr_xNiO_4$ [76] system which is shown in figure 5.10(b) exhibits some of the features of the planar cuprates. The system has a larger charge transfer gap (≈ 4 eV), requires much higher levels of doping to become metallic and does not exhibit superconductivity. The band is also composed of two components (≈ 0.6 eV and 1.5 eV). The lower energy peak is at the position of the E_I peak in the planar cuprates. The center of the mid-infrared band is at higher frequency than in the cuprates and does not soften with increased doping levels. This may be due to the absence of the mid-infrared component Thomas *et al.* associate with the antiferromagnetic exhange energy (≈ 0.1 eV). The differences between the mid-infrared continuum in the cuprate and nickelate deserve further study.

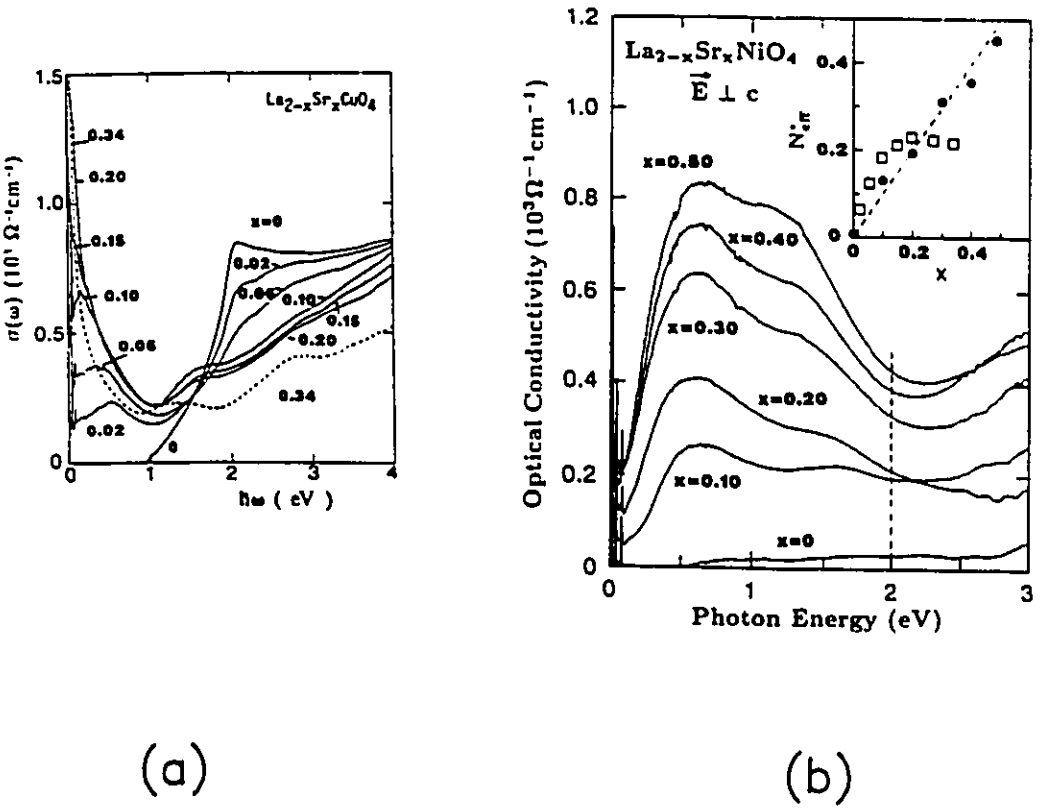

Figure 5.10: (a)Evolution of the optical conductivity with doping in the $La_{2-x}Sr_xCuO_4$ system. Reference 34]. (b)Evolution of the optical conductivity with doping in the $La_{2-x}Sr_xNiO_4$ system. Reference [76].

5.3.4 (Sr,La)TiO_3

This system has been attracted a lot of interest in the past year [46, 77, 78, 79]. The two end members of this mixed crystal system are very different: $SrTiO_3$ is a filled band insulator while $LaTiO_3$ is a Mott- Hubbard insulator. Similar to excess oxygen or La vacancies, substituting Sr for La in $LaTiO_3$ will reduce the occupation of the Ti(3d) type orbitals. Fujishima *et al.* measured the reflectance of a series of $Sr_xLa_{1-x}TiO_3$ samples. The data they present for nominally stoichiometric $LaTiO_3$ is more metallic than the reflectance of insulating $LaTiO_3$ presented in chapter 4 below implying that their sample is somewhat oxidized. They note that the plasma edge moves to higher frequencies with increasing occupation of the $3d$ orbital until $y \approx 0.7$. For larger values of y, the plasma edge begins to move toward zero frequency which they believe is due to an increase in the effective mass of the carriers (the Brinkmann-Rice metal-insulator transition).

5.4 Reflectance of Doped $LaTiO_3$

5.4.1 Room temperature Reflectance

The room temperature reflectance of the doped $LaTiO_3$ samples appears in figure 5.11. Recall that sample A exhibits insulating resistivity behaviour, sample B exhibits a change from insulating to metallic resistivity near 160 K while samples C and D exhibit metallic resistivity at all temperatures. Besides the phonon peaks near 170, 340 and 560 cm^{-1} , the reflectance data indicate the presence of three different absorption processes: free carrier absorption at low frequencies, a mid infrared process associated with broad peak in the reflectance spectrum near 1200 cm^{-1} in the insulating materials and a visible absorption that causes the rise in reflectance above 30000 cm^{-1} . The free carrier component scales with oxygen doping and causes the systematic increase in low frequency reflectance and the development of a plasma

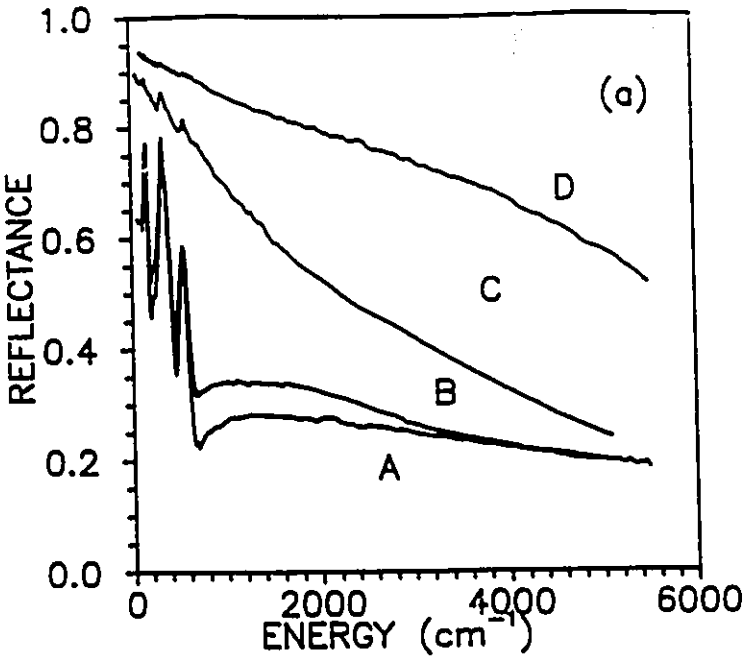

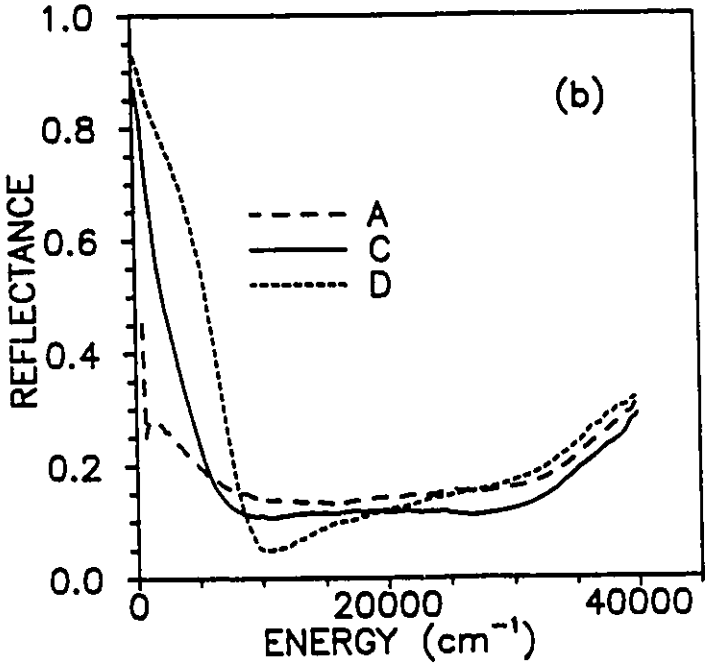

Figure 5.11: (a) 300 K reflectance of A,B,C and D in the far to mid- infrared. (b) 300 K reflectance of A, C and D in the near infrared to visible.

edge that moves to higher frequencies. Note that the phonon related peaks become less prominent with doping but are still visible in the spectrum of the most highly doped sample.

As discussed in chapter 3 there are two approaches to the metal-insulator transition due to correlation: the Mott-Hubbard picture where a gap develops in the quasi-particle density of states when the on-site Coulomb repulsion exceeds the band width and the Brinkman-Rice picture where the effective mass diverges as the short range Coulomb interaction achieves a critical value. The optical properties of the insulating rare earth titanites were discussed within the Mott-Hubbard picture in the previous chapter. Below, both analyses will be applied to the insulator-metal transition in doped $LaTiO_3$.

5.4.2 Mott-Hubbard Picture

As it is easier to see doping induced changes in electronic structure in the optical conductivity a Kramers-Kronig analysis was performed. The reflectance was extended to zero frequency via a Drude extrapolation consistent with the measured dc resistivity for samples C and D while for samples A and B constant low frequency reflectance was assumed. As discussed in chapter 4, the uncertainty in the Kramers-Kronig derived spectral functions is very large for frequencies above 10000 cm^{-1} even though the reflectance was measured to 40000 cm^{-1} .

In figure 5.12 the real part of the optical conductivity is shown for samples A, C and D. Note the increased spectral weight at low frequencies for samples C and D. The loss of infrared spectral weight above 10000 cm^{-1} in sample D is yet another indication that $LaTiO_3$ is a strongly correlated system. The midinfrared absorption is associated with transitions placing two electrons on one site. Qualitatively, the spectral weight associated with this process is proportional to the number of filled sites and should decrease as electrons are removed from the system [75]. It is curious

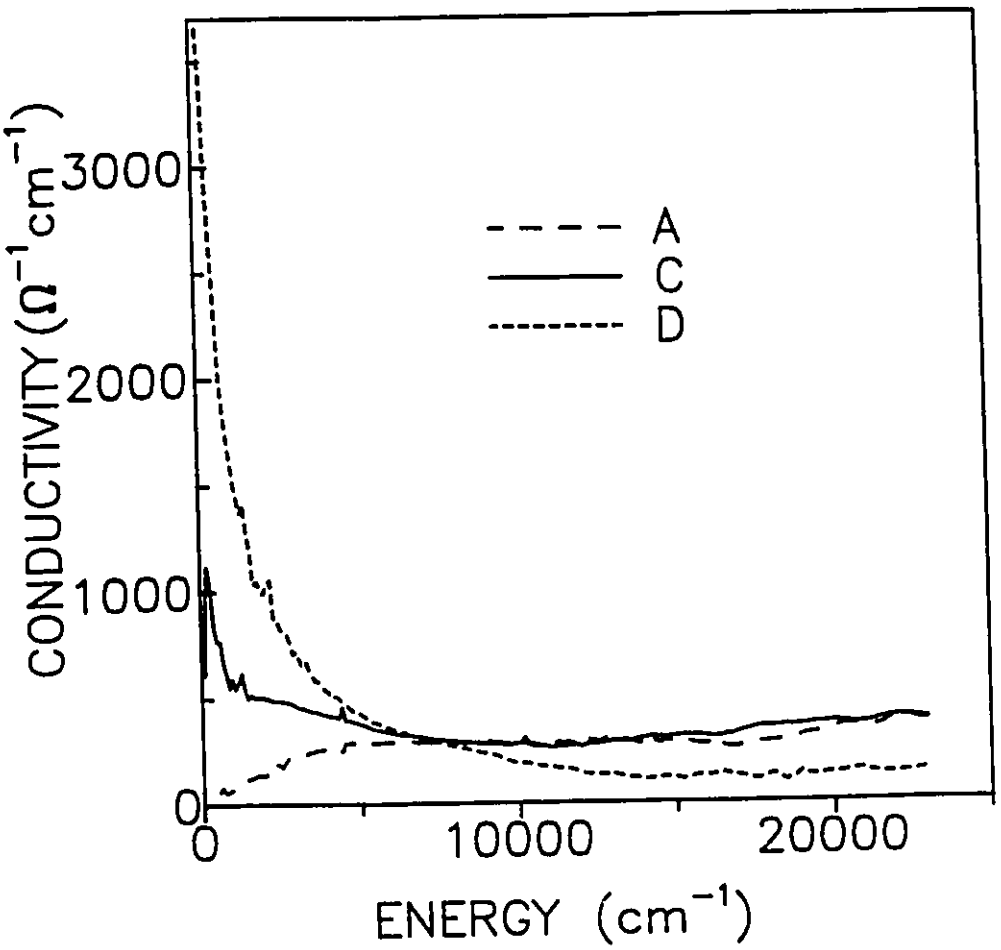

Figure 5.12: Room temperature optical conductivity vs. frequency for doped $LaTiO_3$ samples A, C and D.

that there does not appear to be any loss of infrared spectral weight in sample C. It may be that it is obscured by the uncertainty of the Kramers-Kronig derived spectral functions in this region.

Let us now try to model the effects of doping on the reflectance and optical conductivity. The dielectric function for $LaTiO_3$ will include a Lorentzian to represent the visible range charge transfer process and other Lorentzians to represent the phonons. Modelling the low frequency electronic response poses a bigger problem. As will be seen below, the mid-infrared absorption in $LaTiO_3$ which corresponds to excitations from the lower to the upper Hubbard subband can be fit by an overdamped Lorentzian. In the ionic model, the doping process will produce empty Ti(3d) sites. Electrons adjacent to empty sites are free to move to these sites. The optical conductivity of the Hubbard model has been calculated numerically recently [80] for both the zero and one hole (electrons removed) cases. The spectrum for zero holes consists of a band centered around U. When one electron is removed, some spectral weight appears near zero frequency while some persists near U. It is clear that such a system, especially for low doping levels, is not a free electron gas. Only those electrons adjacent to empty Ti sites are free to respond instantaneously to an external electric field. The response will be retarded for electrons surrounded by filled sites. For lack of a better term, the zero frequency absorption will be referred to as the "Drude" peak in our analysis.

Least square fits to the reflectance and optical conductivity were made using a dielectric function (equation 2.1) consisting of a Drude (D) contribution and Lorentzians to represent the phonons (i) , the midinfrared absorption (M) and the visible absorption (V):

$$\epsilon = \epsilon_\infty - \frac{\omega_{pD}^2}{\omega^2 + i\Gamma_D\omega} + \sum_i \frac{\omega_{pi}^2}{(\omega_{0i}^2 - \omega^2) - i\Gamma_i\omega} + \sum_{j=M,V} \frac{\omega_{pj}^2}{(\omega_{0j}^2 - \omega^2) - i\Gamma_j\omega} \qquad (5.5)$$

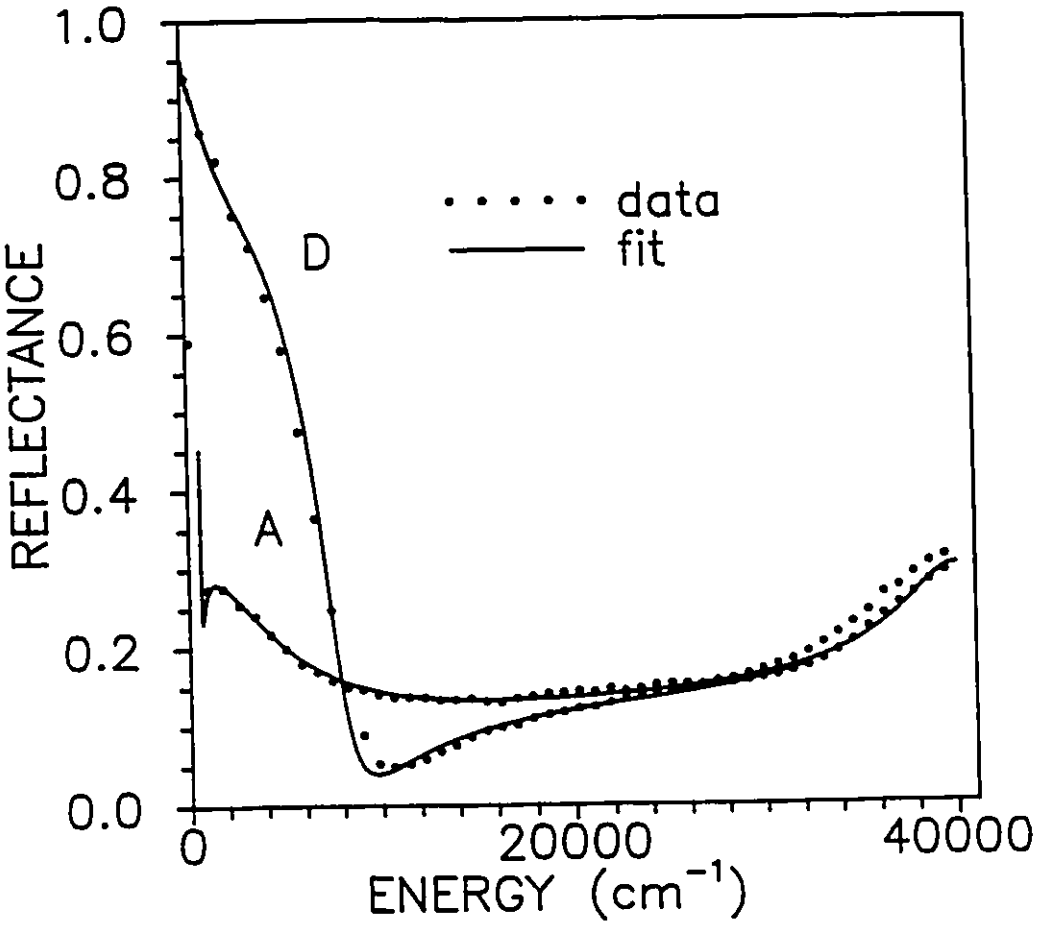

Figure 5.13: Reflectance of the most metallic and most insulating - samples D and A respectively - compared with the sum model fits.

To begin, the reflectance and conductivity of the most insulating sample were fit. For the fits of the more metallic samples, ε_∞ and the visible oscillator constants were held fixed as the reflectance spectra were not measured to high enough frequencies to say whether there are systematic changes in the high frequency components. The fitting parameters appear in table 5.3 and the quality of the fits to samples A and D appear in figure 5.13.

In figure 5.14 one can view the evolution of the fitted Drude and mid-infrared components with doping and compare them to the measured optical conductivity. The mid-infrared component appears to narrow and shift to lower frequencies with increased doping. Part of this shift may be due to structural changes. We know that the onset of the mid-infrared absorption tends to lower frequencies as the Ti-O-Ti bond straightens out. The Ti oxidation state controls $\theta(\mathrm{Ti}-\mathrm{O}-\mathrm{Ti})$. Sunstrom *et al.* observe a systematic increase in $\theta(\mathrm{Ti}-\mathrm{O}-\mathrm{Ti})$ as the Sr:La ratio is increased in $La_{1-x}Sr_xTiO_3$ [79]. The mid-infrared band in the planar cuprates exhibits a similar evolution with increased hole doping [34, 35, 36].The origin of the mid-infrared band in the planar cuprates is different than in the titanites - it is present in stoichiometric $RTiO_3$ but is induced by doping in the planar cuprates - but both charge transfer and Mott-Hubbard insulators show the transfer of spectral weight from high to low frequencies with increased doping.

Table 5.3: Parameters for sum model fits to reflectance and optical conductivity for samples A,B, C and D. Lorentzians 1-3 represent phonons while Lorentzians D,M represent the Drude and midinfrared oscillators discussed in the text. $\epsilon_\infty = 3.92$, while the center frequency, width and plasma frequency of the visible oscillator are 39600,4900 and 37000 cm^{-1} respectively. In the table, all frequencies and dampings are in cm^{-1}.

	A			B		
i	ω_{0i}	Γ_i	ω_{pi}	ω_{0i}	Γ_i	ω_{pi}
1	170	20	600	169	22	640
2	340	56	1100	338	64	1260
3	545	52	720	548	60	830
D	0	540	1100	0	280	1080
M	6600	22700	19400	4130	13600	15700
	C			D		
i	ω_{0i}	Γ_i	ω_{pi}	ω_{0i}	Γ_i	ω_{pi}
1	160	35	820	172	49	920
2	340	30	930	340	139	1650
3	571	32	605	565	81	900
D	0	360	4280	0	430	9000
M	890	9100	16300	655	3400	15500

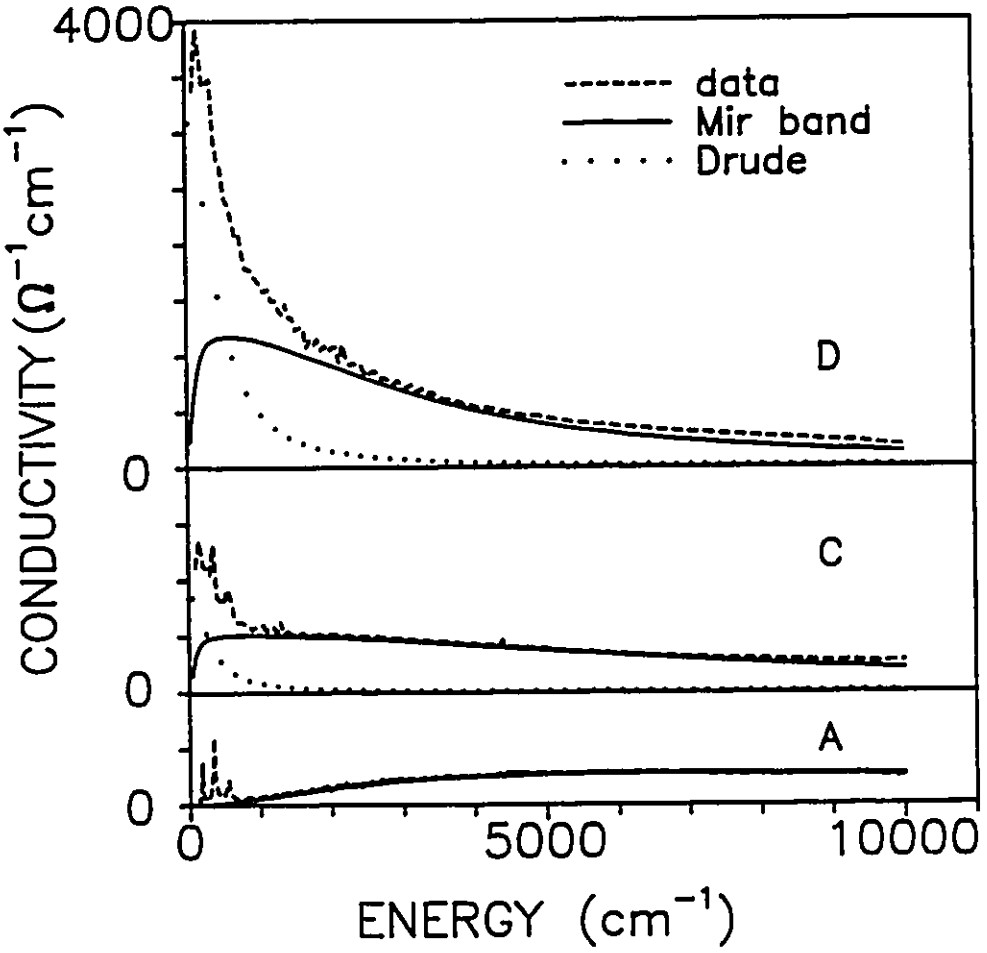

Figure 5.14: Comparison of the measured $\sigma(\omega)$ of the $LaTiO_{3+x}$ system with the Drude and midinfrared components of the sum model fits.

5.4.3 Brinkman-Rice Picture

Recall that the Brinkmann-Rice model of the correlation induced metal-insulator transtion predicts an enhancement of the electron mass as U approaches a critical value. Optical measurements can be used to measure mass enhancements, as has been done for the heavy fermion materials $CePd_3$ and URu_2Si_2 [81, 82]. One uses the generalized Drude theory in which both the scattering rate and effective mass become frequency dependent [83]. The low frequency limit of the renormalized mass is close to the measured specific heat mass enhancements for both these materials.

The usual Drude expression for the conductivity, which is obtained from a dielectric function consisting of a Lorentzian of width Γ and strength ω_p^2 placed at the origin, becomes

$$\sigma(\omega) = \frac{1}{4\pi} \frac{\omega_{eff}^2}{\Gamma_{eff} - i\omega} \tag{5.6}$$

where

$$\Gamma_{eff} = \frac{\Gamma(\omega)}{1 + \lambda(\omega)} \tag{5.7}$$

and

$$\omega_{eff}^2 = \frac{\omega_p^2}{1 + \lambda(\omega)} \tag{5.8}$$

The plasma frequency ω_p (in cm^{-1}) is related to the carrier density n (in cm^{-3}) via:

$$n \approx 1.1 \times 10^{13} (m^*/m) \omega_p^2 \tag{5.9}$$

One can determine $\lambda(\omega)$ and $\Gamma(\omega)$ from the dielectric functions obtained by Kramers-Kronig analysis of the reflectance using the following equations:

$$\Gamma(\omega) = \frac{\omega_p^2}{\omega} \frac{\varepsilon_2}{\varepsilon_1^2 + \varepsilon_2^2} \tag{5.10}$$

$$\lambda(\omega) = \frac{\omega_p^2}{\omega^2} \frac{\varepsilon_1}{\varepsilon_1^2 + \varepsilon_2^2} - 1 \tag{5.11}$$

This analysis applies only to the itinerant carriers in the system and any interband or phonon contributions to the dielectric function must be subtracted before calculating $\lambda(\omega)$ and $\Gamma(\omega)$. One sign that the analysis has been done correctly is if the frequency dependent scattering rate mirrors the temperature dependence of the dc resistivity. Physically, $\frac{d\Gamma(\omega)}{d\omega}$ should have the same sign as $\frac{d\rho(T)}{dT}$ where ρ(T) is the dc resistivity. In URu_2Si_2 for example, the dc resisitivity increases with temperature until 70 K where it begins to decrease [84]. Likewise, the low frequency slope of $\Gamma(\omega)$ is positive for temperatures below 70 K but negative above 70K [82].

Applying the generalized Drude analysis to $LaTiO_3$ poses a difficult problem. The two component analysis of section 5.4.2 suggests that transitions associated with placing two electrons on one site persist in samples C and D.

As a first approach, one can subtract ε_∞ and the phonon and visible oscillator contributions from the dielectric function obtained by Kramers- Kronig analysis. Assuming that n is equal to 1.3 $\times 10^{22}$ cm^{-3} and 1.0 $\times 10^{22}$ cm^{-3} for samples C and D respectively one obtains $\lambda(\omega)$ shown in figure 5.15. The carrier densities are obtained from a consideration of the oxidation state of Ti in the samples and the density of Ti atoms in the lattice (1.6 $\times 10^{22}$ cm^{-3}). Sample C is closer to the metal- insulator transition than sample D and at 300 cm^{-1} the mass is significantly larger for sample C than sample D in agreement with the Brinkmann-Rice picture. However, something is amiss. Evaluation of various model $\Gamma(\omega)$ shows [85] that

$$\lambda(\omega) \propto \frac{d\Gamma(\omega)}{d\omega} \tag{5.12}$$

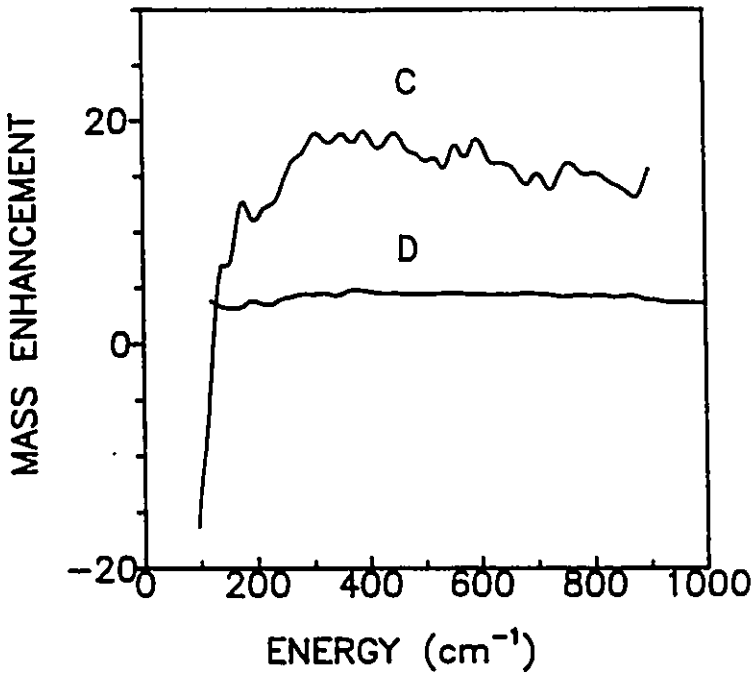

Figure 5.15: Mass enhancement factor for samples C and D with no subtraction of mid-infrared contribution.

For sample C, ρ_{dc}(T) monotonically increases between 4 and 300 K as seen in figure 5.2 and thus the mass enhancement should be positive. The low frequency negative mass enhancement indicates that one needs to subtract off a mid-infrared component for sample C. Apparently, there is still significant spectral weight associated with transitions which place two electrons on one site in sample C where approximately one fifth of the sites are empty.

The actual shape of the midinfrared band is not known. The only other approach we can take is to examine the Drude parameters obtained in the two component fits. This is equivalent to subtracting out the overdamped Lorentzian used to represent the mid- infrared absorption in addition to the phonon and visible oscillator contributions. But we need an estimate of the itinerant carrier density for samples

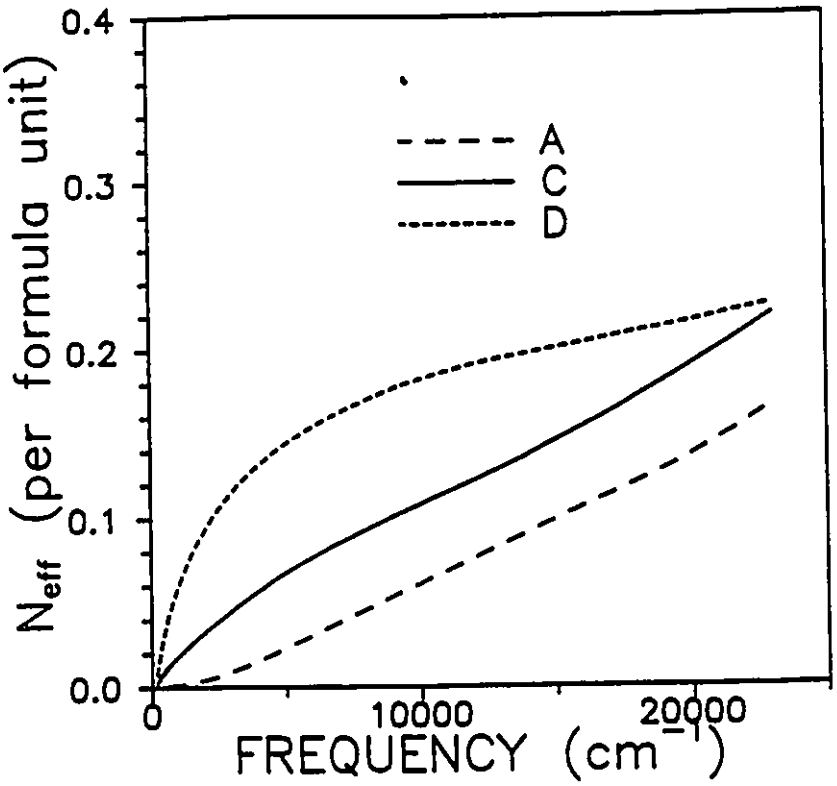

Figure 5.16: The effective number of carriers involved in optical transitions versus frequency for insulating $LaTiO_3$ sample A and metallic samples C and D.

C and D. In some systems this can be obtained using the partial sumrule of section 2.4.

$N_{eff}(\omega)$ is calculated using the optical conductivity curves of figure 5.12 and equation 2.21 and is shown for samples A, C and D in figure 5.16. For sample D, most of the spectral weight associated with the mid-infrared band ($\approx$ 0.2 electrons per formula unit - see section 4.2.2 is transferred below 10000 cm^{-1} . Recall that the Ti oxidation state of sample D is roughly 3.4 (see table 5.2). If most of the spectral weight due to the Ti(3d) electrons was associated with intraband transitions, as it is for the valence electrons in Al [86], then one would expect a spectral weight of roughly 0.6 electrons per formula unit for the itinerant carriers (the low frequency peak in the optical conductivity) of sample D.

Two observations may be significant. The spectral weight associated with itinerant carriers in the $3d^1$ system $SrVO_3$ is about 0.16 [25]. In grossly oxygen deficient $SrTiO_{3-x}$ Hall measurments give carrier densities less than one would expect in the one band model where an oxygen vacancy donates two electrons to the conduction band [51]. Gong *et al.* explain their Hall measurements using a two band model. Band structure calculations show that a heavy and a light electron band are degenerate at the Γ point. The carrier density in light electron band will dominate transport properties. For parabolic bands, where the density of states $\rho(E) \propto (m^*)^{3/2}E^{1/2}$ [87], the ratio of the carrier density in the two bands will be $(m_1^*/m_2^*)^{3/2}$. The two band model for early transition metal perovskites is supported by calculations of the mean free path in $SrVO_3$ where the room temperature resistivity is about 750 $\mu\Omega$cm [25]. In the Drude model the mean free path (l) in Å is given by the equation 5.13 where the carrier density n is in cm^{-3} and the resistivity ρ is in Ωcm.

$$l = \frac{1.27 \times 10^{12}}{n^{2/3}\rho} \tag{5.13}$$

In the one band model, n = density of V atoms = 1.8×10^{22} cm^{-3} and l = 2.4 Å. In the two band model, assuming $n = 2.9 \times 10^{21}$ cm^{-3}, l is 8.3 Å. Both are quite small, but 2.4 Å is of the order of the interatomic distance and is not physical.

The effective mass of sample D can be estimated by assuming 0.2 itinerant carriers per formula unit (all of the midinfrared spectral weight is transferred to the "Drude" peak). Using $\omega_p \approx 9000$ cm^{-1} from table 5.3 and formula 5.9 we obtain $m^* = 3.5$ which is larger than the conduction band mass of $SrTiO_3$. The mass enhancement is modest but may be an indication of the Brinkmann-Rice effect. Why should the mass be enhanced? Recall that m^* diverges as U approaches U_c which is proportional to the bandwidth (section 3.5). It is possible that changes in Ti oxidation state change $\theta(Ti - O - Ti)$, the bandwidth and thus U_c.

In summary, features of both the Mott-Hubbard model and the Brinkman-Rice model are observed in the optical properties of doped $LaTiO_3$. The final question which will be considered in this chapter is the origin of the temperature induced metal-insulator transition in sample B.

5.4.4 Temperature induced metal-insulator transition in lightly doped $LaTiO_3$

Certain slightly oxidized samples (such as B) of $LaTiO_3$ and $CeTiO_3$ exhibit minima (metal-insulator transitions) in their resistivity curves [14, 26]. Before the phase diagram was established by Lichtenberg *et al.* , the temperature induced metal-insulator transition was believed to be a feature of stoichiometric $LaTiO_3$ and two possible explanations were given for the transition [14]. In the first model, $LaTiO_3$ is a narrow band-gap semiconductor. Having four formula units per unit cell, it was argued that $LaTiO_3$ might be a filled band insulator. Although the $RTiO_3$ perovskites are Mott-Hubbard insulators, let us consider the semiconductor model for the sake of completeness.

In this model, the midinfrared absorption is an interband excitation. For $LaTiO_3$ we extract a band gap (E_g) of roughly 550 cm^{-1} . We can use the equations of semiconductor theory [88] to predict the temperature dependence of the carrier concentration, carrier mobility and resistivity. Assuming acoustic phonon scattering only, the dc conductivity would be given by

$$\sigma(T) = C \int_0^\infty \frac{x^{1/2} dx}{\exp(x - \zeta) + 1} \tag{5.14}$$

where C is a constant and $\zeta = E_g/2kT$. The predictions of this equation are shown in figure 5.17. This model cannot reproduce the resistivity minimum even if one includes the effects of other scattering mechanisms besides acoustic phonon scattering.

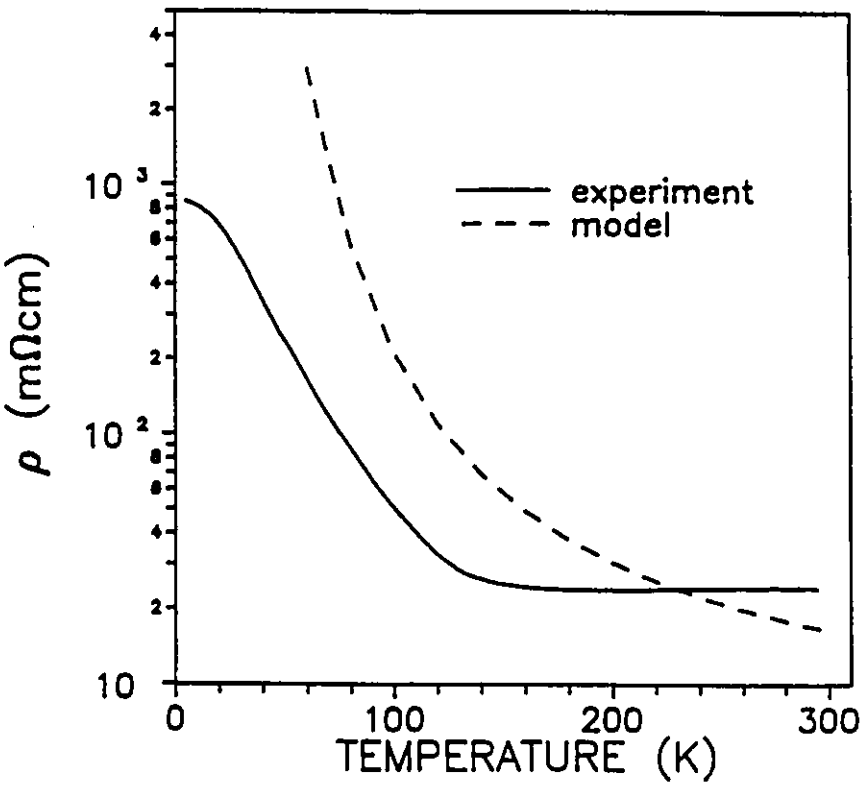

Figure 5.17: Resistivity of sample B compared with the predictions of the narrow band semiconductor model.

The second model assumes that $LaTiO_3$ is an itinerant antiferromagnet where the metal-insulator transition is caused by the long range ordering. This model is based on the observation that the resistivity minimum occurs in the proximity of the antiferromagnetic (AF) transition [14]. In an early attempt to explain why NiO was an insulator rather than a metal J.C. Slater noted that once AF order is established, an electron would experience a periodic exchange potential which could, in principle, induce a gap at the Fermi surface [89]. The reflectance of sample B was measured at various temperatures between 20 and 300K to determine the changes in the midinfrared absorption between the barely metallic (high temperature) and the localized regimes. These measurements appear in figure 5.18.

The optical conductivity as a function of temperature appears in figure 5.19. The dashed lines in this figure are linear fits to optical conductivity data between 675 and 900 cm^{-1} . Note that the fits intersect the frequency axis at progressively lower frequencies as the temperature increases suggestive of a model in which the gap closes continuously with temperature rather than opening up with the onset of antiferromagnetic order. These observations may be explained using the same model used for the blue shift of the mid- infrared absorption in the $RTiO_3$ series: the gap between Hubbard subbands decreases as the Ti-O-Ti bond straightens out. Eitel *et al.* have measured the Ti-O-Ti bond angle in $LaTiO_3$ as a function of temperature and find that it straightens out as the temperature increases, albeit by an extremely small amount (an increase of only 0.4 degrees between 10 and 298 K)[90].

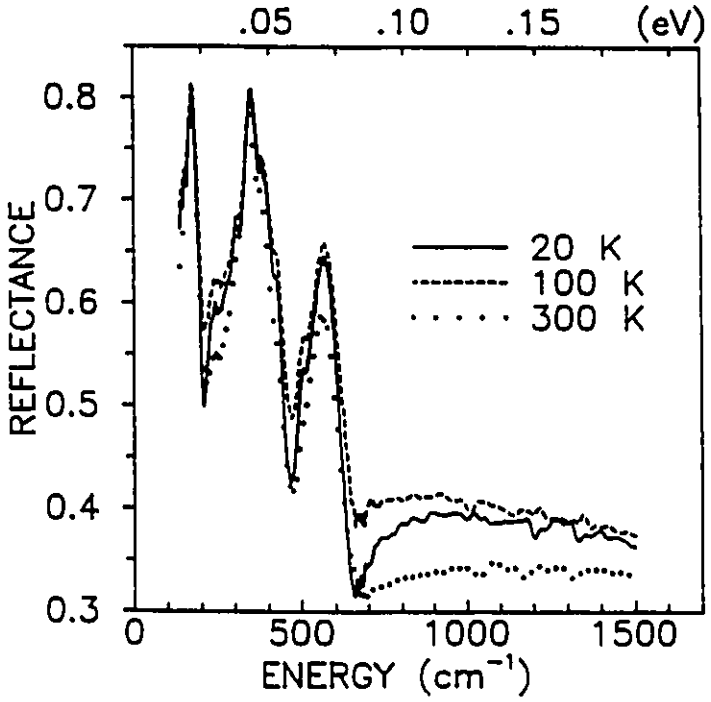

Figure 5.18: Reflectance versus frequencies measured at various temperatures for sample B.

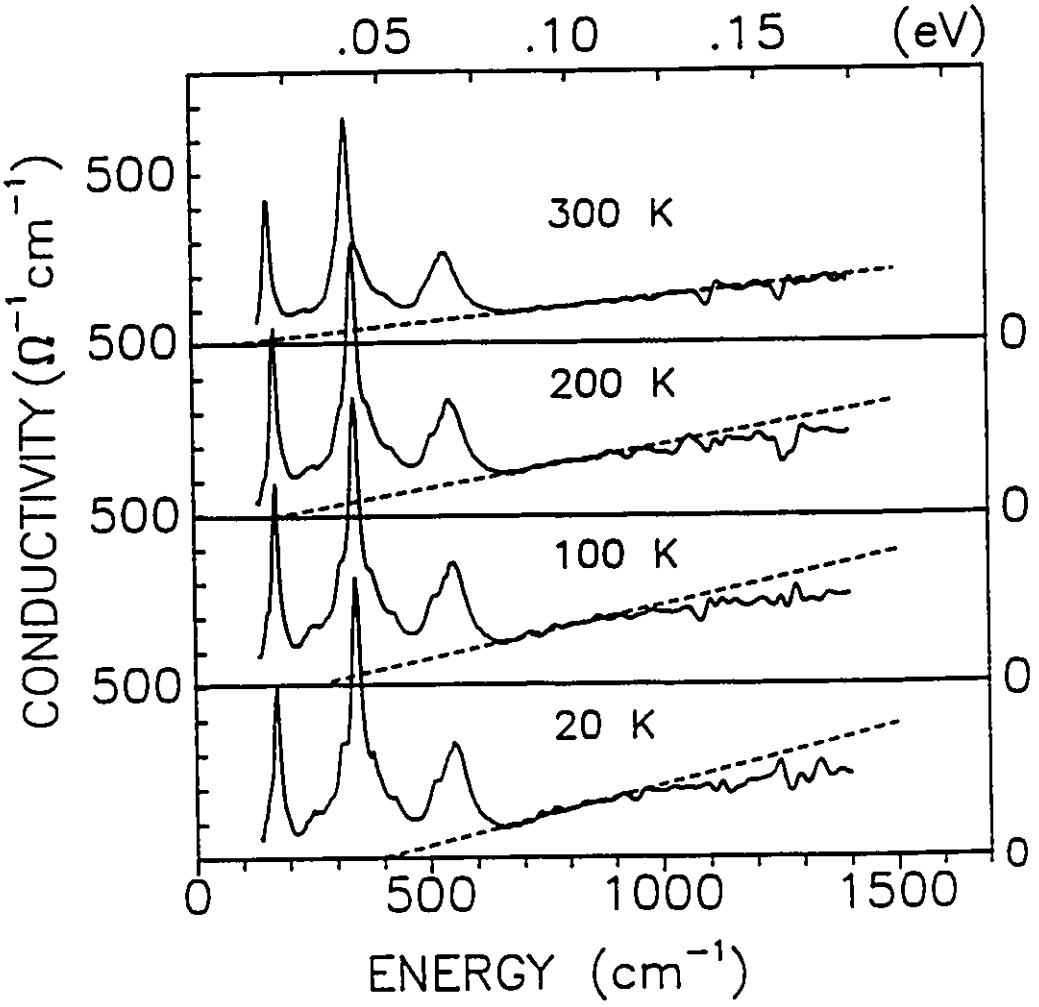

Figure 5.19: Temperature dependence of the real optical conductivity for a sample exhibiting a change from insulating to metallic resistivity behaviour near 160 K

Chapter 6

Conclusions

We have studied the Mott metal-insulator transition. This is one of the large group of problems concerning electron correlation which also includes superconductivity, transition metal magnetism and heavy fermion behaviour.

Reflectance spectroscopy has been a useful experimental probe; we now have a picture of the electronic structure of the rare earth titanites. There are several important energies in a system close to a Mott metal-insulator transition: the band-width, W, the on-site coulomb repulsion , U, and cation- anion charge transfer energy, Δ. In the insulating $RTiO_3$ series we were able to observe the effects of a systematic decrease of W while holding U constant. The smallest optical gap is associated with the the process: $2Ti^{3+} \longrightarrow Ti^{2+} + Ti^{4+}$. The minimum energy required for these charge fluctuations increases systematically from approximately 0.075 eV in $LaTiO_3$ to 0.75 eV in $GdTiO_3$ and is controlled by the Ti-O-Ti bond angle. The next highest optical gap ($\Delta \approx 5$ eV) is associated with O(2p)-T(3d) charge transfer. $U \approx 1$ eV while the W decreases from about 1 eV in $LaTiO_3$ to 0.5 eV in $GdTiO_3$.

Several other studies can be suggested. $RTiO_3$ compounds can be compared with the structurally identical $RNiO_3$. On the $\Delta - U$ chart (figure 3.4) $RNiO_3$ compounds lie on the Δ boundary and presumably are charge transfer rather than

Mott insulators in the ZSA framework. The same crystal structure systematics apply, that is the Ni-O-Ni bond angle decreases as R's ionic radius becomes smaller. The insulator-metal transitions observed in $RNiO_3$ (R= La,Pr,Nd,Sm and Eu) have recently been explained as being due to closing of the charge transfer gap as the electronic bandwidth increases [8]. The Ni-O-Ni bond angle in $PrNiO_3$ increases by 1.5° between 300 and 673 K and Torrance *et al.* suggest that when this bond straigtens out the charge transfer gap closes inducing the metal-insulator transitions in $PrNiO_3$, $NdNiO_3$, and $SmNiO_3$ which occur at 135, 201 and 403 K respectively.[8]. Optical measurements on the $RNiO_3$ system would provide more information on the electronic structure of highly correlated charge transfer insulators. ReO_3 is the most metallic d^1 oxide. One could conceivably reduce the number of electrons in the $5d$ orbital by making $(W, Re)O_3$ alloys. Data on these alloys may be important for clarifying the differences in electronic structure between free electron and highly correlated metals. $SrTiO_3$ is closely related to $LaTiO_3$. Like the planar cuprates doped $SrTiO_3$ is superconducting albeit with a very low transition temperature (0.3 K) [92]. It is also possible to produce highly non-stoichiometric metallic samples [51]. One of the most interesting features of stoichiometric $SrTiO_3$ is the soft vibrational mode which is linked to the antiferrolectric transition. The behaviour of this mode as a function of doping has not, to the author's knowledge been studied. As mentioned in chapter 5 doping produces a mid-infrared band in $SrTiO_3$ the origin of which is not yet clear. A systematic study of the transport and optical properties of doped $SrTiO_3$ may shed some light on the interplay of electron-phonon interactions, correlation and superconductivity.

By doping $LaTiO_3$ we have been able to induce an insulator-metal transition. We have observed a transfer of spectral weight from high frequency to low which is an indication of a highly correlated system, as discussed in section 3.2. It appears that the optical conductivity of a doped Mott-Hubbard system can be modeled using

two oscillators, one for the itinerant carriers and one for transitions from the lower to the upper Hubbard band. The low frequency optical conductivity is not Drude-like even when there are a large number of empty sites. The strength of the mid- infrared band is considerable in sample D with stoichiometry $La_{.88}TiO_3$ where approximately forty percent of the sites are empty. We have also seen that the frequency dependent mass and scattering rate formalism is difficult to apply to a Mott-Hubbard system.

The chemical analysis and structural considerations of the doped $LaTiO_3$ samples are controversial. They support doping by cation vacancies which is more reasonable structurally than excess oxygen . A detailed structural study of the $La_{1-y}TiO_3$ system should unambiguously establish the cation vacancy model.

Finally, $LaTiO_3$ and the Mott insulator V_2O_3 [4] can be compared. The temperature induced insulator-metal transition in V_2O_3 produces strikingly similar changes optical conductivity [38] to the doping induced transition in $LaTiO_3$. In both systems, the insulator-metal transition is accompanied by a decrease in cell volume [93]. Accordingly, application of 26 kbar destroys the low temperature antiferromagnetic phase of V_2O_3 [93]. It would be interesting to study the effects of high pressure on stoichiometric $LaTiO_3$.

Appendix A

Linear Combination of Atomic Orbitals

A.1 LCAO formalism

To determine the band structure we have to solve the set of independent electron Schrodinger equations where H is the Hamiltonian while $E(\underline{k})$ and $\psi(\underline{k}) = \sum_\alpha u_\alpha \chi_\alpha(\underline{k})$ are the energy and wave function for crystal momentum $\underline{k}$:

$$\sum_\beta H_{\alpha\beta}(\underline{k})u_\beta = E_{\underline{k}}u_\alpha$$

The basis functions are Bloch sums ($\chi_\alpha(\underline{k})$). In the LCAO approximation (Linear Combination of Atomic Orbitals) $\varphi_{..}(\underline{r} - \underline{r}_i)$ is an atomic orbital and the Bloch sum is of the form

$$\chi_\alpha(\underline{k}) = \frac{1}{\sqrt{N_\alpha}} \sum_i e^{i\underline{k}\cdot\underline{r}_i}\varphi_\alpha(\underline{r} - \underline{r}_i)$$

The sum is for one particular orbital type over atoms with identical environments. For example, in ABO_3 compounds there are two different O sites (AO and BO_2 planes). On the other hand A and B have only one site each.

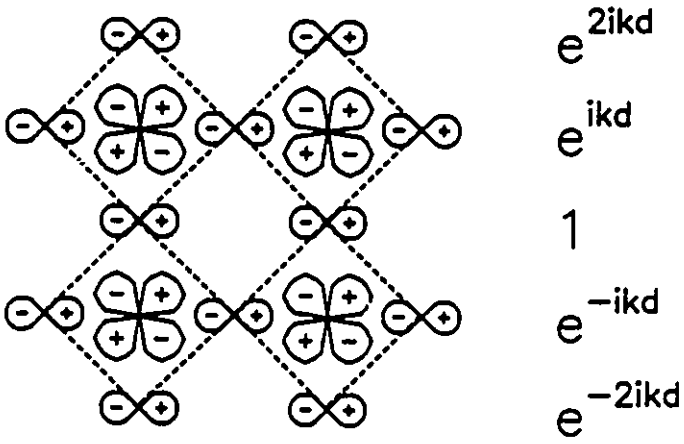

Figure A.1: Orientation of d_{xz} and p_x orbitals in cubic ABO_3.

A.2 Determination of Matrix Elements

Consider k parallel to z and the matrix element between d_{xz} and p_x orbitals in the BO_2 plane as shown in figure A.1.

The matrix element can be derived as follows where there are equal numbers (N) of d_{xz} and p_x orbitals:

$$\langle p_x|H|d_{xz}\rangle = \frac{1}{N}\langle\sum_j e^{-i\underline{k}\cdot\underline{r}_j} p_x(\underline{r}-\underline{r}_j)|H|\sum i e^{i\underline{k}\cdot\underline{r}_i} d_{xz}(\underline{r}-\underline{r}_i)\rangle$$

$$= \frac{1}{N}\sum_i\sum_j e^{i\underline{k}\cdot(\underline{r}_i-\underline{r}_j)}\langle p_x(\underline{r}-\underline{r}_j)|H|d_{xz}(\underline{r}-\underline{r}_i)\rangle$$

Consider a d_{xz} orbital at the origin and the sum j over all the p_x orbitals. There are

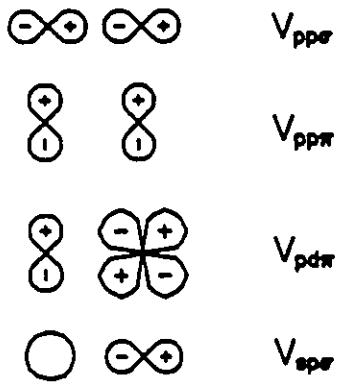

Figure A.2: Labels for various LCAO matrix elements

N such identical sums and we have

$$\langle p_x|H|d_{xz}\rangle = \sum_j e^{i\underline{k}\cdot(\underline{r}-\underline{r}_j)}\langle p_x(\underline{r}-\underline{r}_j)|H|d_{xz}(0)\rangle$$

If we now assume that $\langle p_x(\underline{r}-\underline{r}_j)|H|d_{xz}(0)\rangle$ is non-zero only for nearest neighbours one obtains

$$\langle p_x|H|d_{xz}\rangle = e^{i\underline{k}\cdot\underline{d}}V_{pd\pi} - e^{-i\underline{k}\cdot\underline{d}}V_{pd\pi} = 2iV_{pd\pi}\sin kd$$

The notation $V_{pd\pi}$ ($V_{pd\sigma}$) means the matrix element between a p and a d orbital which would become negative (be unchanged) upon rotation of 180° about the axis joining the two orbital centers. Other matrix elements are illustrated in figure A.2.

A.3 Harrison's Matrix Elements

Harrison's contribution [52] was to develop formulae for the matrix elements involving only the nearest neighbour distance (d). The formulae required for the calculation in chapter 3 are listed below:

$$V_{ll'm} = \eta_{ll'm}\frac{\hbar^2}{md^2}$$

where $\frac{\hbar^2}{m} = 7.62\text{eV}\text{Å}^2$ and $\eta_{pp\pi} = -0.81$.

$$V_{ld'm} = \eta_{ll'm}\frac{\hbar^2 r_d^{3/2}}{md^{7/2}}$$

r_d is specific to the transition metal involved in the interaction ($r_d(\text{Ti}) = 1.08$ Å) and

$$\eta_{sd\sigma} = -3.16$$

$$\eta_{pd\sigma} = -2.95$$

$$\eta_{pd\pi} = 1.36$$

These matrix elements refer of course to very symmetric orientation of the orbitals. For less symmetric orientations, as for the calculation of the effect of the buckling of the Ti-O network in the rare earth titanites, one can use Slater and Koster's tables of interatomic matrix elements as functions of direction cosines l, m and n of the vector from the left state to the right state [91].

A.4 LCAO $SrTiO_3$ band structure

Mattheis's APW calculations of the band structure of cubic $SrTiO_3$ [22] showed that there is no Sr character to the states near the Fermi level. Thus one considers only O(2s), O(2p) and Ti(3d) atomic orbitals.

Consider transport parallel to the z-axis. The symmetry group of $\underline{k} = (0,0,1)$ is D_4, the group of the square. One must consider four representations $(\Delta_1, \Delta_2, \Delta_2', \Delta_5)$. In the Δ_2' representation, d_{xy} does not mix with any other state thus producing a flat band with of energy ϵ_d. The states which mix in the other representations are:

$$\Delta_1 : s, p_z, d_{3z^2-r^2}$$

$$\Delta_5 : p_x, p_y, d_{xz}, d_{yz}$$

$$\Delta_2 : s, p_z, d_{x^2-y^2}$$

The matrix which must be diagonalized for the Δ_1 representation is:

$$\begin{pmatrix}
\epsilon_s & 0 & 0 & 0 & 0 & 0 & -V_{sd\sigma} \\
0 & \epsilon_p & 0 & 0 & 0 & 4E_{xx}\cos k_z d & 0 \\
0 & 0 & \epsilon_s & 0 & 0 & 0 & -V_{sd\sigma} \\
0 & 0 & 0 & \epsilon_p & 0 & 4E_{xx}\cos k_z d & 0 \\
0 & 0 & 0 & 0 & \epsilon_s & 0 & 2V_{sd\sigma}\cos k_z d \\
0 & 4E_{xx}\cos k_z d & 0 & 4E_{xx}\cos k_z d & 0 & \epsilon_p & 2iV_{pd\sigma}\sin k_z d \\
-V_{sd\sigma} & 0 & -V_{sd\sigma} & 0 & 2V_{sd\sigma}\cos k_z d & -2iV_{pd\sigma}\sin k_z d & \epsilon_d
\end{pmatrix}$$

The matrix which must be diagonalized for the Δ_5 representation is:

$$\begin{pmatrix} \epsilon_p & 4E_{xx} & 4E_{xx}\cos k_z d & 0 \\ 4E_{xx} & \epsilon_p & 0 & 0 \\ 4E_{xx}\cos k_z d & 0 & \epsilon_p & 2iV_{pd\pi}\sin k_z d \\ 0 & 0 & -2iV_{pd\pi}\sin k_z d & \epsilon_d \end{pmatrix}$$

For the states of symmetry Δ_2, the wave function must become negative upon reflection in the plane $x = y$. This rules out all oxygen orbitals in the SrO plane and thus all coupling between orbitals of different phases. The bands are independent of k having energies [52]:

$$\Delta_2 = \epsilon_p$$

$$\Delta_2 = \frac{\epsilon_s + \epsilon_d}{2} \pm \sqrt{(\frac{\epsilon_d - \epsilon_s}{2})^2 + 6V_{sd\sigma}^2}$$

The parameters used for the calculation are listed in table A.1 and the LCAO bands for $SrTiO_3$ are compared with Mattheis's APW bands in figure A.3

Table A.1: Parameters required for LCAO band structure calculation of $SrTiO_3$.

d(Ti-O)	1.95 Å
ϵ_s	-29.14 eV
ϵ_p	-14.13 eV
ϵ_d	-10.22 eV
$V_{sd\sigma}$	-2.56 eV
$V_{pd\sigma}$	-2.25 eV
$V_{pd\pi}$	1.14 eV
E_{xx}	0.159 eV

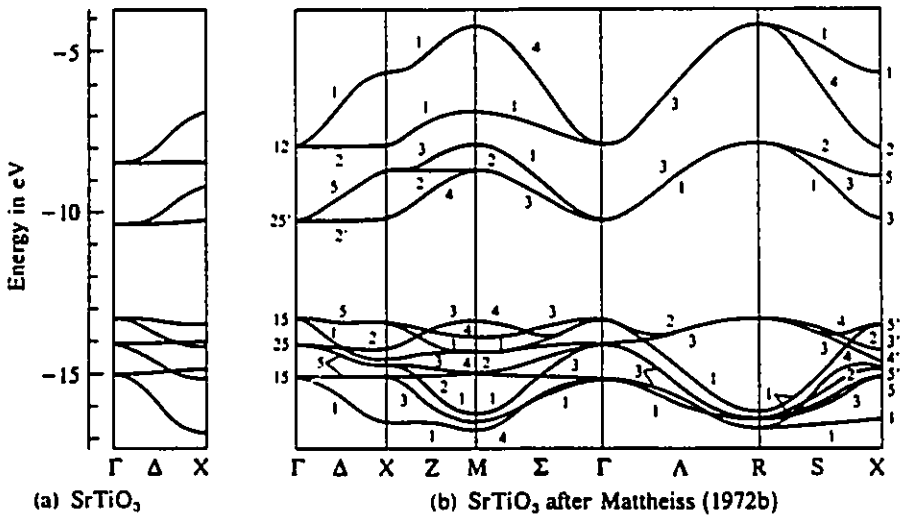

Figure A.3: Comparison of LCAO bands with Harrisons's APW bands for $SrTiO_3$. Reference [52].

Bibliography

[1] Koichi Kitazawa and Setsuko Tajima, "Experimentally Deduced Electronic Structure of the Cuprate Superconductors", in *Some Aspects of Superconductivity* Ed. L. C. Gupta, Nova Scientific Publishers (USA), 1990.

[2] S. Hufner, P. Steiner, I. Sander, F. Reinert and H. Schmitt, Z. Phys. B. **86**, 207 (1992).

[3] M. R. Norman, Phys. Rev. **B40**, 10632 (1989).

[4] S.A. Carter, T.F. Rosenbaum, J.M. Honig, and J. Spalek, Phys. Rev. Lett. **67**, 3440 (1991).

[5] A. Nozaki, H. Yoshikawa, T. Wada, H. Yamauchi and S. Tanaka, Phys. Rev. **B43** (1991).

[6] F. Lichtenberg, T. Williams, A. Reller, D. Widmer and J.G. Bednorz, Z. Phys. B. **84**, 369 (1991).

[7] R. J. Cava, B. Batlogg, J. Krajewski, H. F. Poulsen, P. Gammel, W. F. Peck, Jr. and L. W. Rupp, Jr., Phys. Rev. **B44**, 6973 (1991).

[8] J. B. Torrance, P. Lacorre, and A. I. Nazzal, E. J. Ansaldo, Ch. Niedermayer, Phys. Rev. **B45**, 8209 (1992).

[9] H. J. DeBoer and E. J. W. Verwey, Proc. Phys. Soc. London, **A49**, 59 (1937).

[10] J. Zaanen and G. A. Sawatsky, J. Sol. St. Chem. **88**, 8 (1990).

[11] G.V. Bazuev, G. P. Shveikin, Inorg. Mater. **14**, 201 (1978).

[12] P. Ganguly, Om. Parkash, and C. N. R. Rao, phys. stat. sol. (a) **36**, 669 (1976).

[13] J.E. Greedan, J.Less Comm.Met. **111**, 335, (1985).

[14] D. A. Maclean, J.E. Greedan, Inorg. Chem **20**, 1025 (1980).

[15] D. A. Maclean, Kan Seto and J.E. Greedan, J. Sol. St. Chem. **40**, 241 (1981).

[16] R. D. Shannon and C. T. Prewitt, Acta Cryst. **25**, 925 (1969).

[17] J.S. Toll, Phys. Rev. **104**, 1760 (1965).

[18] Frederick Wooten *Optical Properties of Solids*, New York: Academic, 1972

[19] Edward D. Pallik ed., *Handbook of Optical Constants of Solids*, (New York: Academic, 1985)

[20] N. W. Ashcroft and N. D. Mermin, *Solid State Physics*, Philadelphia : Holt, Rinehart and Winston, 1976.

[21] Donald Long, *Energy Bands in Semiconductors*, New York: John Wiley and Sons, Inc., 1968.

[22] L. F. Mattheis, Phys. Rev. **B6**, 4718, (1972).

[23] C. N. King, H. C. Kirsch and T. H. Geballe, Sol. St. Comm. **9**, 907 (1971).

[24] C Lee, J. Destry and J. L. Brebner, Phys. Rev. **B 11**, 2299 (1975).

[25] P. Dougier, John C. Fan, John B. Goodenough, J. Sol. St. Chem, **14**, 247 (1975).

[26] F. Lichtenberg, D. Widmer, J.G. Bednorz, T. Williams, and A. Reller, Z. Phys. B. **82**, 211, (1991).

[27] David Singh, private communication.

[28] J. Hubbard, Proc. Roy. Soc. **A276**, 238 (1964).

[29] J. Zaanen, G. A. Sawatsky, and J. W. Allen, Phys. Rev. Lett. **55**, 418 (1985).

[30] J.B. Torrance, P. Lacorre, Chinnarong Asavaroengchai, R.M. Metzger, J. Sol. St. Chem. **90**, 168 (1991).

[31] J. Zaanen and G.A. Sawatsky, Canad. J. Phys. **65**, 1262 (1987).

[32] A. S. Barker, jr., and J. P. Remeika, Phys. Rev. **B10**, 987 (1974).

[33] A. Rosencwaig, G.K. Wertheim, J. Electron. Spectrosc. **1** 493 (1973).

[34] S.Uchida, T.Ido, H.Takagi, T.Arima, Y.Tokura, S. Tajima, Phys. Rev. **B43**, 7942, (1991).

[35] S.L.Cooper, G.A. Thomas, J.Orenstein, D.H.Rapkine, A.J. Millis, S-W.Cheong, and A.S. Cooper, Phys. Rev. **B41**, 11605 (1990).

[36] M. Reedyk, T. Timusk, J.S. Xue, J.E. Greedan, Phys. Rev. **B45**, 7406, (1992).

[37] A. Fujimori, E. Takayama-Muromachi, Y. Uchida, and B. Okai, Phys. Rev. **B35**, 8814 (1987).

[38] A.S. Barker, jr. and J.P. Remeika, Sol. St. Comm. **8**, 1521 (1970).

[39] W.F. Brinkman and T. M. Rice, Phys. Rev. **B2**, 4302, 1970.

[40] Peter Fulde, *Electron Correlations in Molecules and Solids*, Berlin: Springer-Verlag, 1991.

[41] J. Spalek, J. Sol. St. Chem., **88**, 2, (1990).

[42] T. B. Reed and E. R. Pollard, J. Cryst. Growth, **2**, 243 (1968).

[43] D. A. Maclean, Ph. D. thesis, McMaster University, 1980.

[44] D. A. Maclean, H. N. Ng, J. Sol. St. Chem, **30**, 35, (1979).

[45] M.A. Cardona, Phys. Rev **140**, A651, (1965).

[46] Y. Fujishima, Y. Tokura, T. Arima and S. Uchida, Physica C **185-189**, 1001 (1991).

[47] H. P. R. Frederikse and W. R. Hosler, Phys. Rev. **161**, 822 (1967).

[48] O. N. Tufte and P. W. Chapman, Phys. Rev. **155**, 796 (1967).

[49] A.S. Barker, jr., *Proceedings of the International Colloquium on the Optical Properties and Electronic Structure of Metals and Alloys, Paris, 1965*, North-Holland, Amsterdam, 1966.

[50] K. Uematsu, O. Sakurai, N. Mizutani and M. Kato, J. Mat. Sci. **19**, 3671 (1984).

[51] Wenhe Gong, H. Yun, Y. B. Ning, J. E. Greedan, W. R. Datars and C. V. Stager, J. Sol. St. Chem. **90**, 320 (1991).

[52] W. Harrison, *Electronic Structure and the Properties of Solids*, San Fransisco: W. H. Freeman and Company, 1980.

[53] M. Couzi, P. Vam Huong, J. Chim. Phys. **69**, 1339 (1972).

[54] S. Tajima, A. Masaki, S. Uchida, T. Matsuura, K. Fueki and S. Sugai, J. Phys. C. **20**, 3469 (1987).

[55] Y. Luspin, J. L. Servoin and F. Gervais, J. Phys. C. **13**, 3761 (1980).

[56] M. D. Fontana, G. Metrat, J. L. Servoin and F. Gervais, J. Phys. C. **16**, 483 (1984).

[57] J. L. Servoin, Y. Luspin and F. Gervais, Phys. Rev. **B22**, 5501 (1980).

[58] A. S. Barker, jr. Phys. Rev. **145**, 391 (1966).

[59] Ichiro Nakagawa, Atushi Tsuchida and Takehiko Shimanouchi, J. Chem. Phys. **47**, 982 (1967).

[60] E. J. Huibregtse, D. B. Barker and G. C. Danielson, Phys. Rev. **82**, 770 (1951).

[61] M. Abe and K. Uchino, Mat. Res. Bull. **9**, 147 (1974).

[62] J. P. Goral and J. E. Greedan, J. Mag. Magn. Mat. **37**, 315 (1983).

[63] R. F. Milligan, T. F. Rosenbaum, R. N. Bhatt and G. A. Thomas, "A Review of the Metal-Insulator Transition in Doped Semiconductors" in *Electron-Electron Interactions in Disordered Systems* edited by A.L. Efros and M. Pollack. Amsterdam: Elsevier, 1985.

[64] G. A. Thomas, M. Capizzi, F. DeRosa, R. N. Bhatt and T. M. Rice, Phys. Rev. **B23**, 5472 (1981).

[65] J. L. Pankove and P. Aigrain, Phys. Rev. **126**, 956 (1962).

[66] S. Narita and M. Kobayashi, Phil. Mag. **B42**, 895, 1980.

[67] G. A. Thomas, D. H. Rapkine, S. L. Cooper, S-W. Cheong, A. S. Cooper, L.F. Schneemeyer and J. V. Waszczak, Phys. Rev. **B 45**, 2474 (1992).

[68] E.K. Kudinov, D.N. Mirlin, and Yu. A. Firsov, Sov. Phys.Sol.St. **11**, 2257 (1970).

[69] V.N. Bogomolov, E.K. Kudinov, D.N. Mirlin and Yu. A. Firsov, Sov. Phys. Sol. St. **9**, 1630 (1968).

[70] Y. Y. Suzuki, P. Pincus, and A. J. Heeger, Phys. Rev. **B44**, 7127 (1991).

[71] H.G. Reik and D. Heese, J. Phys. Chem. Solids **28**, 581 (1967).

[72] M. Reedyk, private communication.

[73] J.S. Xue, Ph. D. Thesis, McMaster University, 1992.

[74] Y. Watanabe, D. C. Tsui, J. T. Birmingham, N. P. Ong, J. M. Tarascon, Phys. Rev. **43**, 3026 (1991).

[75] H. Eskes, M. B. J. Meinders, G. A. Sawatzky, Phys. Rev. Lett., **67**, 1035 (1991).

[76] T. Ido, K. Magoshi, H. Eisaki, S. Uchida, Phys. Rev. **B44**, 12094 (1991).

[77] Y. Maeno, S. Awaji, H. Matusumoto, T. Fujita, Physica B, **165-166** 1185 (1990).

[78] M. Higuchi, K.Aizawa, K.Yamaya, and K. Kodaira, J.Sol.St.Chem. **92**, 573, (1991).

[79] Joseph E. Sunstrom IV, Susan M. Kauzlarich and Peter Klavins, Chem. Mater. **4**, 346 (1992).

[80] Adriana Moreo and Elbio Dagotto, Phys. Rev. **B42**, 4786, 1990.

[81] B. C. Webb, A. J. Sievers and T. Mihalisin, Phys. Rev. Lett. **57**, 1951 (1986).

[82] D. A. Bonn, J. D. Garrett, and T. Timusk, Phys. Rev. Lett. **61**, 1305 (1988).

[83] J. W. Allen and J. C. Mikkelsen, Phys. Rev. **B15**, 2952 (1977).

[84] T. T. Palstra, A. A. Menovsky, and J. A. Mydosh, Phys. Rev. **B33**, 6527 (1986).

[85] T. Timusk, private communication.

[86] H. Ehrenreich, H. R. Phillip, and B. Segall, Phys. Rev. **132**, 1918 (1963).

[87] Charles Kittel, *Introduction to Solid State Physics*, New York: John Wiley and Sons, 1976 p. 162.

[88] R.A. Smith *Semiconductors* (Cambridge: Cambridge University Press, 1978) chapter 4,8.

[89] J. C. Slater, Phys. Rev. **82**, 538 (1951).

[90] M. Eitel, J. E. Greedan, J. Less Comm. Metals, **116**, 95 (1986).

[91] J. C. Slater and G. F. Koster, Phys. Rev. **94**, 1498 (1954).

[92] J. F. Schooley, W. R. Hosler and Marvin Cohen, Phys. Rev. Lett. **12**, 474 (1964).

[93] D.B.McWhan and T.M. Rice, Phys. Rev. Lett., **22**, 887 (1969).

[94] H. Takagi, T. Ido, S. Ishibashi, M. Uota, and S. Uchida, Phys. Rev. **B40**, 2254 (1989).